

May 2016

# Design, Implementation, and Evaluation of a Fluorescence Laminar Optical Tomography Scanner for Brain Imaging

Mahya Sheikhzadeh  
*University of Wisconsin-Milwaukee*

Follow this and additional works at: <https://dc.uwm.edu/etd>



Part of the [Biomedical Engineering and Bioengineering Commons](#), and the [Electrical and Electronics Commons](#)

---

## Recommended Citation

Sheikhzadeh, Mahya, "Design, Implementation, and Evaluation of a Fluorescence Laminar Optical Tomography Scanner for Brain Imaging" (2016). *Theses and Dissertations*. 1248.  
<https://dc.uwm.edu/etd/1248>

This Thesis is brought to you for free and open access by UWM Digital Commons. It has been accepted for inclusion in Theses and Dissertations by an authorized administrator of UWM Digital Commons. For more information, please contact [open-access@uwm.edu](mailto:open-access@uwm.edu).

DESIGN, IMPLEMENTATION, AND EVALUATION OF A  
FLUORESCENCE LAMINAR OPTICAL TOMOGRAPHY  
SCANNER FOR BRAIN IMAGING

by

Mahya Sheikhzadeh

A Thesis Submitted in  
Partial Fulfillment of the  
Requirements for the Degree of

MASTER OF SCIENCE  
IN ENGINEERING

at

The University of Wisconsin–Milwaukee

May 2016

## ABSTRACT

# DESIGN, IMPLEMENTATION, AND EVALUATION OF A FLUORESCENCE LAMINAR OPTICAL TOMOGRAPHY SCANNER FOR BRAIN IMAGING

by

Mahya Sheikhzadeh

The University of Wisconsin–Milwaukee, 2016  
Under the Supervision of Professor Ramin Pashaie

Implementation of new instrumentation and techniques for neuroscience research in recent years has opened new avenues in the study of the dynamics of large-scale neural networks such as the brain. In many of these techniques, including fluorescence recordings and optogenetic stimulation, a combination of photonics and molecular genetic methods are exploited to manipulate and monitor neural activities. Such techniques have been proven to be highly efficient in unraveling the mysteries of data processing in the micro circuits of the brain and as a result these techniques are widely used nowadays in most neuroscience labs.

In optogenetics, cell-types of interest are genetically modified by expressing light-sensitive proteins adapted from microbial opsin. Once these proteins are expressed, we are able to use light of appropriate wavelengths to manipulate, increase or suppress neural activity of specific neurons on command. With a high temporal resolution (in the order of milliseconds) and cell-type-specific precision, optogenetics is able to probe how the nervous system functions in real-time, even in freely-moving animals.

Currently, whenever genetic modifications are employed in the study of nervous systems, fluorescence proteins are also co-expressed in the same cells as biological markers to visualize the induced changes in the targeted cells. Despite its importance to trace the signal of such markers in-vivo, capabilities of the developed fluorescence tomography instrumentation are still limited and researchers mostly document the fluorescence distribution and expression of proteins of interest after euthanizing the animal and dissection of the tissue.

In this project, we present our effort in implementing a fluorescence laminar optical tomography (FLOT) system which is specifically designed for non-invasive three dimensional imaging of fluorescence proteins within the brain of rodents. The application of the developed technology is not limited to optogenetics, but it can be used as a powerful tool to help improving the precision and accuracy of neuroscience and optogenetic experiments.

In this design, a set of galvanometer mirrors are employed for realization of a fast and flexible scanner while a highly sensitive camera records the produced fluorescence signals. Fluorescence laminar optical tomography (FLOT) scanner has shown promising results in imaging superficial areas up to  $2mm$  deep from the surface, with the resolution of  $\sim 200\mu m$ . Details of the design of the hardware and reconstruction algorithms are discussed and samples of experimental results are presented.



© Copyright by Mahya Sheikhzadeh, 2016  
All Rights Reserved

# TABLE OF CONTENTS

<b>1</b>	<b>Introduction and Background</b>	<b>1</b>
1.1	Medical Imaging . . . . .	2
1.2	Light-Tissue Interactions . . . . .	5
1.2.1	Absorption . . . . .	7
1.2.2	Scattering . . . . .	8
1.2.3	Fluorescence . . . . .	9
1.3	Light Propagation Models in Turbid Media . . . . .	10
1.3.1	Radiative Transport Theory . . . . .	12
1.3.2	Diffusion Approximation . . . . .	13
1.3.3	Monte Carlo . . . . .	14
1.3.3.1	General Procedure in MC Modeling . . . . .	15
1.3.3.2	MC modeling of Fluorescence Propagation . . . . .	19
<b>2</b>	<b>Overview of Optical Imaging Approaches</b>	<b>21</b>
2.1	Confocal Microscopy . . . . .	22
2.2	Two-photon Microscopy . . . . .	23
2.3	Optical Coherence Tomography . . . . .	23
2.4	Diffuse Optical Tomography . . . . .	24
2.5	Fluorescence Imaging . . . . .	24
2.6	Laminar Optical Tomography . . . . .	28
2.7	Optogenetics . . . . .	30
<b>3</b>	<b>Instrumentation and detection principles</b>	<b>36</b>
3.1	Measurement Configurations . . . . .	36
3.2	Hardware Design . . . . .	38
3.3	Software Development . . . . .	44
3.4	Data Analysis . . . . .	45
3.5	Image Reconstruction . . . . .	48
3.6	Data Representation . . . . .	52
3.7	Summary . . . . .	54
<b>4</b>	<b>Experimental Results and Data Analysis</b>	<b>55</b>
4.1	Simulation Studies . . . . .	55
4.2	Phantom Studies . . . . .	58
4.2.1	Design and Fabrication method of tissue phantoms . . . . .	59
4.2.2	Measuring the Optical Properties of Phantoms . . . . .	63
4.2.3	Measuring the Phantom Thickness . . . . .	65
4.2.4	Phantom Experimental Results . . . . .	67
4.3	In-vivo Studies . . . . .	71
4.3.1	Animal Preparation . . . . .	73

4.3.2	In-vivo Experimental Results . . . . .	74
4.4	Summary . . . . .	79
<b>5</b>	<b>Conclusion and Future Directions</b>	<b>81</b>
	<b>Bibliography</b>	<b>83</b>

# LIST OF FIGURES

1.1	Light-tissue interactions. The chromophore is used to imply that a molecule absorbs light, while the fluorophore indicates that a molecule emits light. 1: Incident Light 2: Scattering 3: Reflectance 4: Diffuse Reflectance 5: Absorption 6: Fluorescence Emission [17]. . . . .	6
1.2	The optical properties of tissue and their inter-relationships; where $\theta$ is the deflection angle of scatter and $\Psi$ is the azimuthal angle of scatter [19]. . . .	6
1.3	Jablonski energy diagram. After an electron absorbs a high energy photon the system is excited electronically and vibrationally (from $S_0$ to $S_1$ ). The system relaxes vibrationally, and eventually fluoresces at a longer wavelength. The thicker lines represent electronic energy levels, while the thinner lines indicate various vibrational energy states [20]. . . . .	9
1.4	Stokes shift is the difference (in wavelength or frequency) between positions of the band maxima of the excitation and emission spectra in an electronic transition [26]. . . . .	10
1.5	An overview of different light propagation models in tissue, a comparison between their accuracy and mathematical simplicity [29]. . . . .	11
1.6	Terms included in the RTE. (a) Photons lost through the boundary (radiance). (b) Photons lost due to absorption and scattering off of the direction $s$ . (c) Photon gain by scattering in direction $s$ . (d) Photon gain through sources within the volume $dV$ [29]. . . . .	13
1.7	Flow chart for MC modeling of the propagation of a single photon packet. After initializing the photon packet and finding the first step size, the photon is moved. All the photon-tissue interactions (absorption, scattering, refraction, reflection, transmission) are recorded and the photon weight is adjusted until the photon exits the tissue or the weight is below some threshold. Then, the photon packet is terminated and a new photon packet is started [32] . . . . .	16
1.8	Flowchart for the fluorescence Monte Carlo modeling. $\lambda_{exc}$ : excitation wavelength and $\lambda_{emm}$ : emission wavelength. A photon packet at the excitation wavelength is launched. The fluorescence photon is generated upon the absorption of an excitation photon. Fluorescence light propagation with optical properties at the emission wavelength is simulated [33]. . . . .	20
2.1	A comparison between different imaging modalities in terms of spatial resolution and depth of penetration [34]. . . . .	22
2.2	Excitation and emission spectra of NADH (left) and FAD (right). NADH excitation maximum happens at 340nm and the emission maximum is at 460nm. FAD excitation maximum is at 448 nm and the emission maximum is at 520nm [27]. . . . .	25
2.3	Excitation and emission spectra of Green Fluorescence Protein (GFP) [47] .	26
2.4	A typical fluorescence imaging optical set up [20]. . . . .	27

2.5	(a) ChR2 (channelrhodopsin) allows positive sodium ( $Na^+$ ) and potassium ( $K^+$ ) ions to pass through the channel in response to blue light exposure. NpHR (halorhodopsin) regulates the flow of negative chloride ( $Cl^-$ ) ions in response to yellow light. (b) Action spectra for ChR2 and NpHR, separated by 100nm. (c) Spike trains of neurons; blue light flashes cause action potential in the neuron, while yellow light exposure inhibits the activity of the neurons [59]. . . . .	32
2.6	(a) Optical fiber implanted in the brain tissue through a cannula guide, to deliver light and stimulate the targeted brain region. (b) A rat receiving two implants in the motor cortex on both hemispheres [9]. . . . .	33
2.7	Diagrams comparing (a) electric neural stimulation and (b) optogenetic stimulation. In optogenetics, cell-type targeting of the neurons is possible. [59]. .	34
2.8	(a) Schematic of the tagged ChR2 with green fluorescence protein (GFP), (b) the confocal microscopy image of a rat brain's slice, which is labeled with GFP.	35
3.1	Banana patterns of light penetration in the medium in the reflection and transmission geometries. As a rough rule of thumb, the mean depth of light penetration in the reflection mode is $\rho/2$ [66]. . . . .	37
3.2	LOT measurement geometry and source-detector configurations. (a) Point illumination [25]. (b) Line illumination. . . . .	38
3.3	Block diagram of the FLOT system. Collimated laser light passes through a cylindrical lens for line illumination. Dichroic mirror separates the illumination from the imaging path. Blue light is focused on the sample using the scan lens and is scanned and de-scanned using a pair of galvanometers. Emitted light is reflected from dichroic beam splitter and passes through a narrow band filter then imaged on the CCD camera. . . . .	40
3.4	Schematic of the XT2 collimated emission-port adapter [67]. . . . .	40
3.5	FLOT system implementation. (1) Laser Diode Drivers (2) EMCCD Camera (3) Filter Wheel (4) XT2, Collimated Emission-port Adapter (5) Galvanometer Mirrors (6) Galvanometer Drivers (7) Scan Lens (8) DAQ, Data Acquisition Device (9) Lab Jack (10) Achromatic Lens (11) Dichroic Beam Splitter (12) Cylindrical Lens (13) Collimator (14) Pigtailed laser diode. . . . .	41
3.6	(a) EMCCD camera (no. 2 on Figure 3.5) [67], (b) galvanometer mirrors (no. 5 and 6 on Figure 3.5) [68], (c) data acquisition device (no. 8 on Figure 3.5) [69]. . . . .	42
3.7	(a) Cylindrical lens (no. 12 on figure 3.5) [68], (b) achromatic doublet (no. 10 on figure 3.5) [68], (c) scan lens (no. 7 on figure 3.5) [68], (d) XT2, collimated emission-port adapter (no. 4 on figure 3.5) [67]. . . . .	43
3.8	Raw data for 7 source-detector separations in FLOT measurements from a sample with an embedded rectangular channel, $150 \times 25$ microns in size, located at the depth of 1.19mm, and filled with $8\mu M$ FAD, after background correction (color bar shows the fluorescence intensity). . . . .	47
3.9	Monte Carlo simulation in a scattering medium for four different SD separations from 0 to 1.6 mm in logarithmic scale (color bar shows the fluorescence intensity). . . . .	49

3.10	2D and 3D reconstruction of a sample with a rectangular channel ( $150 \times 25$ microns) at the depth of 0.8 mm. (a) 2D ZX cross-section. (b) 3D volumetric reconstruction, XYZ view. (c) 3D volumetric reconstruction, YZ (side) view. (d) 3D volumetric reconstruction, XY (top) view. . . . .	53
4.1	Simulation of 3D reconstruction of a square object at the depth of 2 mm. (a) 3D volumetric image of the real object in XYZ view. (b) 3D volumetric image of the reconstructed object in XYZ view. . . . .	56
4.2	Simulation of 2D reconstruction of a square object at the depth of 2 mm. (a) 2D ZX cross-sections of the real object. (b) 2D ZX cross-sections of the reconstructed object. . . . .	57
4.3	Phantom fabrication process 1. (a) Plain mold, (b) weighting curing agent and $TiO_2$ , (c) weighting PDMS base and India ink, (d) pouring the mixture into the mold, (e) vacuum degassing, (f) oven baking. . . . .	61
4.4	Phantom fabrication process 2. (g) Demolding and cutting the phantom, (h) pinning the input/output holes, (i) oxygen plasma surface activation, (j) final phantom and its image under microscope, (k) thickness measurements, (l) FAD injection using syringe pump. . . . .	62
4.5	Double Integrating Sphere setup used to measure the diffuse reflected and transmitted light. (a) Schematic (taken and modified from [88]), (b) experimental setup. . . . .	63
4.6	Measuring the depth of a phantom with the channel size of $100 \times 50 \mu m$ . (a) and (b) Measuring the depth under the microscope, (c) and (d) measuring the depth using the OCT. . . . .	66
4.7	Optical setup for scanning phantoms. . . . .	67
4.8	A phantom with a rectangular channel ( $200 \times 25$ microns) embedded at the depth of 0.82mm. Images were reconstructed by SART algorithm after 1600 iterations, (a) raw data (color bar shows the fluorescence intensity), (b) 2D ZX cross-section of reconstructed channel (cross-section no. 30), (c) 3D volumetric of reconstructed channel, XYZ view. . . . .	68
4.9	A phantom with a rectangular channel ( $150 \times 25$ microns) embedded at the depth of 1.18mm. Images were reconstructed by SART algorithm after 4000 iterations, (a) raw data (color bar shows the fluorescence intensity), (b) 2D ZX cross-section of reconstructed channel (cross-section no. 30), (c) 3D volumetric of reconstructed channel, XYZ view. . . . .	69
4.10	A phantom with a rectangular channel ( $150 \times 25$ microns) embedded at the depth of 1.18mm. Images were reconstructed by SART algorithm after 2000 iterations, (a) raw data (color bar shows the fluorescence intensity), (b) 2D ZX cross-section of reconstructed channel (cross-section no. 30), (c) 3D volumetric of reconstructed channel, XYZ view. . . . .	70
4.11	A comparison between the results of the OCT and FLOT in finding the depth of channels. . . . .	71
4.12	Experimental setup in surgery room for in vivo scanning of rat brain. . . . .	72
4.13	Injection sites and rat's skull before the injection. . . . .	74

4.14	Single-fiber probe system [89]. A rat before and during the experiments with the probe system. . . . .	75
4.15	Experimental raw data of a rat brain which was injected with GFP in right hemisphere, at the depth of 0.8mm (color bar shows the fluorescence intensity).	76
4.16	Experimental data of an in-vivo scan of a rat brain with the injection depth of 0.8mm and injection volume of $0.2\mu l$ in the right hemisphere, (a) a confocal microscopy image of a slice close to the site of experiment, (b) FLOT reconstruction result, (c) probe system's curve showing the fluorescence intensity as a function of the penetration depth, (d) superimposed image of the reconstruction result and the confocal microscopy image. . . . .	77
4.17	Experimental data of an in-vivo scan of a rat brain with the injection depth of 0.8mm and injection volume of $0.2\mu l$ in the left hemisphere, (a) a confocal microscopy image of a slice close to the site of experiment, (b) FLOT reconstruction result, (c) probe system's curve showing the fluorescence intensity as a function of the penetration depth, (d) superimposed image of the reconstruction result and the confocal microscopy image. . . . .	78
4.18	Experimental data of an in-vivo scan of a rat brain for which the gene expression was not successful, (a) the probe system signal, (b) confocal image of the corresponding brain slice. . . . .	79

## LIST OF TABLES

1.1	Comparison between some of the medical imaging modalities (adopted and modified from [16]). . . . .	5
-----	---	---



## LIST OF ABBREVIATIONS

<b>2D</b>	Two-dimensional
<b>3D</b>	Three-dimensional
<b>ART</b>	Algebraic Reconstruction Technique
<b>CCD</b>	Charge Coupled Device
<b>ChR2</b>	Channelrhodopsin-2
<b>CM</b>	Confocal Microscopy
<b>CT</b>	Computed Tomography
<b>DA</b>	Diffusion Approximation
<b>DAQ</b>	Data Acquisition
<b>DE</b>	Diffusion Equation
<b>DOT</b>	Diffuse Optical Tomography
<b>EMCCD</b>	Electron-multiplying Charge-coupled Device
<b>FAD</b>	Flavin Adenine Dinucleotide
<b>FCM</b>	Fluorescence Confocal Microscopy
<b>FCT</b>	Fluorescence Coherence Tomography
<b>FLOT</b>	Fluorescence Laminar Optical Tomography
<b>fMRI</b>	functional Magnetic Resonance Imaging
<b>FMT</b>	Fluorescence Molecular Tomography
<b>FOV</b>	Field of View
<b>FP</b>	Fluorescent Proteins
<b>GFP</b>	Green Fluorescent Protein
<b>IAD</b>	Inverse Adding Doubling
<b>LOT</b>	Laminar Optical Tomography
<b>MC</b>	Monte Carlo

<b>MPM</b>	Multi-photon Microscopy
<b>MRI</b>	Magnetic Resonance Imaging
<b>NADH</b>	Nicotinamide Adenine Dinucleotid
<b>NpHR</b>	Natronomonas Haraonis Halorhodopsin
<b>OCM</b>	Optical Coherence Microscopy
<b>OCT</b>	Optical Coherence Tomography
<b>PAM</b>	Photo-acoustic Microscopy
<b>PAT</b>	Photo-acoustic Tomography
<b>PDMS</b>	Polydimethylsiloxane
<b>PET</b>	Positron Emission Tomography
<b>RT</b>	Radiation (Radiative) Transport (Transfer)
<b>RTE</b>	Radiative Transfer Equation
<b>SART</b>	Simultaneous Algebraic Reconstruction Technique
<b>SD-OCT</b>	Spectral-Domain Optical Coherence Tomography
<b>SIRT</b>	Simultaneous Iterative Reconstruction Technique
<b>SNR</b>	Signal to Noise Ratio
<b>SPECT</b>	Single-Photon Emission Computerized Tomography
<b>TiO<sub>2</sub></b>	Titanium Dioxide
<b>TPM</b>	Two-photon Microscopy
<b>US</b>	Ultrasound
<b>YFP</b>	Yellow Fluorescent Protein

## ACKNOWLEDGEMENTS

The research included in this thesis could not have been performed if not for the assistance, patience, and support of many individuals. I would like to extend my gratitude first and foremost to my advisor Dr. Ramin Pashaie for the continuous support of my Masters study and research, for his motivation, enthusiasm, and immense knowledge. I was always amazed, by his patience and approach to the solutions of any problem. Apart from technical discussions, I had learned from him on how to develop scientific thinking, and more importantly, how to keep an open mind. I attribute the level of my Masters degree to his encouragement and effort, while allowing me the room to work in my own way.

I would also like to thank Dr. Chiu Tai Law, and Dr. Yongjin Sung for serving as my committee members and the assistance they provided at all levels of the research project. I owe my deepest gratitude to our collaborators, Dr. Woo Jin Chang, Wookkun Kwon, Department of Mechanical Engineering, Dr. Fred J. Helmstetter, and Dr. Patrick Cullen, Department of Neuroscience, at the University of Wisconsin-Milwaukee, for providing us with the help in making our phantoms and conducting the in-vivo experiments on rat brains. Without their collaborations and supports, this work could not reach to this level.

Thanks must go to my fellow lab mates in BIST lab, for the stimulating discussions, and for all the fun we have had in the last two years. My sincere thanks to Mehdi Azimpour, who worked on this project with me, for pointing me the direction and giving useful ideas and sharing his knowledge and experience. Farid Atry also deserves special thanks for many interesting discussions we had on the hardware of the system and reconstruction schemes.

Last but not the least, I would like to thank my family for the support they provided me through my entire life, and in particular, I must acknowledge my dear mother for her unconditioned love, my husband and best friend, Mehdi Gilaki, whom without his love, encouragement and support, I would not be where I am today.

---

# Chapter 1

## Introduction and Background

Brain imaging using X-ray Computed Tomography (X-ray CT) or Magnetic Resonance Imaging (MRI) are well accepted clinically these days. However, these methods are limited in spatial resolution (in the range of submillimeter) and temporal resolution (in the range of seconds). As a result, there are many unanswered questions on the normal brain functions, due to its complexity, that makes it difficult to study in details with high resolution and less scanning time, without damaging its functionality.

Optical brain imaging, as a fast and non-invasive method, allows the living brain to be closely observed, and many functional interactions and changes, such as hemoglobin oxygenation, membrane potential and metabolic processes, to be investigated in details over different durations. One of the most significant benefits of optical imaging is that it provides sensitivity to functional changes, either via intrinsic or extrinsic contrast changes in absorption, fluorescence, or scattering parameters of the tissue under test [1][2].

In spite of the the advantages of in-vivo optical imaging, there are also many challenges. One significant challenge is the multiple light scattering of photons which distorts the waves propagating through the tissue, causing the loss of directionality. This can effect the performance of optical imaging, especially in terms of the penetration depth and achievable imaging resolution [3][4]. While there have been efforts to mitigate the effect of light scattering, by using techniques such as confocal and two-photon microscopy [5][6], that work by rejecting the scattered light, there also have been interesting studies in which they not only overcome the effect of light scattering but also make use of the multiple scattering in an effective way [4].

Laminar Optical Tomography (LOT) [7] was developed to address this need as an optical

imaging modality that provides non-contact imaging of superficial tissue, offering better resolution than Diffuse Optical Tomography (100-200 micron), and deeper penetration depth compared to Laser Scanning Microscopy ( $> 2mm$ ). The fact that LOT takes advantage of absorption, scattering and fluorescence contrast, over a large field of view and high acquisition speeds, makes it suitable for imaging of superficial tissue such as retina, skin, endothelial tissues and cortical regions of the brain [8].

The aim of this project is to improve the quality and functionality of the latest LOT design, focusing on fluorescence imaging for optogenetic applications. Optogenetics is a recently developed neuromodulation technique, which allows the activity of neurons to be modulated by light, with high spatial and temporal resolution. For this purpose, the targeted cells are genetically modified to produce light-sensitive proteins [9]. Fluorescent markers are a common choice for serving as biomarkers in optogenetics. Introducing these proteins into targeted cells or the brains of live animals provides a systematic mechanism to track light sensitization of neurons. This project strives to introduce and test a technique for the brain imaging to extract the location and depth information of the fluorescent distribution following the gene delivery.

This chapter starts with a brief introduction to medical imaging modalities and the physics of the light tissue interaction. Then, different models for light propagation in tissue, relevant to this project, are summarized.

## 1.1 Medical Imaging

Medical imaging refers to several different technologies and modalities that aim to image a specific physiological activities (functional imaging) or anatomical structure (structural imaging). These technologies provides different information based on their applications on different parts of the body and can be used to study or treat diseases, injuries, screen drugs and effectiveness of medical treatments. In general, imaging techniques include the fields of

radiology, nuclear medicine and optical imaging.

**Radiological methods** render the anatomical and physiological details of the human body with a very high spatial and temporal resolution [10]. This discipline includes methods such as Ultrasound (US), X-ray, Computed Tomography (CT) and Magnetic Resonance Imaging (MRI).

Ultrasound is a noninvasive and effective medical procedure that uses high frequency sound waves to create images of internal organs. It's an extremely fast technique, which is capable of real-time imaging with relatively high spatial resolution and involves no ionizing radiation [11]. Ultrasound uses a device known as a transducer to send high-frequency sound waves into the body. Sound waves emitted by the transducer reflect back from internal structures and are transmitted back to the ultrasound machine to produce images of the area of interest. Ultrasound technology can also produce audible sounds of blood flow using Doppler effect, to be used for other applications such as the detection of compromised blood flow in veins and arteries. However the weakness of this technique is the poor soft-tissue contrast, that causes certain organs not to be easily imaged.

X-ray technology is the oldest and most frequently used form of medical imaging. It uses ionizing radiation to produce images of the patient's internal structure by sending X-ray beams through the body, and detecting the transmitted beams on the opposite side [12][13]. Contrast in the images between different tissue samples arises from differential attenuation of X-rays beam in the body, which depends on the density of the organs [11]. X-rays are especially useful in showing detailed images of skeletal structure. They are more limited when it comes to injuries or abnormalities in soft tissues such as tendons and ligaments.

CT combines multiple X-ray projections taken from different angles to produce detailed cross-sectional images (slices) of soft tissues, organs, bones, blood vessels and the brain. The major disadvantage of both X-ray and CT is the use of ionizing radiation, which is harmful for the body and as a result, there is a limit on the total radiation dose per year to which a patient can be exposed [11].

MRI is a noninvasive, high resolution technology that uses a magnetic field and radio waves to create detailed images of internal organs and other tissues. MRI is very effective in diagnosing a number of conditions as it has the ability to show the difference between the normal and diseased soft tissues of the body. It is also capable of creating images of biological functions such as cardiac function. However, the deficiency of this technique is that it's expensive, lengthy and more susceptible to patient's motion.

In **Nuclear imaging techniques**, such as Positron Emission Tomography (PET) and Single-Photon Emission Computerized Tomography (SPECT), the organ function and structure of the human body is being investigated as opposed to traditional anatomical imaging such as CT or MRI. It involves the application of radioactive substances, introduced into the body in very small amounts, to locate a disease within the body and deliver treatment directly to targeted anatomical sites. Nuclear medicine images can be superimposed with CT or MRI to produce detailed, computerized pictures of areas inside the body. This is known as image fusion or co-registration and can lead to more precise information and accurate diagnoses [14].

**Optical imaging** uses light and properties of photons to obtain detailed images of organs, tissues or even smaller structures like cells or molecules. Unlike most other medical imaging techniques, optical imaging is non-invasive as it uses non-ionizing radiation to excite electrons without harming the tissue. As a result, it is much safer for patients and significantly faster so that it can be used for lengthy and repeated procedures to monitor both static characteristics and dynamic events in the tissue or organ in real time [15].

Table 1.1 gives a quick comparison between some of the medical imaging techniques discussed in this section.

**Table 1.1:** Comparison between some of the medical imaging modalities (adopted and modified from [16]).

Imaging Technique	Portion of EM Radiation	Spatial Resolution	Depth	Temporal Resolution
Magnetic resonance imaging (MRI)	radiowaves	25 – 100 $\mu m$	no limit	minutes to hours
Computed tomography (CT)	X-rays	50 – 200 $\mu m$	no limit	minutes
Ultrasound	high-freq sound	50 – 500 $\mu m$	mm to cm	seconds to minutes
Positron emission tomography (PET)	high-energy $\gamma$ rays	1-2 mm	no limit	10 sec to minutes
Single photon emission computed tomography (SPECT)	lower-energy $\gamma$ rays	1-2 mm	no limit	minutes
Optical fluorescence imaging	visible light or NIR	2-3 mm	< 1cm	seconds to minutes

Imaging Technique	Ability of human imaging	Advantages	Disadvantages	Cost
Magnetic resonance imaging (MRI)	yes	high spatial res., morphological & func. imaging	low sensitivity, long scan and post processing time, mass probe	\$\$\$\$
Computed tomography (CT)	yes	bone, tumor & anatomy imaging	limited soft tissue res., radiation	\$\$
Ultrasound	yes	real-time, low cost	limited spatial res.	\$\$
Positron emission tomography (PET)	yes	high sensitivity, isotopes can substitute naturally occurring atoms, quantitative translational research	PET cyclotron or generator needed, relatively low spatial res., radiation to subject	\$\$\$\$
Single photon emission computed tomography (SPECT)	yes	can image multiple probes, adapted to clinical imaging	relatively low spatial res. because of sensitivity, collimation, radiation	\$\$\$
Optical fluorescence imaging	yes but limited	high sensitivity, detects fluorochrome in live and dead cells	low spatial resolution, surface-weighted	\$-\$\$

## 1.2 Light-Tissue Interactions

Optical properties of a tissue can be characterized by studying the interaction of light with a medium. It can also help us to extract important information about the structure and dynamics of the materials. When light (laser beams) transport within scattering tissues such as skin, breast, brain and vessels, different scenarios might happen. This includes absorption, scattering, luminescence (fluorescence and phosphorescence), reflection from boundaries and transmission through boundaries. These interactions are shown in Figure 1.1.



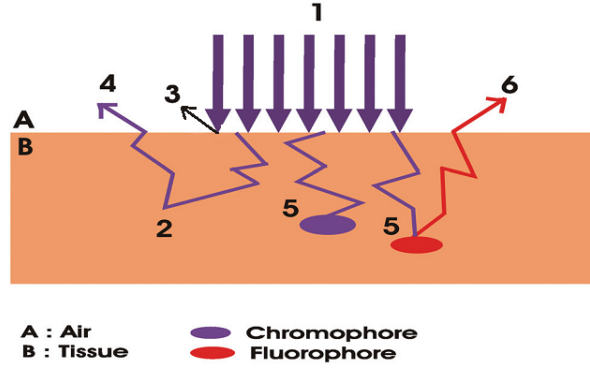


**Figure 1.1:** Light-tissue interactions. The chromophore is used to imply that a molecule absorbs light, while the fluorophore indicates that a molecule emits light. 1: Incident Light 2: Scattering 3: Reflectance 4: Diffuse Reflectance 5: Absorption 6: Fluorescence Emission [17].

Multiple scattering and absorption are the cause of laser beam broadening and decaying, whereas bulk scattering is the main reason for beam dispersion in the backward direction. As a result, light propagation within a tissue depends on the absorption and scattering properties of its components. The size, shape, concentrations and refractive index of the tissue's particles as well as the polarization states of the incident light, all have major impacts on the propagation of light in tissue [18].

Determining the optical properties of a tissue (absorption, scattering, anisotropy, reduced scattering, refractive index) is the first step toward properly designing a device. Figure 1.2 shows the optical properties of tissue and their inter-relationships [19]. These properties can be measured through a combination of experiments and optical theory, which will be covered in more details in chapter 4.

Absorption	$\mu_a$	$[\text{cm}^{-1}]$
Scattering	$\mu_s$	$[\text{cm}^{-1}]$
Scattering function	$p(\theta, \psi)$	$[\text{sr}^{-1}]$
Anisotropy	$g = \langle \cos \theta \rangle$	$[-]$
Real refractive index	$n'$	$[-]$
Reduced scattering	$\mu_s' = \mu_s(1-g)$	$[\text{cm}^{-1}]$

**Figure 1.2:** The optical properties of tissue and their inter-relationships; where  $\theta$  is the deflection angle of scatter and  $\Psi$  is the azimuthal angle of scatter [19].

### 1.2.1 Absorption

Absorption of light is the way in which the energy of a photon is taken up, typically by transferring to the atoms and molecules of the matter, when light wave is propagating through a medium. The overall effect of absorption is a reduction in the transmitted light intensity which is often called attenuation [20].

The absorption coefficient  $\mu_a[cm^{-1}]$ , is a parameter that gives the probability for a photon to be absorbed per unit path length. The reciprocal of absorption coefficient ( $1/\mu_a$ ) is called the mean absorption length [21]. It determines how far into a material, light with a particular wavelength, can penetrate before it is absorbed [22]. A large absorption coefficient means that the beam is quickly attenuated as it passes through the medium while a small absorption coefficient means that the medium is relatively transparent to the beam [20][23]. The absorption coefficient depends on the material and also on the wavelength of light which is being absorbed. This may be related to other properties of the object through the Beer-Lambert law:

$$I(L) = I_0 e^{-\mu_a \cdot L}, \quad (1.1)$$

where  $I(L)$  is the intensity of light after passing through the sample,  $I_0$  is the initial light intensity before passing through the sample,  $L$  is the path length and  $\mu_a$  is the absorption coefficient of the medium.

Chromophores are the structures of the tissue that absorb photons. They have different absorption wavelengths [24]. According to Beers law, the absorption coefficient of a tissue can be determined using the chromophore extinction coefficient ( $\varepsilon_i$ ), chromophore concentrations ( $c_i$ ), and the wavelength of light ( $\lambda$ ) [25]:

$$\mu_a(\lambda) = \sum_i \varepsilon_i(\lambda) c_i. \quad (1.2)$$

As mentioned before, absorption is one of the sources of optical imaging contrast. Many

substances in the body such as oxy-hemoglobin ( $HbO_2$ ) and deoxy-hemoglobin (HbR) in the blood or melanin in the skin are highly absorbing. Therefore, absorption forms a basis for many imaging techniques.

### 1.2.2 Scattering

In a scattering event, photons change the direction of propagation. This effect makes the light broadening and decaying and therefore limits the depth of penetration and introduces uncertainty in the path that light travels. The amount of scattering is inversely proportional to the wavelength of the light [24].

The scattering coefficient  $\mu_s[cm^{-1}]$ , gives the probability for a photon to be scattered in a matter per unit path length. The reciprocal of scattering coefficient ( $1/\mu_s$ ) is referred to as the scattering mean free path [21], which is the step-size that photons can travel in tissue before the scattering happens. Scattering coefficient can be expressed using Beer's law:

$$T(L) = e^{-\mu_s \cdot L}, \quad (1.3)$$

where  $T(L)$  is the ballistic transmittance,  $L$  is the path length and  $\mu_s$  is the scattering coefficient of the medium.

Usually in biological tissues, each photon undergoes several scattering events. In this case, the reduced scattering coefficient  $\mu'_s[cm^{-1}]$  can be defined along with the anisotropy of the scatterer ( $g$ ), the average cosine of the scattering angle, to describe this multiple scattering process:

$$g = \langle \cos\theta \rangle, \quad (1.4)$$

$$\mu'_s = \mu_s(1 - g), \quad (1.5)$$

where  $\theta$  is the deflection angle of scattering. Depending on the value of  $\theta$ ,  $g$  can get values between 0 (for completely isotropic scattering,  $\theta = 90^\circ$ ) to 1 (for heavy forward scattering,

$\theta = 0^\circ$ ). For photon scattering in biological tissues,  $g$  is typically between  $0.8 - 1$ . Similar to the absorption, scattering is another source of optical contrast in tissue.

### 1.2.3 Fluorescence

Another fundamental mechanism of interaction between light and tissue is fluorescence, which occurs upon the absorption of a photon energy by a fluorophore molecule at excitation wavelength, followed by the emission of a secondary photon (fluorescence) at a longer wavelength. Fluorescence is the result of a three-stage process: excitation of a molecule by an incoming photon, vibrational relaxation of excited state electrons to the lowest energy level, emission of a longer wavelength photon and return of the molecule to the ground state [26]. These three events are classically presented by the Jablonski energy diagram in Figure 1.3 [20].

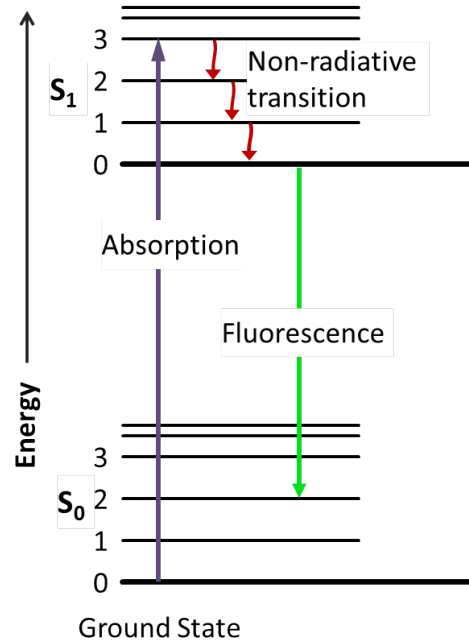


**Figure 1.3:** Jablonski energy diagram. After an electron absorbs a high energy photon the system is excited electronically and vibrationally (from  $S_0$  to  $S_1$ ). The system relaxes vibrationally, and eventually fluoresces at a longer wavelength. The thicker lines represent electronic energy levels, while the thinner lines indicate various vibrational energy states [20].

In most cases, the emitted light has a longer wavelength (lower energy) than the absorbed radiation. This phenomenon is known as the Stokes shift (named after Irish physicist George G. Stokes) and is measured as the difference between the maximum wavelengths or frequencies in the excitation and emission spectra. The size of the Stokes shift (Figure 1.4) can range from just a few nanometers to over several hundred nanometers, depending on the molecular structure [26]. Fluorescence process can provide valuable information about the optical imaging contrast.

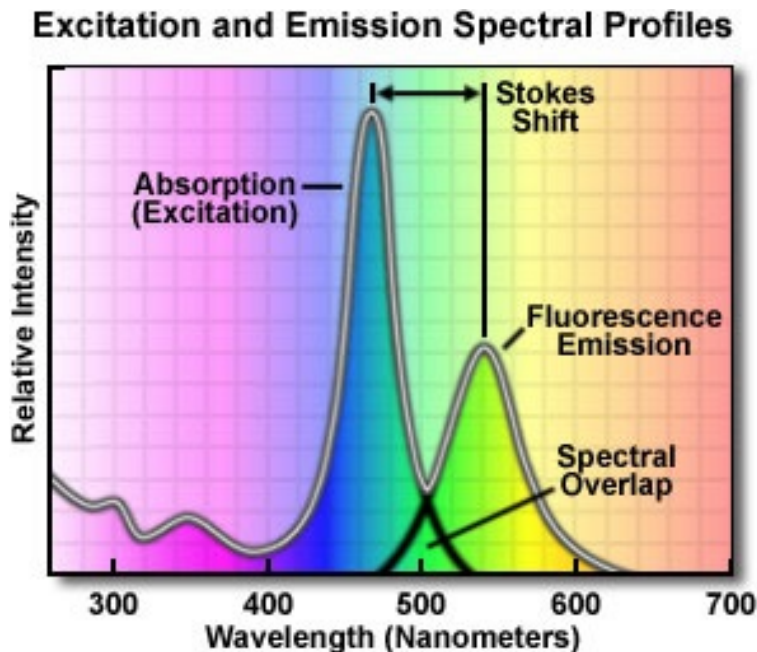


**Figure 1.4:** Stokes shift is the difference (in wavelength or frequency) between positions of the band maxima of the excitation and emission spectra in an electronic transition [26].

### 1.3 Light Propagation Models in Turbid Media

The development of a reliable optical instrument requires precise understanding of the light propagation in biological tissue. Therefore, modeling and simulation of photon propagation in different structures is an important step toward any optical device's design.

In one aspect, light propagation in tissue can be classified in two categories: particle models and wave models. First category describes light propagation in terms of photon

transport and includes methods such as radiation transport (RT) theory, diffusion theory and Monte Carlo (MC). Second category uses wave propagation theory such as Maxwell equations. For all these methods, we need to have a prior knowledge of the optical properties of tissue. Figure 1.5 shows an overview of these approaches and gives a comparison between them in terms of accuracy and mathematical simplicity.

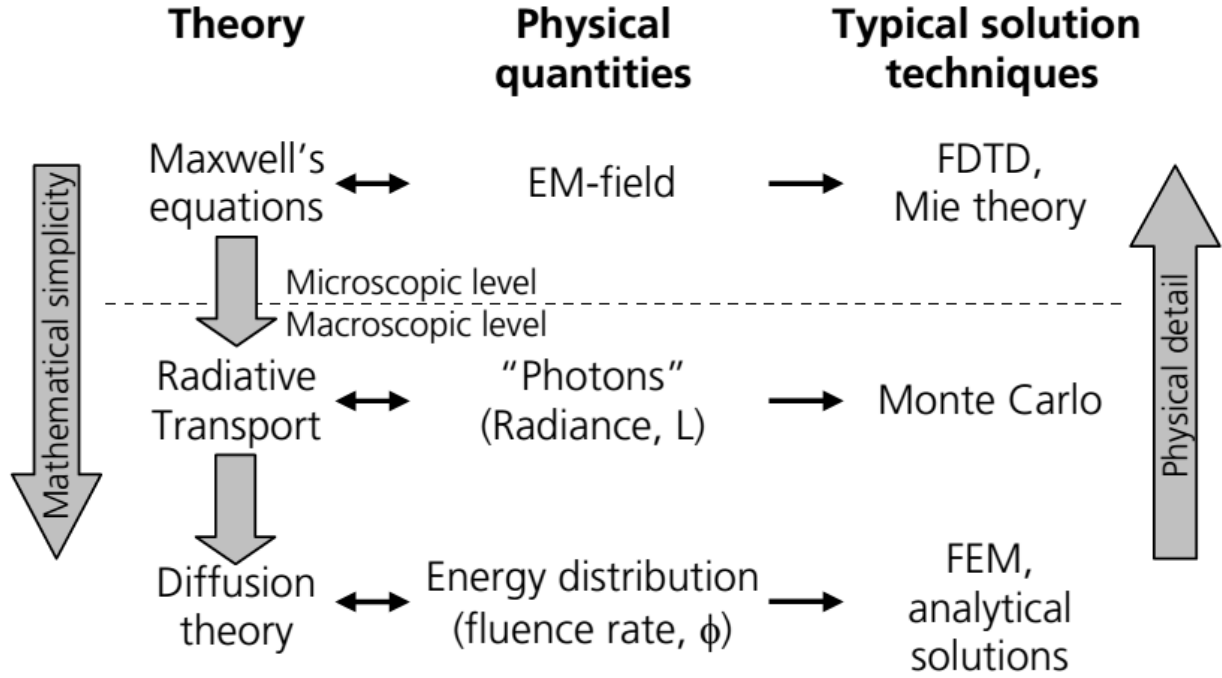


**Figure 1.5:** An overview of different light propagation models in tissue, a comparison between their accuracy and mathematical simplicity [29].

In this work, we only consider particle models of transport theory, which describes energy transport through a medium containing randomly distributed absorbing and scattering particles. Describing light propagation in terms of photon transport allows to use a number of mathematical simplifications to model complex mediums such as tissue, in compare with the mathematically and analytically complex theory of Maxwell [28].

Photon transport in biological tissue can be equivalently modeled either analytically by the radiative transfer equation (RTE) or numerically with Monte Carlo (MC) simulations. RTE is difficult to solve and some approximations need to be taken into account. It is often simplified by a diffusion approximation (DA). Overall, solutions to the diffusion equation

for photon transport are more computationally efficient, but less accurate than Monte Carlo simulations [21]. In this section, we mainly focus on Monte Carlo method, which best suited for our application.

### 1.3.1 Radiative Transport Theory

Photons transport through turbid media can be expressed by the Radiative Transfer Equation (RTE). RTE is derived by considering light to be a number of independently moving particles (photons), and expressing the energy balance of incoming, outgoing, absorbed and emitted photons of a small area element in the medium. Here, only the intensity of the light is considered and interference effects (loss or gain in photon energy due to the interaction) are not included in the model.

One approach to defining the RTE is based on a continuity equation for the photon density per solid angle,  $N(r, s, t)$  [ $1/m^3 sr$ ]. It describes the number of photons at the position  $r$  and time  $t$  with velocity  $v$  in the direction  $s$ . Then, the radiance  $L(r, s, t)$  [ $W/m^2 sr$ ] can be defined as the propagation of photon power per unit area and solid angle [29]:

$$L(r, s, t) = N(r, s, t) \frac{hv}{\lambda} . c, \quad (1.6)$$

where  $h$  is Plank's constant and  $c$  is the speed of light in the medium. The RTE (also called Boltzmann equation) can then be expressed in terms of the radiance  $L$  [21]:

$$\frac{\partial L(r, s, t)}{c \partial t} = -s \cdot \nabla L(r, s, t) - (\mu_a + \mu_s) L(r, s, t) + \mu_s \int_{4\pi} L(r, s', t) P(s' \cdot s) d\Omega' + S(r, s, t). \quad (1.7)$$

Terms on the right hand side in the RTE can be interpreted as: flow through the boundaries, absorption and scattering off the direction of  $s$ , scattering into the direction of  $s$  and sources  $S(r, s, t)$  [ $W/m^3 sr$ ] located within the volume element, respectively [29]. Figure 1.6 shows a small volume  $v$  with photons traveling in the direction  $s$ :

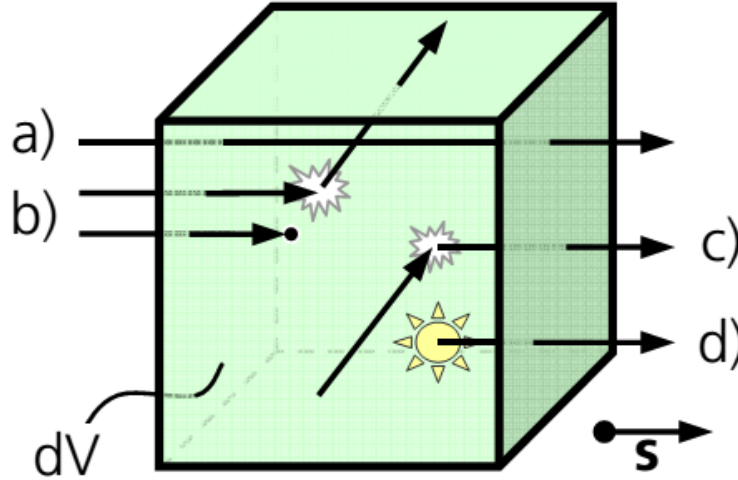


**Figure 1.6:** Terms included in the RTE. (a) Photons lost through the boundary (radiance). (b) Photons lost due to absorption and scattering off of the direction  $\mathbf{s}$ . (c) Photon gain by scattering in direction  $\mathbf{s}$ . (d) Photon gain through sources within the volume  $dV$  [29].

As mentioned before, RTE equation is difficult to solve numerically and exact solutions to it only exist for relatively simple problems. The fact that biological tissue scatters light strongly in the forward direction also makes the situation worse. Therefore, RTE is simplified using few approximations.

### 1.3.2 Diffusion Approximation

A formal method to solve RTE is to find the solution to its homogeneous part and expand the general solution in terms of the homogeneous solution obtained. In this regard, a simple approach would be to expand the radiance using appropriate function series. A well-known method is diffusion approximation (DA), which expresses the radiance  $L$  in equation 1.7 in terms of the fluence rate. The time-dependent diffusion equation (DE) is often written as [21]:

$$\frac{\partial \Phi(r, t)}{c \partial t} = -\mu_a \Phi(r, t) + D \nabla^2 \Phi(r, t) + S_0(r, t), \quad (1.8)$$



where  $S_0(r, t)$  is source term,  $\Phi(r, t)$  [ $W/m^2$ ] is the fluence rate and indicates net radiant energy or energy flow per unit area at position  $r$  at a given time  $t$ , and  $D$  is diffusion coefficient:

$$\Phi(r, t) = \int \int L(r, t) d\Omega, \quad (1.9)$$

$$D = \frac{1}{3(\mu_a + \mu_s(1 - g))}. \quad (1.10)$$

The diffusion approximation is only applicable when light propagates diffusely i.e. almost isotropically where  $(1 - g)\mu_s \gg \mu_a$ . This implies that the DE is not valid close to the light source as the condition for having an almost isotropic source is for the light to efficiently travel at least for a distance of  $1/\mu'_s$ .

However, as we will cover later in more details, for our application (i.e. FLOT), the diffusion approximation cannot be employed since none of these conditions are applicable to FLOT and light cannot be assumed to be diffuse. Here an alternative approach is using Monte Carlo Simulation.

### 1.3.3 Monte Carlo

Monte Carlo (MC) simulation provides a flexible yet rigorous approach for modeling the light propagation in tissues with small dimensions, where the diffusion approximation is not valid anymore. The required parameters for a MC simulation are the absorption coefficient, scattering coefficient and the scattering phase function.

Supposing the random walk of photons, MC offers a stochastic model, which uses probability distributions that describe the step-size of photon movement between sites of photon-tissue interaction and the angles of deflection in a photon's trajectory. During the random walk, depending on the optical properties of the medium, photon can get absorbed and lose energy, scattered into different direction, refracted or reflected. MC works by tracking all of

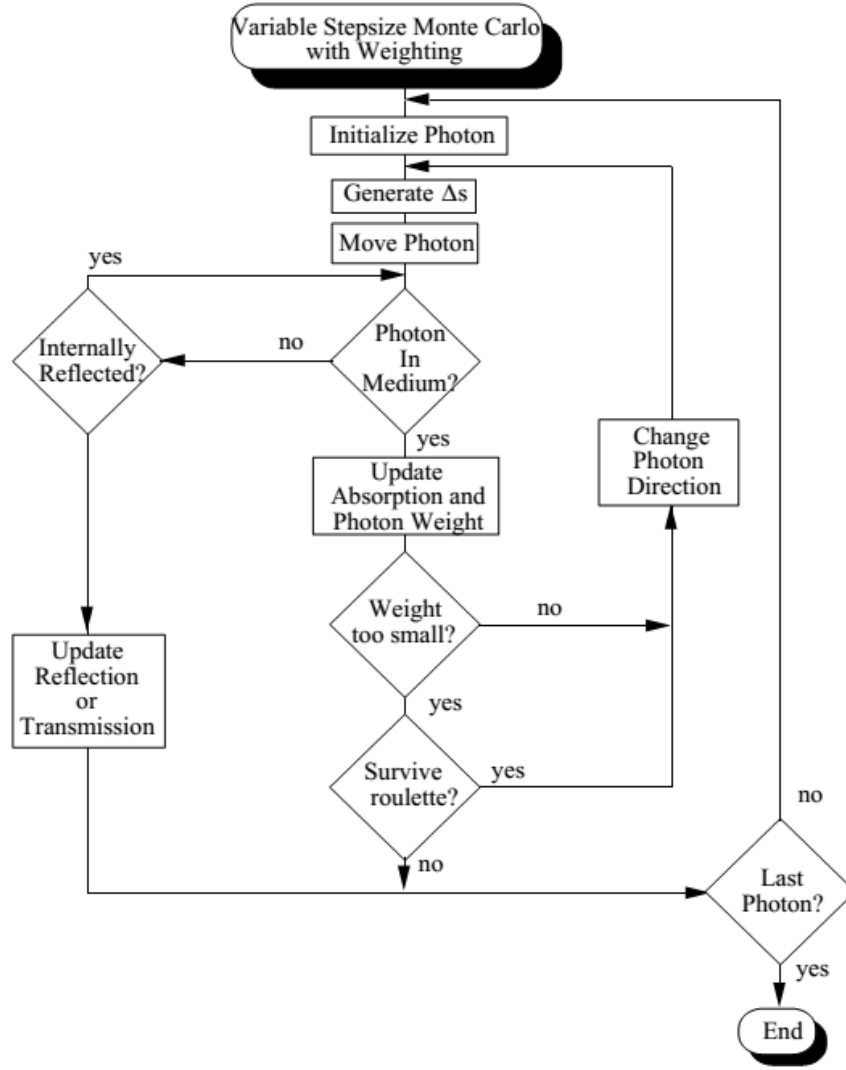
these light-tissue interactions and recording photons histories as they are scattered, absorbed or reflected. After propagating many photons, the net distribution of all the photon paths yields an accurate approximation to reality [20][30][31].

Figure 1.7 shows the flow chart of a general procedure of MC modeling. It starts with launching a photon packet with an initial assigned weight. Once launched, the photon is moved a distance  $\Delta s$ , step-size, which will be sampled randomly based on the optical properties of the tissue. As the photon propagates in the tissue it may be scattered, absorbed, internally reflected, or transmitted out of the tissue. At the end of each step, the photon packets weight is updated. If the photon escapes from the tissue, the reflection or transmission of the photon is recorded. If the photon is absorbed, the position of the absorption is recorded. Meanwhile, the new step-size and scattering angle for the next step is sampled randomly based on their respective probability distributions. The photon packet repeatedly moves in the tissue model step-by-step until it either escapes from tissue or is completely absorbed. Then, another photon packet is launched and this process is repeated until the desired number of photons are propagated. The process continues until the recorded reflection, transmission, and absorption profiles approach some accurate approximation close to the real values [32][33].

### 1.3.3.1 General Procedure in MC Modeling

**Photon Initialization [32]:** N number of photons are launched, each with a photon weight initially set to 1, which is computationally efficient. Starting coordinates for each photon is identical and a photon initial direction is chosen via convolution with the beam shape.

**Propagation distance [32]:** Choosing an efficient step-size,  $\Delta s$ , is quite important. A very small step might cause rare photon-tissue interactions while a very large one gives us a wrong estimation of the real photon movements. In general, step-size must be small relative to the average mean free path of a photon in tissue. The mean free pathlength is the reciprocal of the total attenuation coefficient:



**Figure 1.7:** Flow chart for MC modeling of the propagation of a single photon packet. After initializing the photon packet and finding the first step size, the photon is moved. All the photon-tissue interactions (absorption, scattering, refraction, reflection, transmission) are recorded and the photon weight is adjusted until the photon exits the tissue or the weight is below some threshold. Then, the photon packet is terminated and a new photon packet is started [32]

$$\Delta s \ll \frac{1}{\mu_t} = \frac{1}{\mu_a + \mu_s}. \quad (1.11)$$

**Coordinates update [32]:** For tracking photons movement we need the three spatial coordinates of the position and three directional angles of the movement. First one is defined with three Cartesian coordinates (x,y,z) and the second one with three direction cosines

$(\mu_x, \mu_y, \mu_z)$ . Then, the new coordinates  $(x', y', z')$  are given by:

$$\begin{aligned}x' &= x + \mu_x, \\y' &= y + \mu_y, \\z' &= z + \mu_z.\end{aligned}\tag{1.12}$$

**Internal reflection [32]:** The probability that a photon is internally reflected is determined by the Fresnel reflection coefficient  $R(\theta_i)$ :

$$R(\theta_i) = \frac{1}{2} \left[ \frac{\sin^2(\theta_i - \theta_t)}{\tan^2(\theta_i + \theta_t)} + \frac{\tan^2(\theta_i - \theta_t)}{\sin^2(\theta_i + \theta_t)} \right],\tag{1.13}$$

where  $\theta_i$  is the angle of incident on the boundary and  $\theta_t$  is the angle of transmission which can be found using Snell's law:

$$\theta_i = \cos^{-1} \mu_z,\tag{1.14}$$

$$n_i \sin \theta_i = n_t \sin \theta_t.\tag{1.15}$$

A random number  $(\xi)$ , uniformly distributed between 0 and 1, is used to determine if the photon is reflected or transmitted. If  $(\xi) < R(\theta_i)$  then the photon is internally reflected; otherwise, the photon exits the tissue and the event is recorded either as backscattered or transmitted light (depending on the position of the photon.) If the photon is recognized as reflected, then the coordinates and directions of the photon is updated accordingly.

**Photon absorption [32]:** After each propagation step, a fraction of the photon packet is absorbed and the remainder is scattered. The fraction of the packet that is absorbed is:

$$\frac{\mu_a}{\mu_a + \mu_s} = 1 - \frac{\mu_s}{\mu_a + \mu_s} = 1 - a,\tag{1.16}$$

where  $a$  is the single particle albedo. Therefore, the new photon weight ( $w'$ ) is given by  $w' = aw$ , which represents the fraction of the packet that is scattered.

**Photon termination [32]:** A minimum value for the weight of a photon packet is defined. A technique named roulette is used to terminate a photon when its weight is below minimum value. The roulette gives a photon a weight of  $w$ , one chance in  $m$ , of surviving with the weight  $mw$ . Otherwise,  $w$  will be set to zero and the photon is terminated.

$$w = \begin{cases} mw & \text{if } \xi \leq (\frac{1}{m}) \\ 0 & \text{elsewhere} \end{cases} \quad (1.17)$$

**Photon scattering [32]:** A normalized phase function describes the probability density function (PDF) for the azimuthal and longitudinal angles of a photon when it is scattered at angle  $(\theta, \phi)$ . If the phase function has no azimuthal dependence, then the azimuthal angle  $\phi$  is uniformly distributed between  $[0, 2\pi]$ , and may be generated by multiplying a pseudo-random number  $\xi \in [0, 1]$  by  $2\pi$  (i.e.  $\phi = 2\pi\xi$ ). The PDF for the scattered cosine of the deflection angle ( $\cos\theta$ ) in tissue is characterized by the Henyey-Greenstein phase function:

$$\cos\theta = \frac{1}{2g} \{1 + g^2 - [\frac{1 - g^2}{1 - g + 2g\xi}]^2\}, \quad (1.18)$$

where

$$\begin{cases} g \sim -1 & \text{reflective} \\ g \sim 0 & \text{isotropic} \\ g \sim 1 & \text{forward} \end{cases} \quad (1.19)$$

For isotropic scattering,  $g = 0$  so:

$$\cos\theta = 2\xi - 1. \quad (1.20)$$

### 1.3.3.2 MC modeling of Fluorescence Propagation

Fluorescence modeling requires the consideration of an additional parameter, fluorescence quantum yield, to describe the probability of a photon packet to be absorbed by a fluorophore molecule, which causes the conversion to a fluorescence photon of a different wavelength and directionality. The initial direction of the fluorescence photon is isotropic because of the nature of fluorescence emission [33].

Figure 1.8 illustrates the MC modeling of fluorescence propagation in tissues with some new steps added to the general MC modeling. After launching a photon packet with optical properties at the excitation wavelength, there is a chance for a fluorescence photon to be generated upon the absorption of an excitation photon after a time delay. This probability is defined by the quantum yield and the time-delay is defined by the lifetime of the fluorescence light. The rest of the procedure involves a general MC simulation to simulate fluorescence light propagation with optical properties at the emission wavelength. Fluorescence simulation is typically much more time-consuming than the simulation of diffuse reflectance due to extra fluorescence photon propagation [33].

The theory of MC simulation is briefly explained in this section. The MC method is necessarily statistical and therefore requires intensive computation time to achieve the desired precision. However, its flexibility and recent advances in improving the speed, makes it a standard and powerful tool in the field of tissue optics for simulated measurements of photon transport. In our work, we used the MC method to simulate the light distribution in the forward model. For more detailed explanation on MC simulation, the reader is referred to literatures [30], [32], and [33].

In the next chapter, advantages and disadvantages of some of the optical imaging techniques are reviewed.

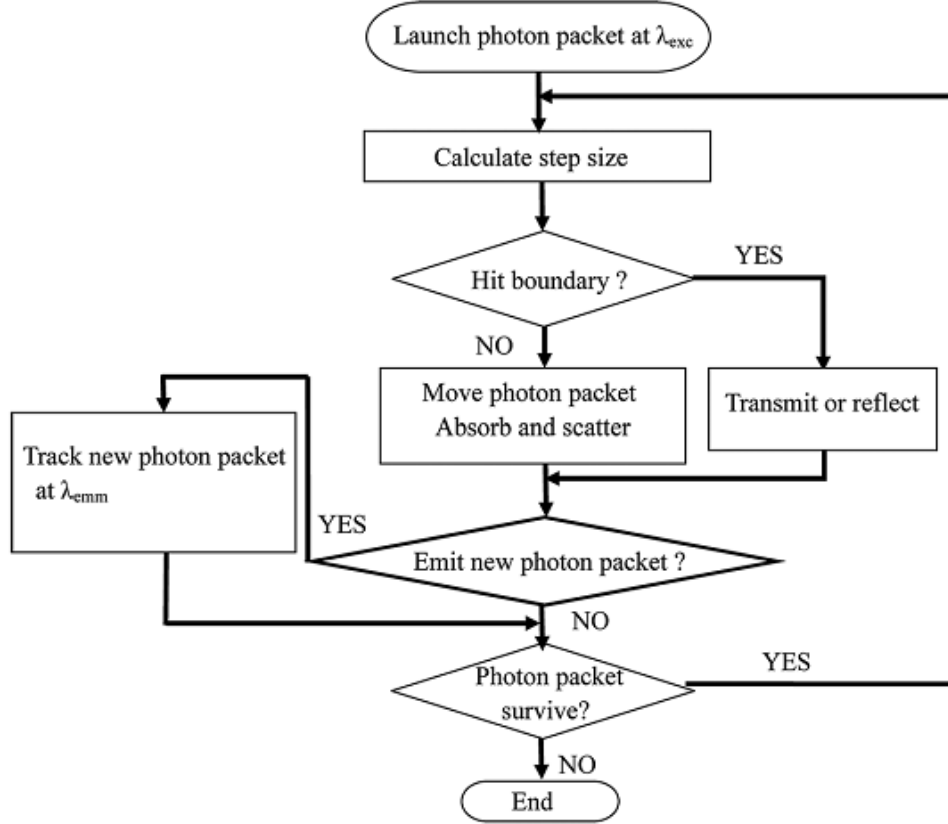


**Figure 1.8:** Flowchart for the fluorescence Monte Carlo modeling.  $\lambda_{exc}$ : excitation wavelength and  $\lambda_{em}$ : emission wavelength. A photon packet at the excitation wavelength is launched. The fluorescence photon is generated upon the absorption of an excitation photon. Fluorescence light propagation with optical properties at the emission wavelength is simulated [33].

---

## Chapter 2

### Overview of Optical Imaging Approaches

Optical imaging techniques have emerged as non-invasive, fast, yet robust alternative to conventional methods of medical imaging, in both clinical applications or laboratory research. A main challenge for optical imaging instrumentation is overcoming the effect of light scattering and absorption by tissue, which limit the penetration depth and degrades the resolution. Depending on the penetration depth and resolution, imaging technologies can be categorized into microscopic, mesoscopic and macroscopic scales.

In microscopic imaging technologies, the detected light is only minimally scattered, so it can provide cellular or subcellular level imaging resolutions ( $< 1\mu m$ ) but with a limited penetration depth of a few hundred microns. This includes: Confocal Microscopy (CM), Multi-photon Microscopy (MPM), Photoacoustic Microscopy (PAM), and Optical Coherence Microscopy (OCM). On the other side, macroscopic imaging technologies, utilize light to image large tissue volumes such as a whole organ or even whole body. These technologies typically have penetration depth of several centimeters, but their resolutions are limited to several tens to hundreds of micrometers. Macroscopic imaging technologies include: X-ray, Computed Tomography (CT), Positron Emission Tomography (PET), Single-photon Emission Computerized Tomography (SPECT), Magnetic Resonance Imaging (MRI), Ultrasound (US), and Diffuse Optical Tomography (DOT). Finally, Mesoscopic imaging technologies bridge the gap between microscopic and macroscopic technologies with the imaging depth of millimeters scale and resolution of few to hundred microns. This regime includes: Optical Coherence Tomography (OCT), Laminar Optical Tomography (LOT), Fluorescence LOT (FLOT), Fluorescence Coherence Tomography (FCT), and Photoacoustic Tomography (PAT) [34][35]. Figure 2.1 shows a schematic comparison between the above mentioned



techniques in terms of spatial resolution and depth of penetration.

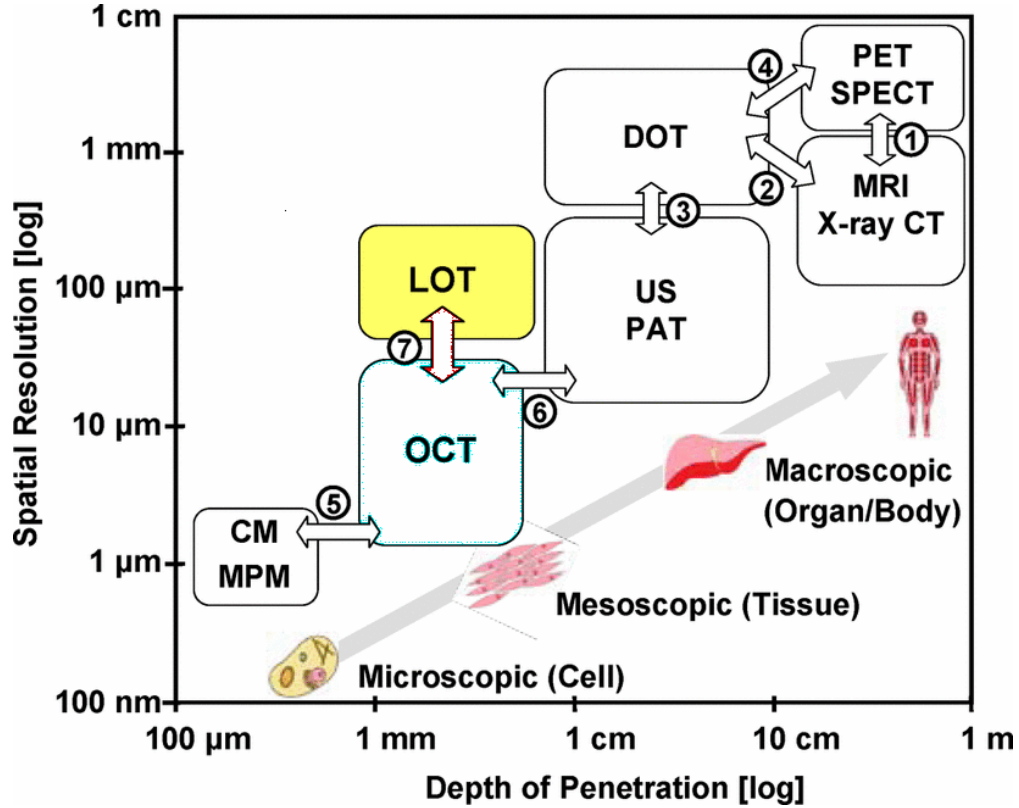


**Figure 2.1:** A comparison between different imaging modalities in terms of spatial resolution and depth of penetration [34].

In this chapter, we continue with a quick review of some of the microscopic and mesoscopic techniques, continuing on reviewing some basics of fluorescence imaging and then will mainly focus on LOT, a non-contact laser-scanning imaging technique, which incorporates the effect of scattering to probe fluorescence contrast in living tissues in the range of 2mm with the resolution of about  $200\mu m$ . Optogenetics, as one of the applications of Fluorescence LOT is then reviewed.

## 2.1 Confocal Microscopy

Confocal microscopy (CM) [37][38] increases optical resolution ( $< 1\mu m$ ) by reducing the amount of scattered light detected, with isolating signal from the focal point of a scanning

laser beam. It uses a point light source that is focused and scanned on the tissue, with a pinhole placed in front of the detector. The use of the pinhole rejects out-of-focus multiple scattered light from reaching out the detector. The fluorescent or reflected light detected, is then used to build up a high-resolution two dimensional (2D) image of the tissue. It is possible to reconstruct a three dimensional (3D) structures by stacking individual 2D images at different depths [36]. However, the limitation of CM is that it cannot image the tissue at depths of more than 300 microns, as the likelihood of scattering events occurring becomes too great and the confocal images become blurred once the focus of the beam is positioned too deeply [35].

## 2.2 Two-photon Microscopy

Two-photon microscopy (TPM) [39][40] provides high-resolution (submicron) imaging with deeper tissue penetration ( $500 - 600\mu m$ ) than confocal microscopy. In the two-photon process, a molecule simultaneously absorbs two photons, which their individual energies are only half of the energy state needed to excite that molecule, and then releases the energy to an emission photon [36]. TPM uses longer wavelength light for excitation (means less scattering and absorption in tissue) and a pinhole is not needed in the detection path, therefore it can provide deeper penetration depth than CM [25]. TPM is typically using for imaging fluorescent contrast and is able to image conventional fluorophores such as green fluorescent protein (GFP), nicotinamide adenine dinucleotide (NADH) and flavin adenine dinucleotide (FAD).

## 2.3 Optical Coherence Tomography

Optical coherence tomography (OCT) [41][42] is a technique for obtaining subsurface images, up to 1-2mm depth, with high resolution in the range of  $1 - 10\mu m$ . It uses low-coherence near-infrared light to record volumetric images of biological tissues. OCT is based

on the Michelson - Morley interferometer where light is interfered with itself in order to precisely determine distances. Interferometry facilitates the measurement of the echo time delay of back-scattered or reflected light from the tissue. When the two path lengths are exactly same, a constructive interference pattern emerges, which is detected as some increase in the amplitude. By changing the length of the reference path, it is possible to record the data from different depth to build up a 3D image of the tissue [43][44]. OCT's main mechanism of contrast is back-scattering or back-reflection from interfaces within the tissue, rather than absorption. The reliance of OCT on the coherence of the detected light makes it unsuitable for fluorescence imaging [35].

## 2.4 Diffuse Optical Tomography

Diffuse Optical Tomography (DOT) [45] utilizes light in the near infrared spectral range ( $650 - 1000nm$ ) to probe deeper regions (several centimeters) in biological tissues such as breast or brain. However, as a trade-off between depth and resolution, DOT has lower resolution, in the order of millimeter or submillimeter, compared with most other imaging techniques. On the other hand, DOT has the unique advantage of high sensitivity to specific biomolecules and fluorophores, by probing absorption as well as scattering properties of biological tissues, so can provide spatial distributions of intrinsic tissue optical properties or molecular contrast agents through model-based reconstruction [34]. Image reconstruction in DOT involves both forward and inverse problems, and the diffusion approximation is usually used to predict the light propagation in the forward model [11].

## 2.5 Fluorescence Imaging

We covered the basis of fluorescence as a source of imaging contrast in chapter 1. Fluorescence imaging has received particular attention recently due to the increasing availability of fluorescent dyes, which can be detected at low concentrations without using harmless

radiations. With fluorescence imaging we are able to investigate the tissue in different applications, both anatomically or functionally, in a noninvasive manner.

Fluorescence contrast agents, the molecules that produce the fluorescence light, are classified in two main categories: endogenous and exogenous. Some biological substances possess intrinsic fluorescence that originates from chromophores, known as endogenous fluorophores or autofluorescence. Intrinsic fluorescence can be used for diagnostic applications or for understanding the mechanisms of molecular interactions. Endogenous fluorophores are generally associated with the structural proteins responsible for flexibility and rigidity of tissues and organs such as collagen and elastin, or with the cellular metabolism such as FAD (Flavin Adenine Dinucleotide) and NADH (Nicotinamide Adenine Dinucleotide) [46][48].

Excitation and emission spectra of two of auto-fluorescent coenzymes, NADH and FAD, are displayed in Figure 2.2. As shown, NADH has a maximum in its excitation spectrum at 340nm and the emission maximum occur at 460nm, where FAD has its excitation maximum at 448nm and a maximum in the emission spectrum at 520nm [27]. We used the FAD for our phantom studies. Understanding the difference between these wavelengths is very important for the proper design of optical systems.

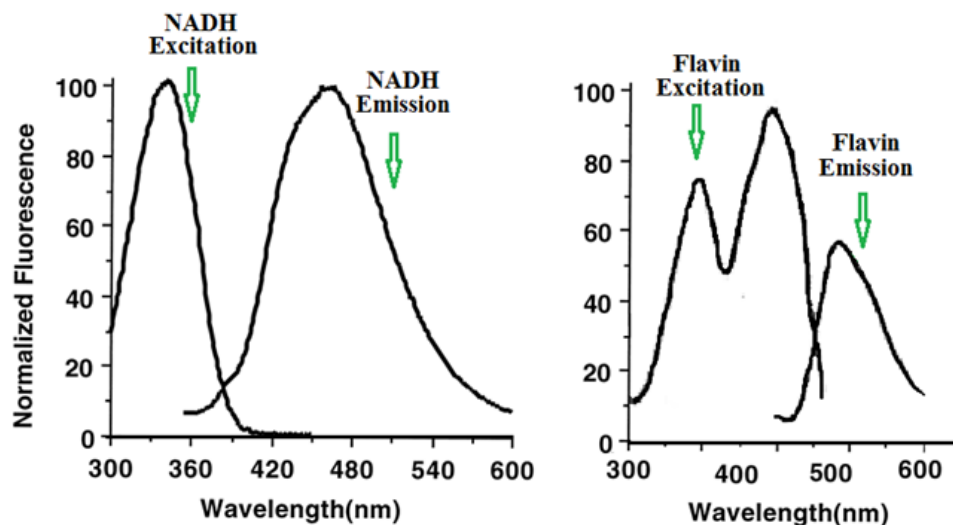


**Figure 2.2:** Excitation and emission spectra of NADH (left) and FAD (right). NADH excitation maximum happens at 340nm and the emission maximum is at 460nm. FAD excitation maximum is at 448 nm and the emission maximum is at 520nm [27].

The main shortcoming of endogenous fluorophores is that their signals are usually weak and nonspecific due to their low excitation and emission wavelengths. For shorter wavelengths, tissue absorption is relatively high and the depth of penetration is limited. To solve this problem, exogenous fluorescence probes have been developed to provide distinct fluorescence information related to physiological, cellular or molecular processes in living tissues. The advantage of exogenous probes is that they are extremely diverse and cover a large spectral range of wavelengths from 250nm to almost 1200nm [48]. Exogenous fluorescence probes have the ability of targeting specific cellular or subcellular events and this ability differentiates them from nonspecific dyes [46]. Two examples of exogenous fluorescence probes are green fluorescence proteins (GFP) and yellow fluorescence proteins (YFP). Excitation and emission spectra of GFP, which is used in our in-vivo studies, is shown in Figure 2.3.

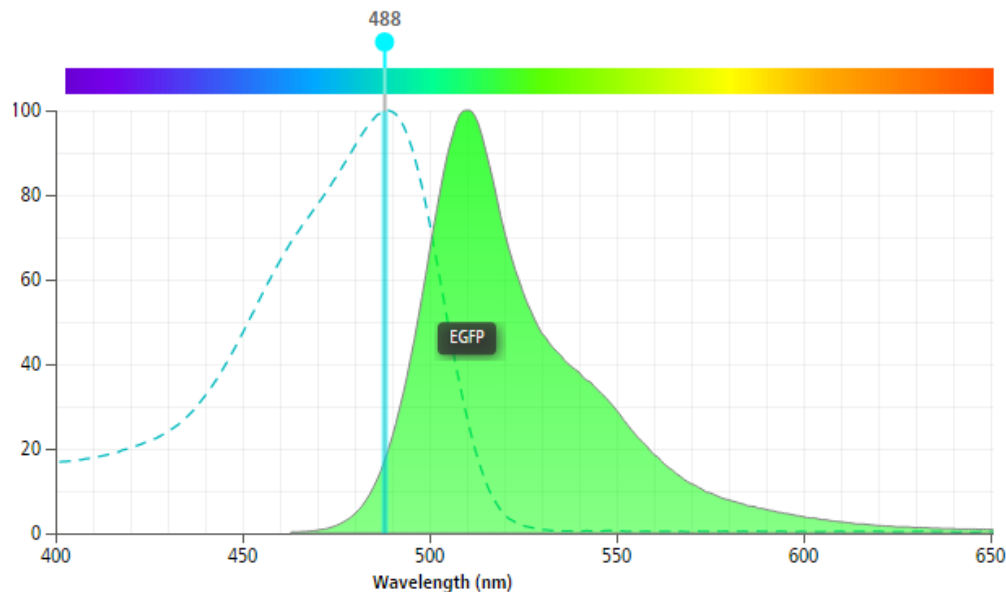


**Figure 2.3:** Excitation and emission spectra of Green Fluorescence Protein (GFP) [47] .

In principle, the basis of fluorescence imaging is fairly straightforward: using an external light of specific wavelength to excite fluorescent molecules in the sample, which is followed by the release of longer wavelengths, lower energy light, called emission. The final goal of fluorescent imaging is the detection of fluorescent emission using appropriate techniques and optical equipment. Typical components of a fluorescence imaging device are shown in

Figure 2.4: a light source, the excitation filter, the dichroic mirror or dichroic beamsplitter, the emission filter, detectors, and objective lens. The dichroic and filters should be chosen to match the excitation and emission spectra of target fluorophores.

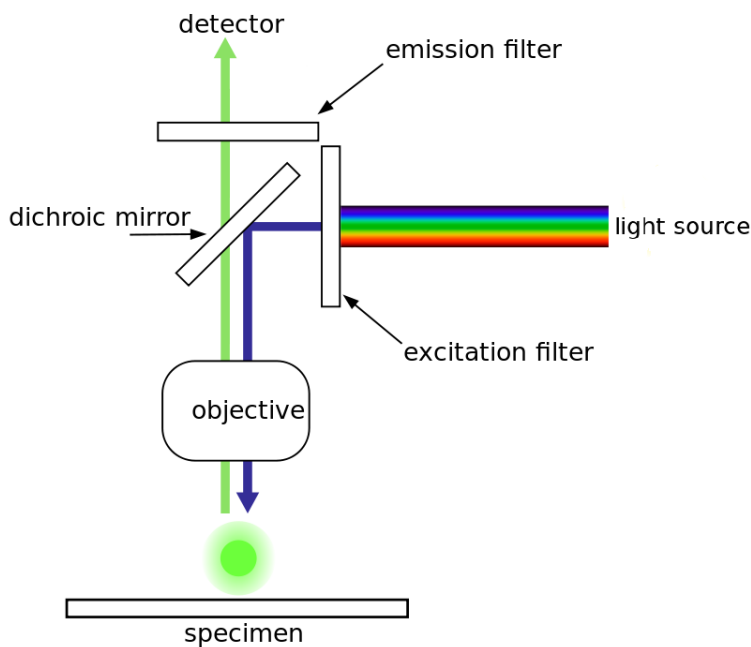


**Figure 2.4:** A typical fluorescence imaging optical set up [20].

The main challenge here is the delivery of excitation light in a way that it reaches fluorescent molecules, despite the inherent absorption and scattering properties of the tissue, and then detecting the emission light, which is usually a faint and weak signal. The positive side is that fluorophores can be excited continuously and there is no signal decay limiting the excitation. However, in some cases, photobleaching might happen, which is when the fluorescent molecules accumulate chemical damage from the electrons excited during fluorescence. Using more robust fluorophores, minimizing illumination time, or using photoprotective scavenger chemicals can help reducing photobleaching probability [20].

In vivo fluorescence imaging can provide information at a wide range of resolutions and imaging depths, from micrometers in subcellular level (microscopy) to centimeters in small-animal whole-body imaging (fluorescence reflectance imaging and fluorescence molecular tomography) [49]. In microscopic techniques, fluorescent dyes are usually used for monitoring

the distribution of chemicals throughout the cell by taking microscopy images of the cell, loaded with the dye. Viability studies on cell populations (alive or dead), imaging the genetic material within a cell (DNA and RNA), and viewing specific cells within a larger population also can be determined using fluorescence microscopy. Macroscopic imaging allows us to study mostly the interactions between cells and provides a platform much closer to true in vivo analysis in terms of structural architecture on microscopic and macroscopic scales [46].

In vivo fluorescence imaging is a growing field encompasses a wide range of different techniques such as fluorescence confocal microscopy (FCM), plan reflectance imaging, fluorescence molecular tomography (FMT), and diffuse optical tomography (DOT). For more information the reader is referred to literatures [46][50][51].

## 2.6 Laminar Optical Tomography

Laminar optical tomography (LOT) was first implemented in 2004 [7], as a mesoscopic imaging technique, which incorporates the measurement geometry of DOT with a microscopy-based setup. LOT performs depth-resolved 3D functional imaging offering  $100 - 200\mu\text{m}$  resolution and the frame rate of 100 fps, effective over the depth up to 2.5mm. It was initially developed for multi-spectral imaging of rat cortex where its use on thinned skull rat cortex was demonstrated in 2007 [2][52]. Since then, several advances have been made to the technique such as using it for fluorescence imaging [8][53] or integrating it with other techniques such as OCT [54]. LOT also can be used in other in-vivo imaging applications such as imaging of skin [55][56], heart [35], retina [57] or dental applications [58].

LOT uses a non-contact laser scanning setup [2][7][8][25] similar to confocal microscopy, to raster scan a focused beam of light on the surface of the tissue. Laser beam passes through a couple of lenses and is illuminated on the surface of the tissue using a pair of moving galvanometer mirrors and again the returning light is descanned using the same mirrors. Returning light is detected from both the focal point of the scanning beam, and

also at a series of increasing distances ( $0 - 1.5mm$ ) from the beams focus, using an array of seven photodiode detectors. Usually light beams that scatter more in the tissue, travel deeper through the tissue and are detected further away from the illumination point. This measurement geometry allows features at different depths to be distinguished for producing the raw data. Using an appropriate model of light transport and reconstruction method, raw measurements can be converted into 3D images.

As mentioned, LOT is similar to confocal microscopy in using non-contact laser scanning setup. However, unlike confocal microscopy, it does not have a pin hole for Z-scanning the ballistic light. Instead, it achieves its depth-resolution by measuring both confocal and multiply scattered light emerging from tissue, for a variety of source and detector positions in a similar way to DOT configuration. The light measured in LOT is not diffused yet and source-detector separations are much less (hundreds of microns) than in DOT (few centimeters) [8]. Therefore, LOT is an incorporation between these two techniques by providing higher resolution than that of DOT (with less penetration) but deeper penetration than confocal microscopy (with lower resolution) [25].

LOT is able to measure both absorption and fluorescence in the tissue. For absorption measurements, the illumination light is the same wavelength as the detected light, while for fluorescence measurements different filters and dichroic mirror should be used to separate the two different excitation and emission wavelengths. Compared with OCT, LOT has lower spatial resolution but is able to penetrate deeper well beyond the scattering limits of tissue and can be used for fluorescent imaging. OCT suffers from poor sensitivity to absorption contrast because it isolates only coherently backscattered light. It also cannot be used for fluorescence imaging since it is not sensitive to fluorescence contrast [8][2].

Chapter 3 is devoted to describing the measurement geometry of LOT, the basic components of an LOT system, and the analysis of LOT data in more details.



## 2.7 Optogenetics

The project presented here, has the final goal of providing a new set of optical tools for imaging the fluorescence distribution in living tissues. The application of the developed technology is not limited to optogenetics, but it can be used as a powerful tool to help improving the precision and accuracy of neuroscience and optogenetic experiments. Many neuropsychiatric disorders benefit from understanding how specific brain cell types and neurons are connected and function as a part of a larger network of neurons in the brain [59]. Optogenetics is a neuromodulation method, which involves genetic and optical techniques to monitor, control and measure the activities of specific cells or neurons within a living tissue [9][20][60]. With a high temporal resolution (in the order of milliseconds) and cell-type-specific precision, optogenetics is able to probe how the nervous system functions in real-time, even in freely-moving animals.

During optogenetic experiments, a major common challenge that neuroscientists faced is the need to precisely control one type of cell in the brain, while leaving the activities of others unchanged. Methods like using electrodes or drugs were not good enough, as electrodes cannot be used to precisely target defined cells, especially in moving animals, and drugs act too slowly. Advances in optogenetics have opened new windows in neuroscience, and even beyond neuroscience, by addressing and solving the need for controlling defined events in specific cell types in intact systems [61][62]. Some primary benefits of optogenetic stimulation over the conventional electrical method are: the ability of specific cell-type targeting, bidirectional control of cellular activity for both activation and inhibition of the neurons and high spatial and temporal resolutions [9].

In optogenetics, cell-types of interest are genetically modified by expressing light-sensitive proteins adapted from microbial opsin tagged with a fluorescent protein. Once these proteins are expressed, we are able to use light of appropriate wavelengths to manipulate, increase or suppress, neural activity of specific neurons on command [9][61]. For confirming that

the proteins are expressed within the specific cells, we can combine optogenetics with other optical devices such as FLOT, which is able to record the fluorescence distribution in the brain.

In general, optogenetic approach requires: (1) engineered control genetic tools to target specific cells of interest (such as microbial opsin genes tagged with a fluorescent protein), (2) appropriate technology for delivering light into tissues under investigation, and (3) obtaining compatible readouts and performing analysis on the neural activity using fluorescent indicators (intrinsic or genetically encoded), electrical recording, fMRI or other technologies [60][62].

The foundation of the optogenetic technology is based on two microbial opsins, channelrhodopsin-2 (ChR2) adapted from an algae, and halorhodopsin (NpHR) adapted from a bacteria. Co-expression of these proteins enables bidirectional control of cellular activities (activation or inhibition) with high temporal and spatial resolution. ChR2 is a monovalent cation channel, when illuminated with blue light ( $\sim 470\text{nm}$ ) regulates the flow of positively charged ions by permitting the entry of sodium ( $Na^+$ ) ions into the cell and exiting the potassium ( $K^+$ ) ions to the outside of the cell. NpHR is a chloride pump, when stimulated with yellow light ( $\sim 580\text{nm}$ ), regulates the flow of negatively charged ions by facilitating the transport of chloride ( $Cl^-$ ) ions by overcoming the membrane potential of the cell (Figure 2.5(a)). The action spectra of the ChR2 and NpHR are shown in figure 2.5(b). Since there is a 100nm difference between the peak sensitivity of the ChR2 and NpHR spectrums, bi-directional control of cells is possible by using the blue light to drive the action potential and yellow light to suppress the neural activity without considerable interference (Figure 2.5(c)) [59].

Next requirement to modulate the activity of neurons is finding a suitable method of light delivery to the region of interest. There are different methods depending on the requirements of the application, but the most common one is using a thin optical fiber ( $100 \sim 200\mu\text{m}$  diameter) implanted on the skull through a cannula guide (Figure 2.6). This method is suitable to stimulate both superficial and deep brain tissue [59]. However, its field of stimu-

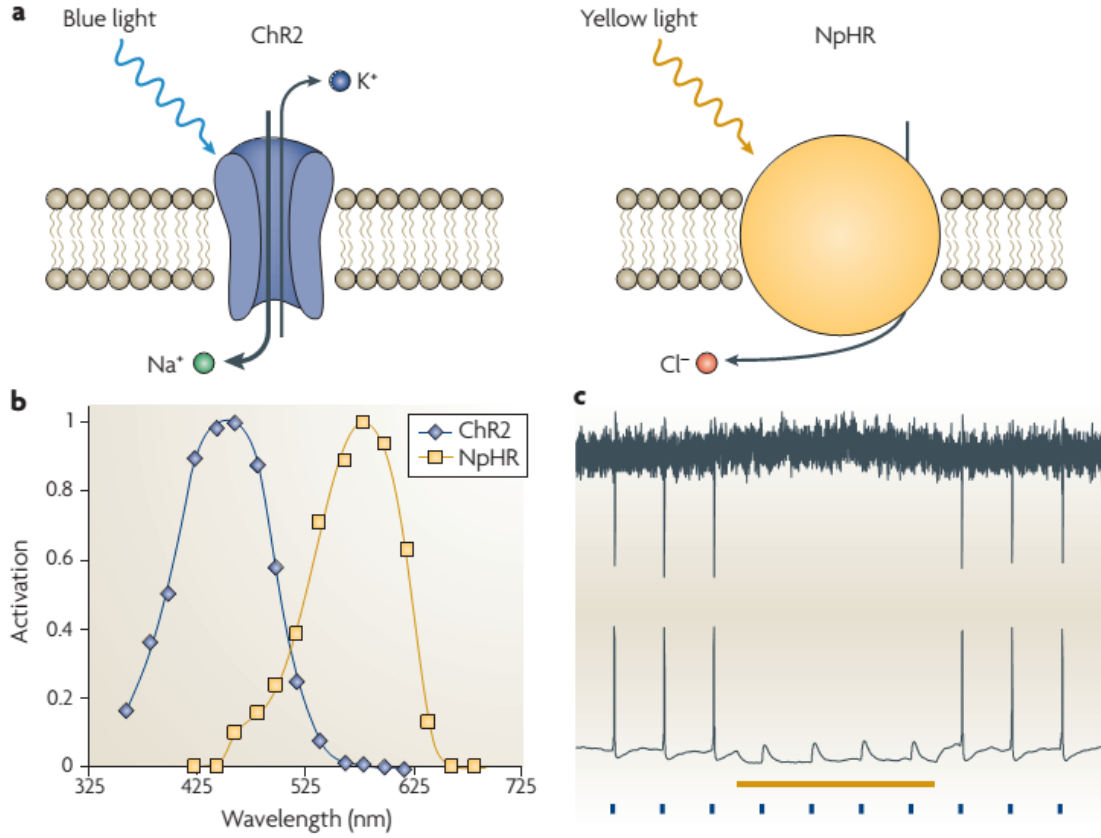


**Figure 2.5:** (a) ChR2 (channelrhodopsin) allows positive sodium ( $\text{Na}^+$ ) and potassium ( $\text{K}^+$ ) ions to pass through the channel in response to blue light exposure. NpHR (halorhodopsin) regulates the flow of negative chloride ( $\text{Cl}^-$ ) ions in response to yellow light. (b) Action spectra for ChR2 and NpHR, separated by 100nm. (c) Spike trains of neurons; blue light flashes cause action potential in the neuron, while yellow light exposure inhibits the activity of the neurons [59].

lation is limited to the area close to the fiber tip, due to the light absorption and scattering inside the tissue. For controlling the light distribution in the brain, more advanced light delivery mechanisms are needed, such as making an array of channel waveguides where each waveguide terminates at a different depth or moving an optical fiber inside the tissue [9].

Final step for optogenetic experiments is designing an appropriate readout technology. A common method for this purpose is by using electrodes. However, one of the deficiencies of electrical stimulation/recording is that the simultaneous input/output processing is not typically possible due to artifacts associated with electrical stimulation [62]. Combining optogenetics with electrodes provides a powerful tool for optical stimulation and parallel

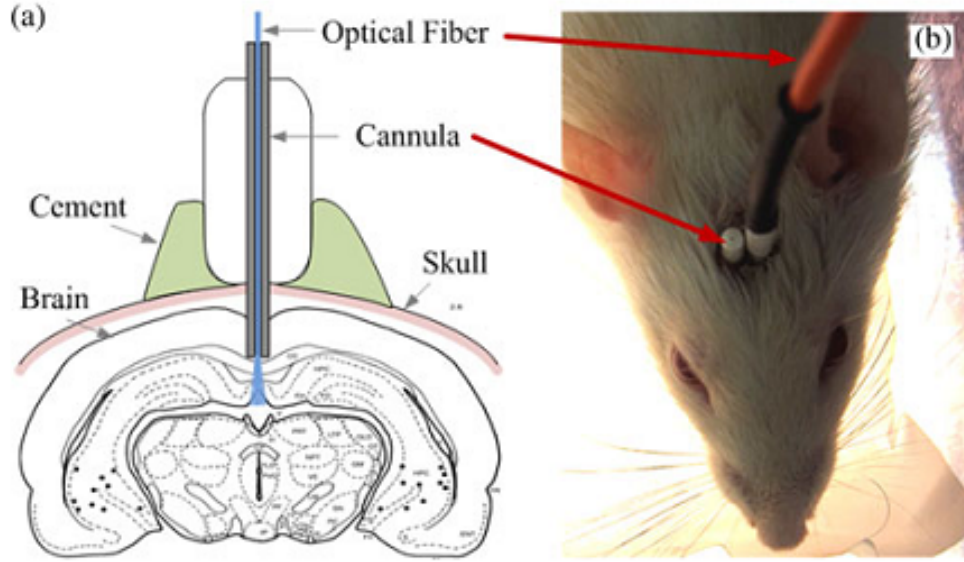


**Figure 2.6:** (a) Optical fiber implanted in the brain tissue through a cannula guide, to deliver light and stimulate the targeted brain region. (b) A rat receiving two implants in the motor cortex on both hemispheres [9].

recording of the neural activities. Although, we still need to make sure that the recorded signal is not an artifact resulting from the direct effects of light and temperature on the recording electrode [63]. Since the stimulation is based on light, it is now possible to target individual or large networks of neurons, simply by exposing them to appropriate wavelengths (Figure 2.7).

Another approach for reading the neural activity during optogenetic stimulation is based on the fluorescent proteins (FP). Fluorescent proteins can convert a physiological signal in the form of the changes in the ions concentration, membrane voltage or pH level, to the fluorescent output [64]. For example, action potential in the cell is associated with influx of the intracellular calcium ( $\text{Ca}^{2+}$ ), and detection of the calcium ions can be an indicator of the neural activity [65].

Fluorescent proteins can also be served as bio-markers to provide a tool for confirming the expression of the light-sensitive proteins such as ChR2 or NpHR after virally transfection. Proper expression of the light activated proteins is essential for any successful optogenetic experiments. For this purpose, microbial opsin genes tagged with a fluorescent protein (such

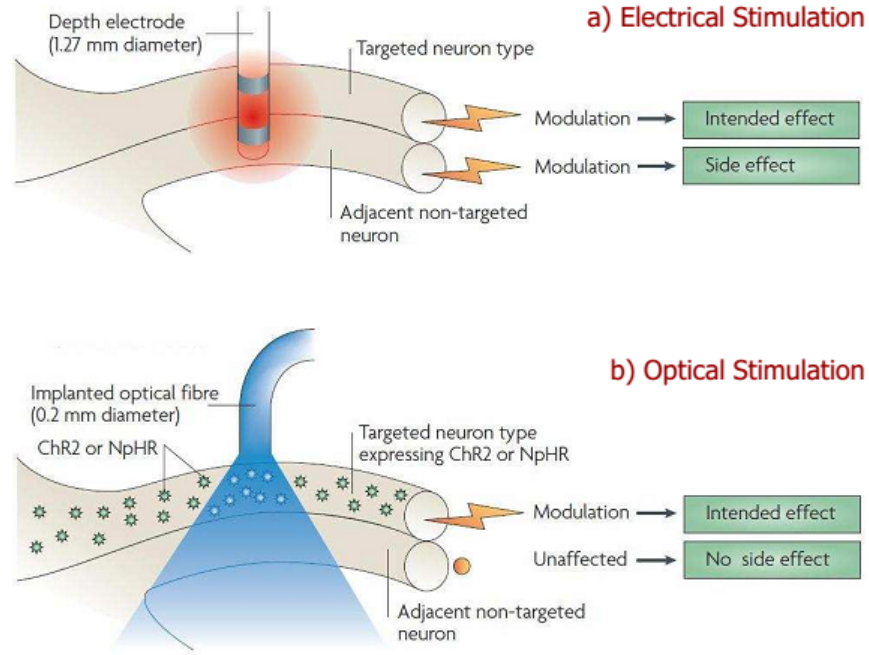


**Figure 2.7:** Diagrams comparing (a) electric neural stimulation and (b) optogenetic stimulation. In optogenetics, cell-type targeting of the neurons is possible. [59].

as YFP or GFP) are delivered and co-expressed in cells. If the expressed fluorescent proteins is illuminated with the light of appropriate wavelength (e.g., blue light), they emit fluorescent light, which indirectly confirms the expression of the light activated proteins.

Figure 2.8 (a) shows the schematic of the tagged ChR2 with green fluorescence protein (GFP). The GFP can be excited with the blue light and the emitted green fluorescent signal can be captured for the imaging purpose. The conventional method of confirming the expression of the light sensitive proteins is by sacrificing the animal, extracting and slicing the brain tissue and then detecting the fluorescence distribution using common fluorescence microscopy techniques. In Figure 2.8 (b), the microscopic image of a rat brain slice, which is labeled with GFP, is shown.

Our developed FLOT has the advantage of being able to monitor and reconstruct the position and depth of fluorescence distribution in the tissue. In our experiments we excited the brain using blue light (450nm laser) and were able to monitor and extract the XYZ coordinates of the GFP distribution to confirm appropriate expression of the light sensitive

opsins in the brain of small rodents.

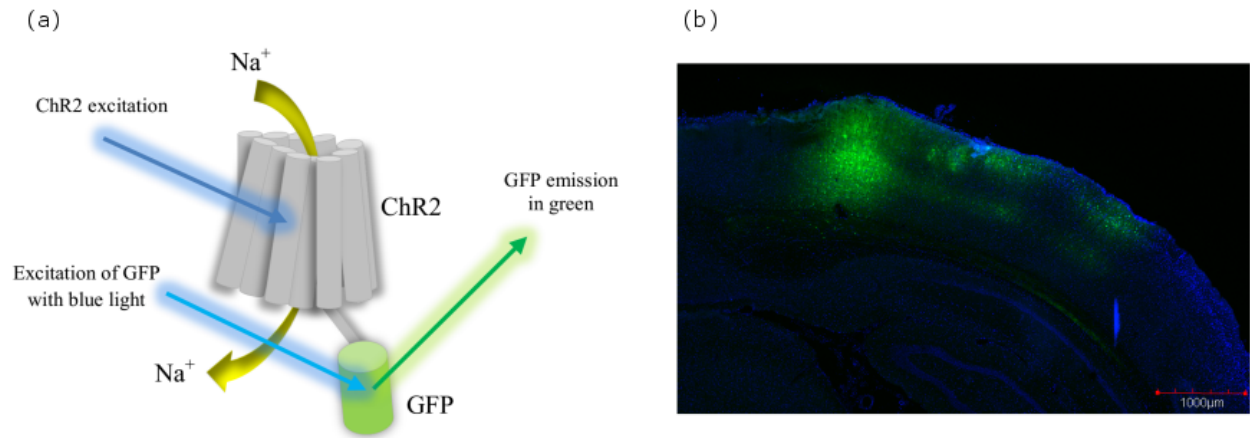


**Figure 2.8:** (a) Schematic of the tagged ChR2 with green fluorescence protein (GFP), (b) the confocal microscopy image of a rat brain's slice, which is labeled with GFP.

---

## Chapter 3

### Instrumentation and detection principles

This chapter describes the development of our FLOT system for fluorescence imaging. We will cover the measurement configuration, hardware design (optical layout), controlling software, raw data analysis, image reconstruction, and reconstructed data representations. FLOT provides a relatively simple system to image superficial fluorescent objects in a highly scattering medium like the brain tissue, up to 2 mm depth.

#### 3.1 Measurement Configurations

As we covered before in sections 1.2.3 and 2.5, in fluorescent imaging, the fluorophore is excited by light of appropriate wavelength within its absorption spectrum and then the emitted light, which has a longer wavelength, is detected by a detector. Therefore, the first step toward the system design is determining source-detector configurations. Typically in optical tomography, there are two main source-detector configurations for detecting light at known distances from point sources: reflection and transmission geometries (Figure 3.1).

In reflection geometry, source and detectors are defined on the same side of the medium at a distance  $\rho$ . Usually light is delivered through a fiber connected to a laser source and is detected by a photo-multiplier tube or an avalanche photo-diode. In the transmission geometry, sources and detectors are placed on the opposite sides of the sample and light detection is done using either a fiber or a lens mounted on a CCD camera system [66].

In a LOT system, the reflection geometry is adapted therefore, all of the sources and detectors are placed on one side of the tissue. The excitation light is delivered in the form of a point source [7] or line illumination [54]. In both cases, measurements are acquired by

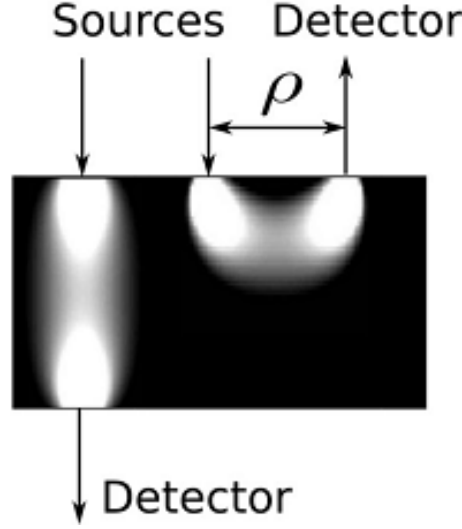


**Figure 3.1:** Banana patterns of light penetration in the medium in the reflection and transmission geometries. As a rough rule of thumb, the mean depth of light penetration in the reflection mode is  $\rho/2$  [66].

scanning a focused laser beam over the surface of the tissue (source position) and collecting the returning light at detector positions close to the source coordination. The distance between the illumination and detection points is known as source-detector (SD) separation.

LOT is able to detect both confocal and multiple scattered light emerging from the surface of the tissue at various distances away from the illumination point. In our design, detectors are defined at 7 (or 9) fixed distances away from the scanning spot in the range of 0 to 1.6mm (1 confocal spot and 6 to 8 neighboring spots). For higher SD separations, light has scattered more and travelled deeper and provides information about the deeper parts of the tissue. After a full scan, we have the raw data of seven different SD separations, each with a different weighted depth-sensitivity. Using these measurements with an appropriate method of light propagation and image reconstruction, we are able to reconstruct 3D images revealing the fluorescence distribution in the tissue [2].

Our FLOT system is designed based on the line illumination technique (Figure 3.2(b)). We used an EMCCD camera to acquire data along the lines parallel to the illumination pattern, which reduces the scanning time significantly, since only 1D scanning is required to acquire 3D information. Seven (up to nine) lines of source-detectors ( $D_1$  to  $D_7$ ) are defined



with 0.2 mm separation from 0 to 1.2mm (up to 1.6mm). In traditional LOT systems with point illumination (Figure 3.2(a)), fast photo-detectors are required to acquire high resolution data and reduce the scanning time. In this case, 3D images are obtained through 2D raster scanning of the illumination point. The SD separations are fixed and limited to the fiber's diameter ( $200\mu m$ ) in conventional LOT, while in our case we are able to decrease the SD separations to  $16\mu m$ , which is the pixel size of the camera.

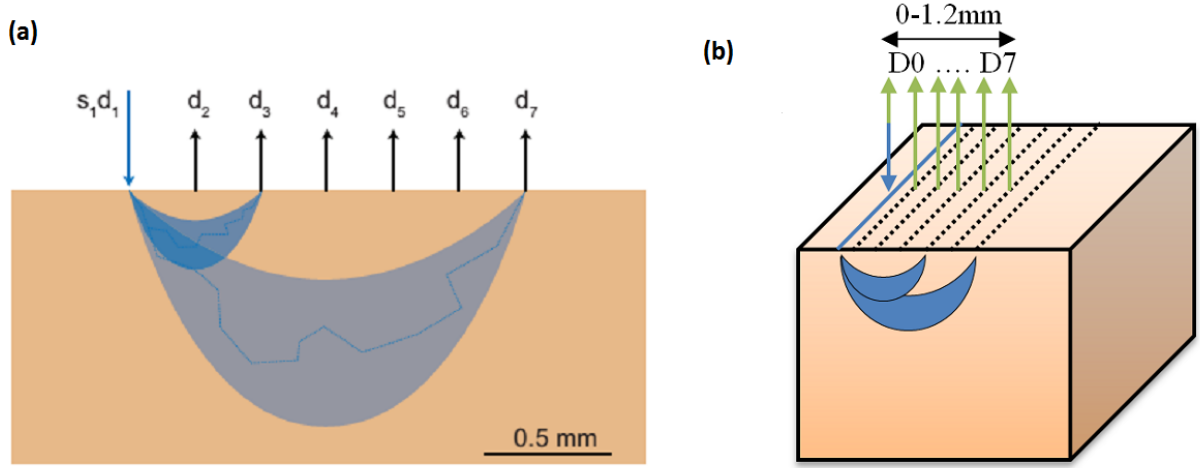


**Figure 3.2:** LOT measurement geometry and source-detector configurations. (a) Point illumination [25]. (b) Line illumination.

The number of measurement configurations is physically limited because of memory consumption for reconstructing the 3D volumetric images. In our case, each pixel of the EMCCD camera could be considered as one detector ( $512 \times 512$  pixels). However, only a certain number of pixels are used in each direction to define the lines of source-detectors. Therefore, while acquiring as much information as possible, the size of the matrix we will be using for the reconstruction would not be too large.

## 3.2 Hardware Design

Figure 3.3 shows the schematic diagram of our FLOT setup. The tissue is excited using a blue light (450nm single mode pigtailed laser diode, Thorlabs Inc., Newton, NJ) and the

fluorescent emission (530nm) is captured. The blue laser is collimated and passed through a cylindrical lens (LJ1695RM, Thorlabs Inc., Newton, NJ) to be expanded for line-field illumination, and then hits a dichroic mirror (FF440/520-Di01, Semrock, Rochester, NY). Wavelengths shorter than a threshold (excitation light) pass through the dichroic mirror, and wavelength longer than that threshold (emission light) reflect toward the imaging components of the system. The excitation light, after passing through the dichroic mirror, hits on a pair of moving X and Y galvanometer mirrors (GVS212, Thorlabs Inc., Newton, NJ). The galvanometer mirrors are controlled by the computer software prepared under LabVIEW (National Instruments, Austin, TX) to steer the collimated beam through a scan lens. The scan lens (LSM03-VIS, Thorlabs Inc., Newton, NJ) focuses the line-beam on the surface of the tissue to scan the defined field of view by converting the angular changes on one of the galvanometer mirrors into a horizontal translation of the scanning line.

The re-emitted light from the fluorophores inside the tissue travels back through the same scan lens and is de-scanned by the galvanometer mirrors. To this point, the excitation and detection path are the same; however, after reaching the dichroic beam splitter, only the emitted fluorescence light is reflected toward the light detection components of the system. To completely remove the unwanted wavelengths, we used a narrow band green optical filter in front of the EMCCD camera (Evolve 512, Photometrics, Tucson, AZ). The light entering the optical filter is a converging beam. Therefore, to prevent any error in the imaging system, a two-piece collimated emission-port adapter (XT2, Photometrics, Tucson, AZ) is used, which provides a collimated (infinity) space allowing us to place the filter wheel for using any type of optical filters in the system without sacrificing the performance or introducing optical aberrations. The architecture of the XT2 is shown in Figure 3.4. Finally, an EMCCD camera is used to acquire data along the lines parallel to the illumination pattern. Consequently, photons that travel through various depths are detected simultaneously within a shorter scanning time. The FLOT system implementation is shown in Figure 3.5 from different angles.

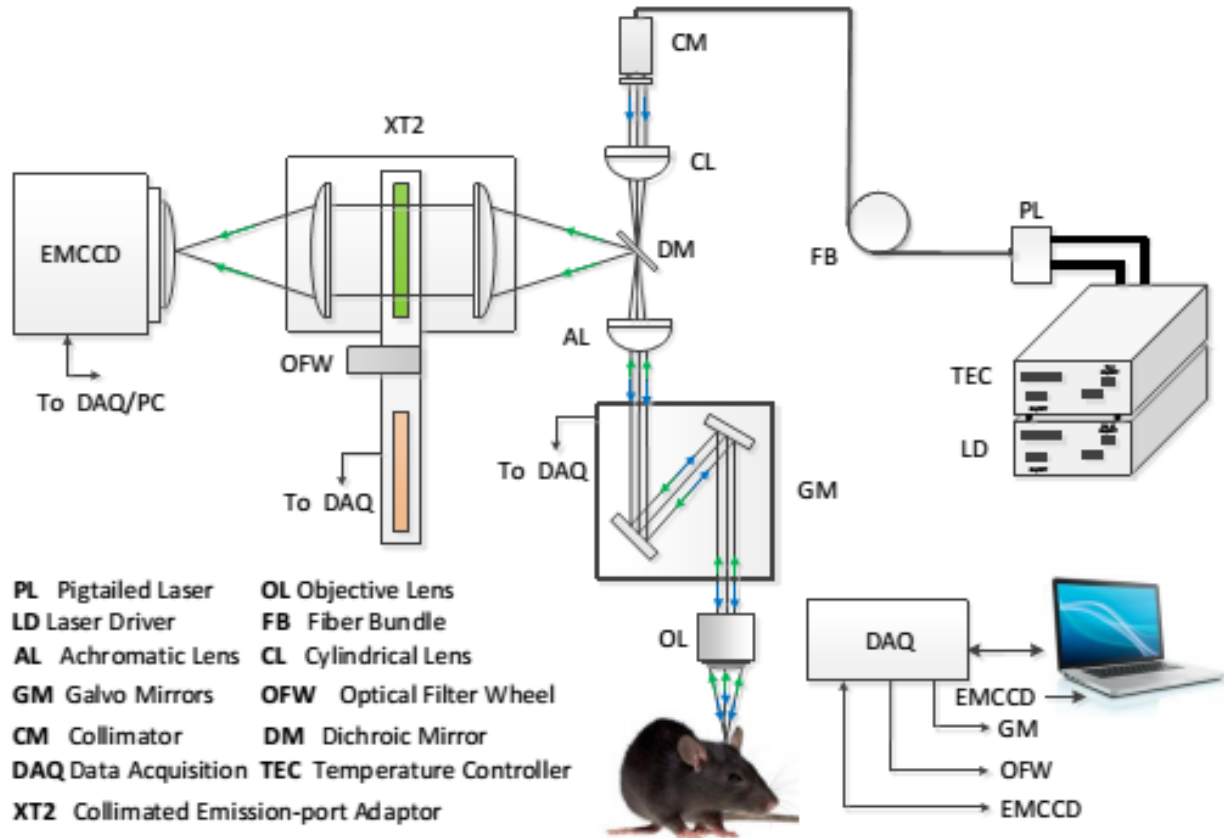


**Figure 3.3:** Block diagram of the FLOT system. Collimated laser light passes through a cylindrical lens for line illumination. Dichroic mirror separates the illumination from the imaging path. Blue light is focused on the sample using the scan lens and is scanned and de-scanned using a pair of galvanometers. Emitted light is reflected from dichroic beam splitter and passes through a narrow band filter then imaged on the CCD camera.

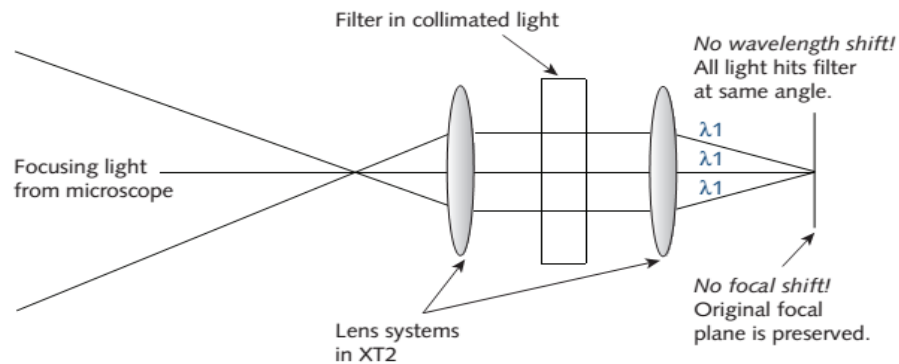


**Figure 3.4:** Schematic of the XT2 collimated emission-port adaptor [67].

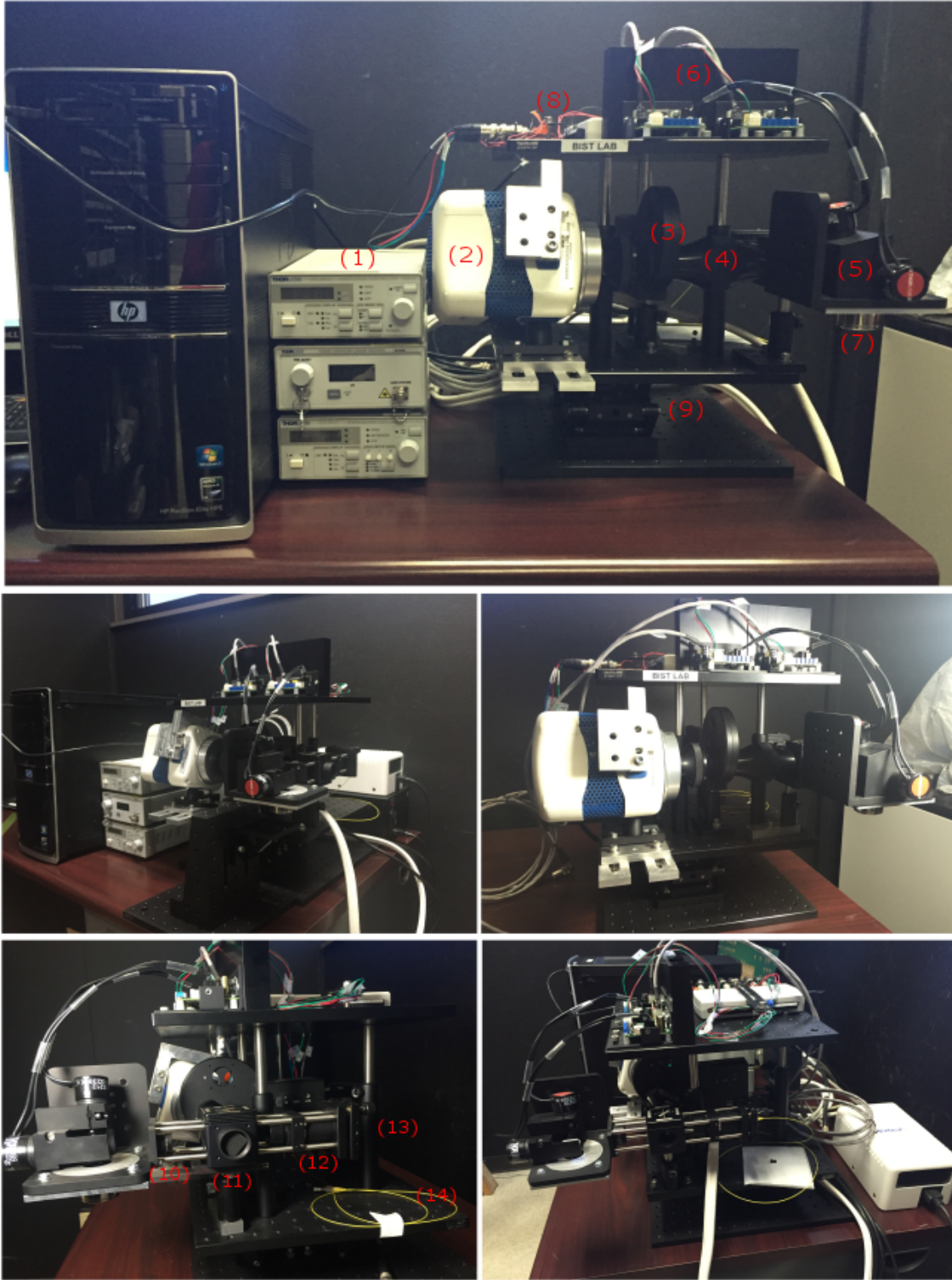


**Figure 3.5:** FLOT system implementation. (1) Laser Diode Drivers (2) EMCCD Camera (3) Filter Wheel (4) XT2, Collimated Emission-port Adapter (5) Galvanometer Mirrors (6) Galvanometer Drivers (7) Scan Lens (8) DAQ, Data Acquisition Device (9) Lab Jack (10) Acromatic Lens (11) Dichroic Beam Splitter (12) Cylindrical Lens (13) Collimator (14) Pigtailed laser diode.

The hardware, including the EMCCD camera, galvanometer mirrors, and data acquisition device, were all chosen to be compatible for the required imaging speeds. The process of scanning and data acquisition for one scan varies depending on the exposure time, field of view, and the number of images we capture. For example, one full scan including 200 images of  $512 \times 512$  pixels in a  $3\text{mm} \times 3\text{mm}$  field of view with the exposure time of 50ms, takes about 25 seconds (8 fps). We are able to increase our system's speed using a smaller field of view, lower exposure time, less number of images or less number of pixels on the camera.

The CCD camera we chose (Evolve 512, Photometrics, Tucson, AZ [67]) is implemented with 10MHz, 5MHz and 1.25MHz digitization speeds (pixels per second). The highest full frame ( $512 \times 512$ ) rate is at 10MHz, which gives approximately 31fps. With either digitizer, increased frame rate can be achieved by choosing a subregion or applying the binning. The galvanometer mirrors we chose (GVS212, Thorlabs Inc., Newton, NJ [68]), have the response time of the  $400\mu\text{s}$  for the smallest angle steps (0.2 degree); therefore, we are able to scan 2500 points/lines per second at best, which is equal to the speed of 2500fps. Finally, we have used a 16 bit DAC (National Instruments, Austin, TX [69]) with the speed of 400,000 samples per second. Considering that, the limitation comes from the speed of camera; however, the speed of 100fps can be reached easily for a  $256 \times 256$  frames without sacrificing the image quality.

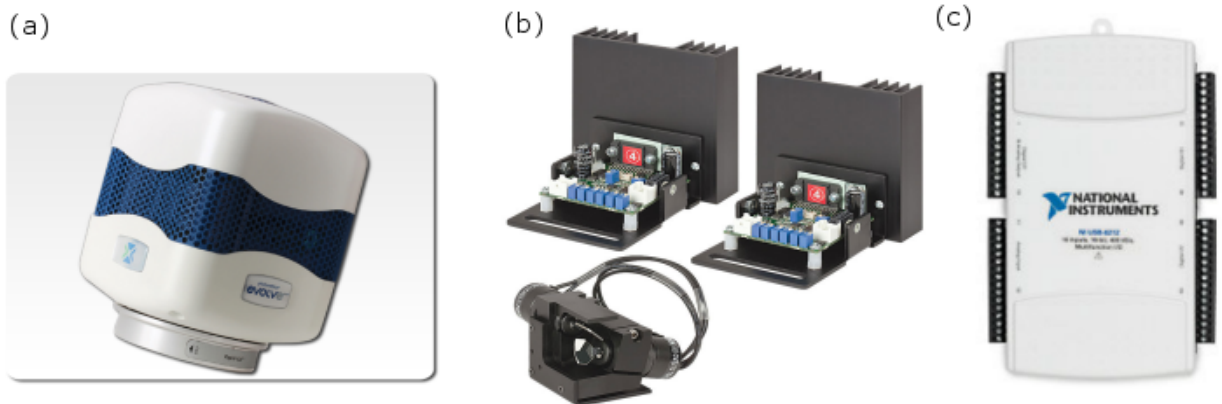


**Figure 3.6:** (a) EMCCD camera (no. 2 on Figure 3.5) [67], (b) galvanometer mirrors (no. 5 and 6 on Figure 3.5) [68], (c) data acquisition device (no. 8 on Figure 3.5) [69].

The lensing design of the FLOT system is fairly simple. As described above, in the illumination path, the collimated laser beam is reshaped to a line pattern using a cylindrical lens (LJ1695RM, Thorlabs Inc., Newton, NJ [68]) with the focal length of  $f_1 = 50mm$ . After passing through the dichroic mirror and before reaching the scan lens, an achromatic doublet lens (AC254-060-A-ML, Thorlabs Inc., Newton, NJ [68]) with the focal length of  $f_2 = 60mm$  was placed in a way that the distance between the cylindrical and achromatic lens is equal to  $f_1 + f_2$ . Therefore, a collimated line-shape laser beam is delivered to the scan lens (LSM03-VIS, Thorlabs Inc., Newton, NJ [68]) with the focal length of  $f_3 = 39mm$ . The scan lens focuses the illumination light at the sample, and collect the emitted photons.

In the imaging path, the fluorescence signal is passed through the same scan lens and achromatic doublet before reaching the Photometrics XT2 [67] lens system. As mentioned earlier, the XT2 provides a collimated space between two built-in lenses and provides space for the optical filter in the system without sacrificing the resolution of the scanner. The EMCCD camera is placed in the focal plane of the second lens of the XT2. Therefore, the output light from XT2 is imaged on the EMCCD camera sensor.



**Figure 3.7:** (a) Cylindrical lens (no. 12 on figure 3.5) [68], (b) achromatic doublet (no. 10 on figure 3.5) [68], (c) scan lens (no. 7 on figure 3.5) [68], (d) XT2, collimated emission-port adapter (no. 4 on figure 3.5) [67].



### 3.3 Software Development

After recording the images by the EMCCD camera, they are sent to a computer for storage and processing. Data acquisition (DAQ) is performed through a custom software developed using LabVIEW (National Instruments, Austin, TX). A data acquisition device is used as an interface between the hardware and software for controlling the camera and galvanometer mirrors movement and recording or displaying all the necessary data. The software was developed to have a user friendly front panel. It consists of two panels.

The first panel gives the operator the opportunity for evaluating the system performance before using the main program during scanning, by applying the changes on the camera and galvo settings. On the camera settings, the region of interest (ROI) on the camera in both X and Y coordinates can be defined. Default values are 0 to 511 pixels, which covers the whole  $512 \times 512$  pixels of the camera. Exposure time (ms), gain, and binning also can be set by the operator. On the galvanometer settings, the position of X-Y galvo mirrors can be set by writing the desired voltage on them. With a scaling of 0.5 volts per degree of mechanical movement, which is the default value for our galvo system, min/max mechanical scan angle is  $-20^\circ$  to  $+20^\circ$  for the full  $-10V$  to  $+10V$  input. Based on the applied voltage the galvo driver sets each mirror position to the command input value.

The main panel displays the same settings on the previous panel but with some more options added. To acquire less noisy data-sets, the user can define the number of full scans and get the average of the measurements when processing the data. On the galvo settings, the number of images in each scan can be defined. This is actually the number of steps at each full scan that we collect during measurements. Since we are implementing a line-pattern laser scanning, only one galvo mirror (Y) is needed and the other one (X) has a fixed position at 0 degree, which is not shown here. The min/max voltage written on the galvo depends on the field of view we need to cover over the sample. Default values are  $-0.6V$  to  $+0.6V$ , which covers a  $3mm \times 3mm$  field of view. The display shows a live view of the sample while

scanning. The number of images captured, the total number of images and the total scan time (ms) are also shown at the top of this panel.

The EMCCD camera and galvo are synchronized by inner program signals, so that the camera captures the images every time the galvo is repositioned. At the end of the scanning process, we have the measurements based on the number of scans and number of steps defined at each scan. All raw images are loaded to MATLAB (The MathWorks Inc., Natick, MA) for post processing and image reconstruction. A set of preprocessing algorithms should be applied before image reconstruction to generate a cross-sectional or volumetric frame. This process involves reading the images, producing the raw data for the 7 source-detectors, background removal and finally reconstruction using a reconstruction algorithm and an appropriate method to model light propagation in the sample.

Next sections will cover the processing chain of data processing algorithms, along with the algorithm we used in this project for image reconstruction including the forward model, inverse problem and the model of light propagation.

### 3.4 Data Analysis

As previously mentioned, after transferring the data to the hard drive, a set of preprocessing and then image reconstruction algorithm had to be applied. This covers the process of how the recorded images from the top view were processed and turned into the cross-sectional or 3D volumetric images of fluorescence distribution in the tissue. Since the measurements contain the images of the sample from different positions relative to the laser focal point, the first step in processing the data is transforming the raw data.

Data collected from the CCD camera includes the information of all the 7 source-detectors in each image as the laser beam scans the tissue surface. For example, 200 steps or measurements is equal to 200 images (at 200 laser positions), while all the source-detectors' measurements are recorded in each image. First part of the process is to rendering 7 useful



images of raw data for each of the 7 SD separations based on the measurement geometry we covered earlier in section 3.1. An example of the raw data of a sample consisting a rectangular channel with the size of  $150 \times 25$  microns at the depth of 1.19mm filled with  $8\mu M$  FAD is shown in Figure 3.8.  $SD_1$  separation (i.e. first source-detector separation) is 0 and  $SD_7$  separation (i.e. last source-detector separation) is 1.2mm.

The raw data on its own, and even before attempting to apply any image reconstruction, gives us a great deal of information. It can be examined by eye to infer information about the shape and depth of structures within the tissue. The raw data of  $SD_1$ , where the source and detector are exactly on top of each other, has the most similar shape to the real channel and is equivalent to the confocal image of the sample's surface. As the SD separation increases, the more information from the depth is retrieved and a shadow of the channel appears. However, this data does not represent true depth of the scattering medium and is only a weighted sum of signals from the shallower and deeper parts of the tissue [35]. Looking at the raw data, under two conditions we have the strongest signals detected. When the laser source is on top of the channel and when the detector is on top of the channel. Under first condition only one channel appears since the source and detector are exactly on top of each other.

There is a fixed pattern overlaid on the images caused by the intrinsic fluorescence of the sample, back reflections from different parts of the system (fiber couplers, lenses, etc.) and noise pixel bias in the camera. Noise background can be improved by scanning the sample more than once and taking the average of the measurements. Back reflections can be removed by placing a polarizer in a plane perpendicular to the incident beam to block the light with the same polarization of the excitation light.

To reduce the intensity of autofluorescence light caused by the intrinsic fluorophores, we used the fact that most autofluorescence signals have broad excitation and emission spectrums while specific fluorescence probes, like GFP (Green Fluorescence Proteins), have a more narrow spectrum [70]. The sample was scanned using two wavelengths, blue (450nm)

and red (653nm), over the same FOV and using the same filter settings. The blue laser is able to excite both intrinsic fluorescence and GFP (or FAD in the phantom experiments), but the red laser is only able to excite the intrinsic fluorescence. Therefore, we have a constant background of intrinsic fluorescence in all 7 source-detectors, which can be subtracted from the raw data.

The subtraction suppresses noise, helping to improve the signal to noise ratio (SNR). Another step to improve the SNR is to set appropriate exposure-time depending on the source-detector separations and detected signals. For example, exposure-times were set between 5ms to 50ms for SD separations of  $200\mu\text{m}$  to  $1200\mu\text{m}$ . This specifically has a noticeable effect on the SNR for samples which have deeper fluorescence distributions.

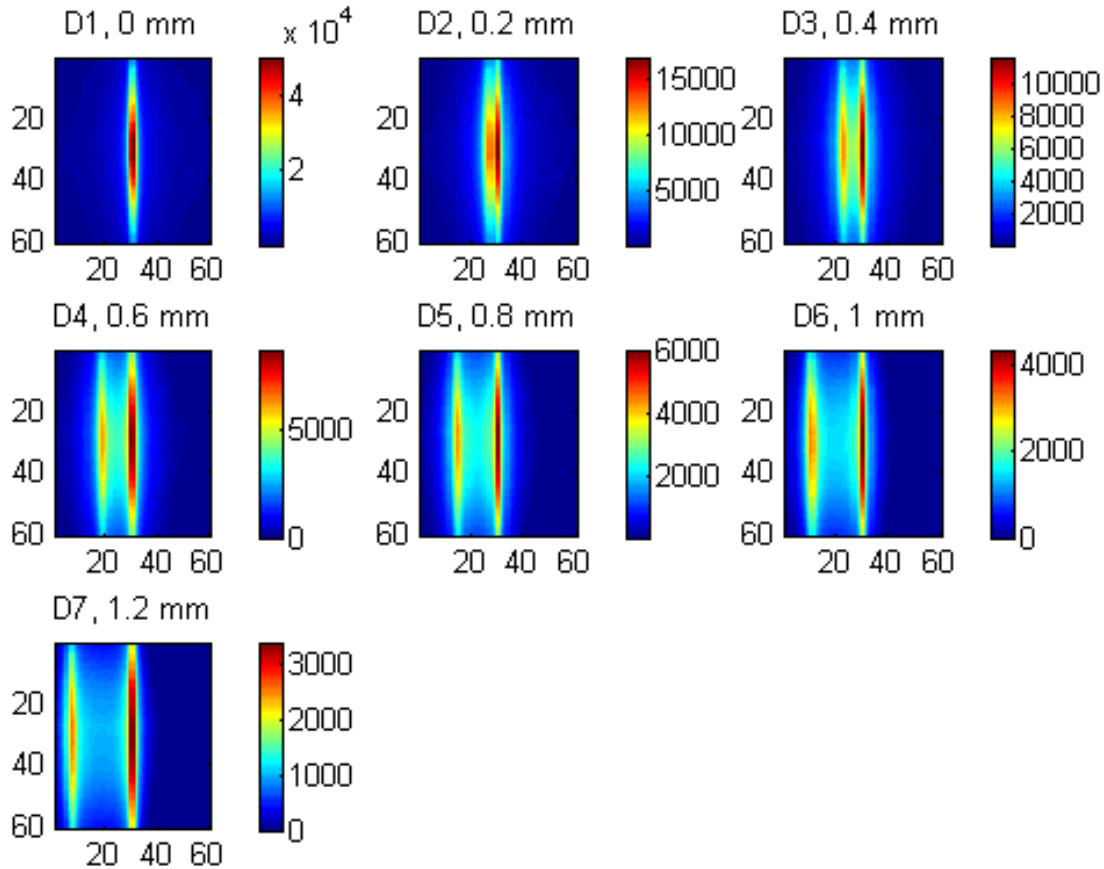


**Figure 3.8:** Raw data for 7 source-detector separations in FLOT measurements from a sample with an embedded rectangular channel,  $150 \times 25$  microns in size, located at the depth of 1.19mm, and filled with  $8\mu\text{M}$  FAD, after background correction (color bar shows the fluorescence intensity).

After background correction and exposure compensation, if needed, the cross-sectional images and the 3-D structure are reconstructed from the raw images. This involves using an image reconstruction algorithm along with an appropriate model of light propagation, which are covered in the next section.

### 3.5 Image Reconstruction

After raw data acquisition and analysis, next step is image reconstruction from the raw data. Tomographic image reconstruction, which creates cross-sectional images from a series of projection measurements, can be divided into two subproblems: developing a forward model to find the sensitivity distribution of each projection measurement, described by the light propagation models in the medium; and the inverse problem to reconstruct unknown parameters (hidden objects or underlying information) based on the experimental measurements and the forward model.

In LOT, the sensitivity of each measurement path is a function of the optical properties of the tissue being imaged. As a result, in order to determine the spatial sensitivity of each measurement, before image reconstruction is attempted, a model of photon transport in tissue is required to simulate the behavior of light scattering in tissue [25][72].

We covered three models of light propagation inside tissue (RTE, DA and MC) in section 1.3. As discussed, the RTE is difficult to solve numerically and exact solutions only exist for relatively simple cases. Therefore, the RTE is simplified by a set of approximations to reach the famous diffusion approximation (DA). However, DA cannot be employed since this model is not suitable for small source-detector separations similar to our FLOT configuration, where light cannot be assumed to be diffused.

Consequently, Monte Carlo simulation [30][32] is employed to simulate the sensitivity matrix of each source-detector pair. Simulated sensitivity matrices for four different source-detector separations (0 to 1.6mm) are shown in Figure 3.9. In our work, the Monte Carlo

code written by Steven Jacques is used [30]. MC simulation requires advanced knowledge of the refractive index, the reduced scattering coefficient  $\mu'_s$ , and the absorption coefficient  $\mu_a$  of the sample. Later in chapter 4, we will cover the double-integrated spheres optical setup that we used to measure the optical properties of our samples.

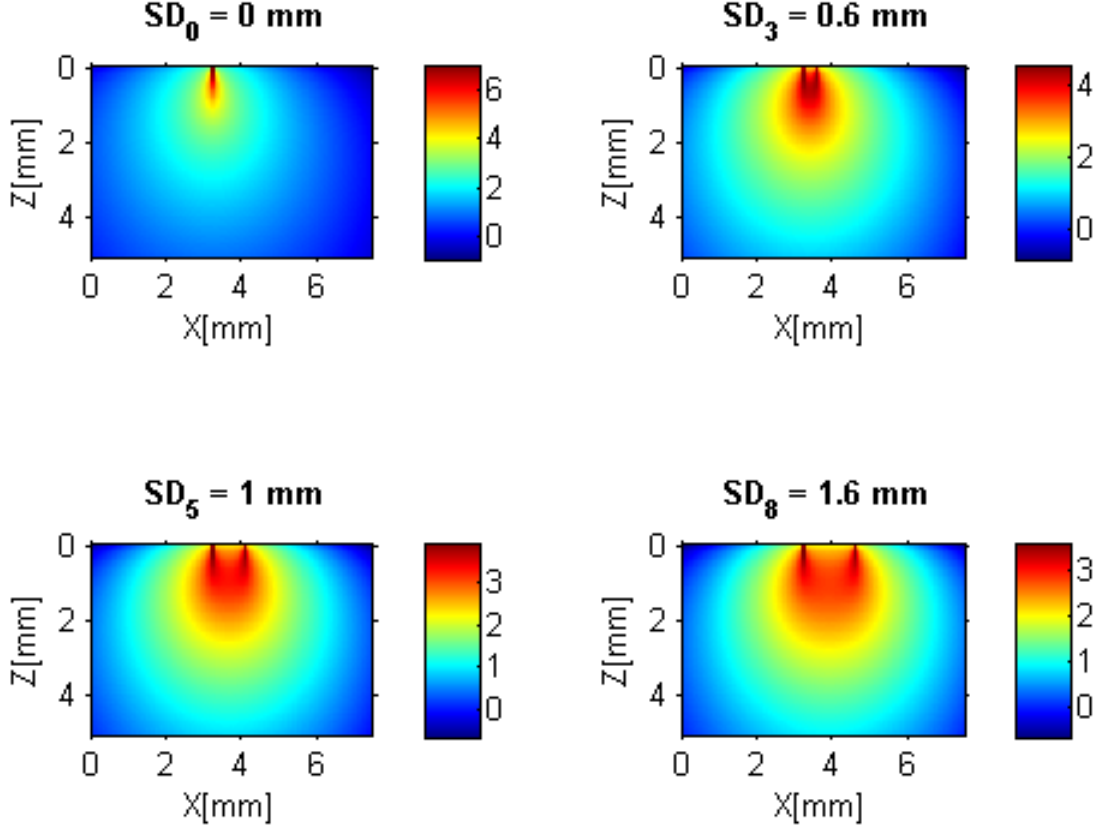


**Figure 3.9:** Monte Carlo simulation in a scattering medium for four different SD separations from 0 to 1.6 mm in logarithmic scale (color bar shows the fluorescence intensity).

By developing the forward model we can generate the sensitivity matrix  $W_{SD}(r)$  (also called the Jacobian or weight matrix), which relates the change in measurements  $\Delta M_{SD}$  for a source and detector position (SD) to the internal optical properties or in our case the change in the spatial distribution of the fluorophore concentration  $\Delta F(r)$  at the position  $r$ :

$$W_{SD}(r) = \frac{\Delta M_{SD}}{\Delta F(r)}, \quad (3.1)$$

$$\Delta M_{SD} = W_{SD}(r)\Delta F(r). \quad (3.2)$$

This equation can be reconfigured in the form of a set of linear equations, which leads to a discrete matrix representation of the linearized problem, by using  $m$  linear equations (number of measurements) with  $n$  variables (number of voxels):

$$\begin{pmatrix} M_1 \\ M_2 \\ \vdots \\ M_m \end{pmatrix} = \begin{pmatrix} W_{11} & W_{12} & \cdots & W_{1n} \\ W_{21} & W_{22} & \cdots & W_{2n} \\ \vdots & \vdots & \ddots & \vdots \\ W_{m1} & W_{m2} & \cdots & W_{mn} \end{pmatrix} \times \begin{pmatrix} F_1 \\ F_2 \\ \vdots \\ F_n \end{pmatrix}. \quad (3.3)$$

In this equation, matrix  $M$  is the experimental measurements, each row of  $W$  corresponds to a different source-detector pairing sensitivity matrix simulated by the Monte Carlo method, and  $F$  is the spatial distribution of the fluorophore concentration in each voxel. Then, the unknown parameters  $\Delta F(r)$  are obtained by inverting the weight matrix and solving the inverse problem:

$$\Delta F(r) = W^{-1}_{SD}(r)\Delta M_{SD}. \quad (3.4)$$

The inverse problem in multidimensional space, corresponding to light propagating in tissues, is generally under determined and ill-posed due to absorption and scattering in the medium and the limitations on the data acquisition [46]. In other words, the limited number of sources and detectors results in limited number of measurements less than the number of voxels to be reconstructed (unknown). In ill-posed problems, small perturbations of the data potentially leads to large fluctuations of the solution. As a result, finding a unique solution representing a true reconstruction of the object may not be possible.

Some useful results do exist; however, they required using different analytical and numerical algorithms. These techniques differ in the regularization method used for matrix in-

version, which is needed to suppress the influence of measurement noise and modeling errors [73]. The most popular techniques are singular value decomposition (SVD) [74], Tikhonov regularization [75], and the iterative techniques such as algebraic reconstruction technique (ART) [76], simultaneous iterative reconstruction technique (SIRT) [77] and simultaneous algebraic reconstruction technique (SART) [78].

Writing the forward problem in the form of  $Ax = b$ , a common way to regularize the solutions is by using the Tikhonov regularization method, since it has a closed form and is easy to implement. This method attempts to find a useful approximation to the solution ( $x$ ) by replacing the minimization problem ( $\|Ax - b\|$ ) by a penalized least-squares problem ( $\|Ax - b\|^2 + \lambda^2 \|x\|^2$ ), where  $\lambda$  is the regularization parameter. The drawback; however, is that it over-penalizes the pixels with near-zero coefficients, causing many pixels with unwanted small coefficients to be produced [79]. This results in a blur reconstructed image with poor spatial resolution, specially in our case, where many images are usually sparse, and most weight coefficients in matrix  $W$  are zero or close to zero.

Another approach to solve the inverse problem is by using iterative algorithms, which seek to determine the correct solution through multiple iteration steps. This results in a better reconstruction at the cost of higher computation time. In general, the procedure for algebraic reconstruction is starting with an initial guess for the solution, computing successive projections on the hyperplanes represented by rows of the linear system until eventually yielding the correct answer [77]. In terms of the convergence of the algorithms in ill-posed problems, where the number of measurements is less than the number of unknowns ( $m < n$ ), such as the one we are considering, infinite number of solutions are possible. But the iterative approach converges to a solution such that the difference between the initial guess and the solution we found is minimized.

In this work, we used the Simultaneous Algebraic Reconstruction Technique (SART) [78], which is well-documented, robust, and straightforward in its implementation. Using the non-negativity constraint and a regularization scheme (accomplished by limiting the number of

iterations) helps to stabilize the convergence of the ill-conditioned problem by SART. The implementation of SART in MATLAB (The MathWorks Inc., Natick, MA) is based on the code written by P. C. Hansen et al. [80]. For arbitrary initial vector  $x^0 \in \mathbb{R}^n$ , the algorithm for SART takes the following form:

$$x^{k+1} = x^k + \lambda_k V^{-1} A^T W^{-1} (b - Ax^k). \quad (3.5)$$

In this iterative equation,  $K$  is the iteration number,  $\lambda$  is the relaxation parameter,  $V$  is the diagonal matrix with row sums of  $A$  ( $V = \text{diag}(\|a_i\|_1)$ , where  $a_i$  is the  $i$ -th row of the matrix  $A$ ), and  $W$  is the diagonal matrix with column sums of  $A$  ( $W = \text{diag}(\|a_j\|_1)$ , where  $a_j$  is the  $j$ -th column of the matrix  $A$ ).

SART is a flexible and fast algebraic method. It allows incorporation of prior information, e.g., non-negativity or box constraints. Several methods are available for choosing the optimal relaxation parameter  $\lambda$ . Regularization is achieved by limiting the number of iterations  $K$ ; however, the choice for the number of iterations is a challenging topic for all algebraic methods, which using prior knowledge of the true solution can help to choose the best regularization (optimal truncation) [81].

Prior knowledge of the anatomy, physics or the physiology of the problem (for example in our case fluorophore localization information and internal structure of the tissue), can increase the accuracy of the forward model by representing the measurements more precisely, and also can be incorporated into the inverse problem, thereby improving the image reconstruction quality and accuracy [73][82].

### 3.6 Data Representation

The theory of LOT is developed for 3D reconstruction. However, 3D volumetric reconstruction of a region of tissue is computationally intensive and challenging, specially in under determined systems. One way to deal with this problem is by assuming that all

inhomogeneities are confined to a known horizontal slab, and performing two dimensional reconstructions [81]. Then, a 3D structure of the object can be obtained by stacking all 2D cross-sectional images together. This way, the number of unknowns reduces and, geometrically, the inverse problem scales down to estimation of fluorescence concentration in a two-dimensional slice.

Figure 3.10 shows an example of the 2D and 3D reconstruction of a sample with a rectangular channel ( $150 \times 25$  micron) at the depth of 0.8mm, filled with  $8\mu M$  FAD. Part (a) represents a local 2D ZX cross-section of the sample. Parts (b)(c)(d) are 3D reconstructions from stacking all the 2D cross-sectional images, from different views. The scan's FOV is  $3mm \times 3mm$ . 200 measurements with the size of  $512 \times 512$  pixels were used in each scan, but then down sampled to  $60 \times 60$  pixels in favor of reducing the computation time.

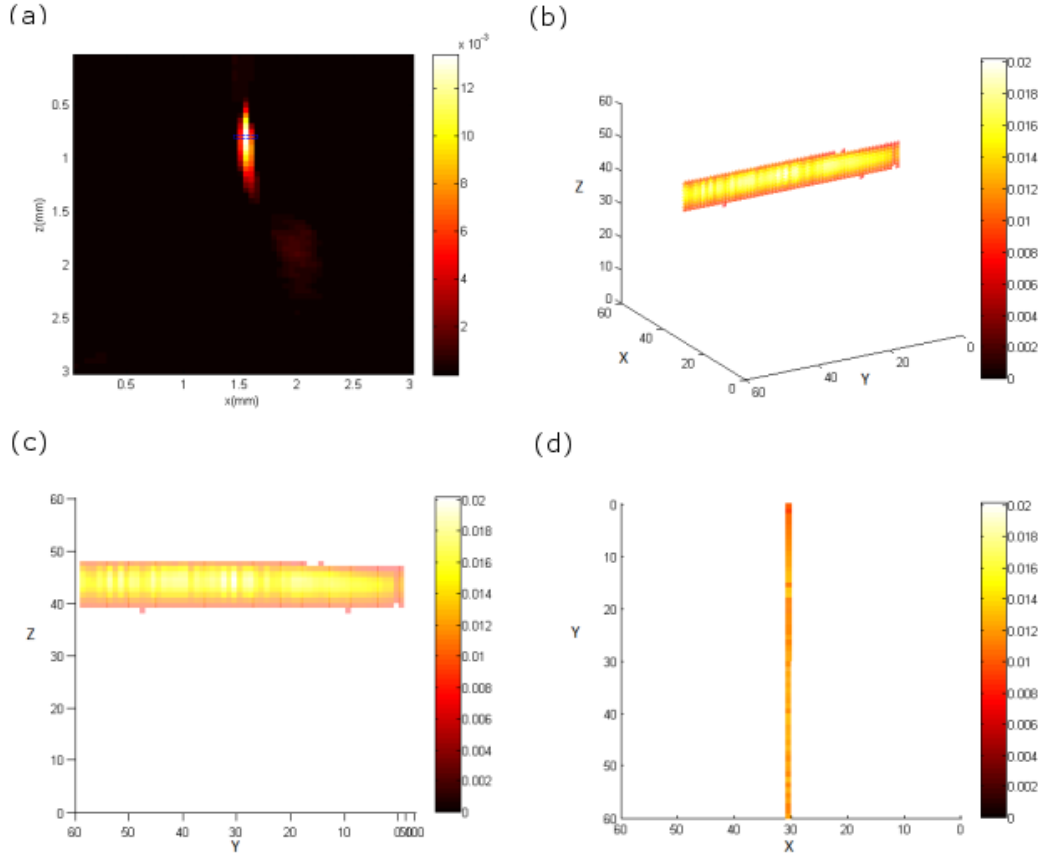


**Figure 3.10:** 2D and 3D reconstruction of a sample with a rectangular channel ( $150 \times 25$  microns) at the depth of 0.8 mm. (a) 2D ZX cross-section. (b) 3D volumetric reconstruction, XYZ view. (c) 3D volumetric reconstruction, YZ (side) view. (d) 3D volumetric reconstruction, XY (top) view.



## 3.7 Summary

This chapter described the design and implementation of our system for both hardware design and software development. Measurement geometry and demonstration of data acquisition and raw data analysis for a less noisy data-set and reducing the intrinsic fluorescence and back reflections have been presented. Finally, image reconstruction, including the forward model (light propagation in tissue) and inverse problem (SART algorithm), have been covered. In the next chapter, results of this study will be shown which demonstrate the ability of our system in detecting fluorescence distributions in superficial regions of tissue.

---

## Chapter 4

### Experimental Results and Data Analysis

The performance of our FLOT system was demonstrated by using three test models with increasing levels of difficulty. First, a series of simulations were carried to demonstrate the performance of the reconstruction algorithm using MC simulations for the defined measurement geometry. In these simulations, optical properties were well defined and the level of noise was under control. The second model was for the measurements we acquired using our silicone-based phantoms. In this step effects of the experimental noise and systematic errors were included, yet we were able to achieve a good estimation of the optical properties of phantoms using double integrating sphere system. The final set of experiments were performed in lab rats with fluorescent injections in the brain, bringing the full complexity of the fluorescence tomography experiments.

#### 4.1 Simulation Studies

In our simulations, we created a mathematical model of the system to explore the behavior of the reconstruction model. The objective of our simulations was to understand the effect of changing parameters of the algorithm on the final results, as well as testing the ability of the system on establishing the existence of fluorescence object in a tissue model. Figures 4.1 and 4.2 show the results in both 2D cross-sectional and 3D volumetric representations. The Monte Carlo simulation were conducted on a medium of  $100 \times 250 \times 250$  voxels with optical properties close to brain tissue, but then down sampled to  $20 \times 50 \times 50$  voxels in favor of reducing the computation time. The tissue was defined with  $15 \times 10 \times 10$  voxels ( $4 \times 10 \times 10 mm^3$ ) with a fluorescence object of size  $2 \times 2 \times 2$  voxels ( $0.5 \times 1 \times 1 mm^3$ ) at

the depth of 2mm. SART algorithm was used with 5000 iterations. Comparing the real object with the reconstructed image, it is evident that the reconstruction shows a rough but reasonable image of the object's depth and distribution.

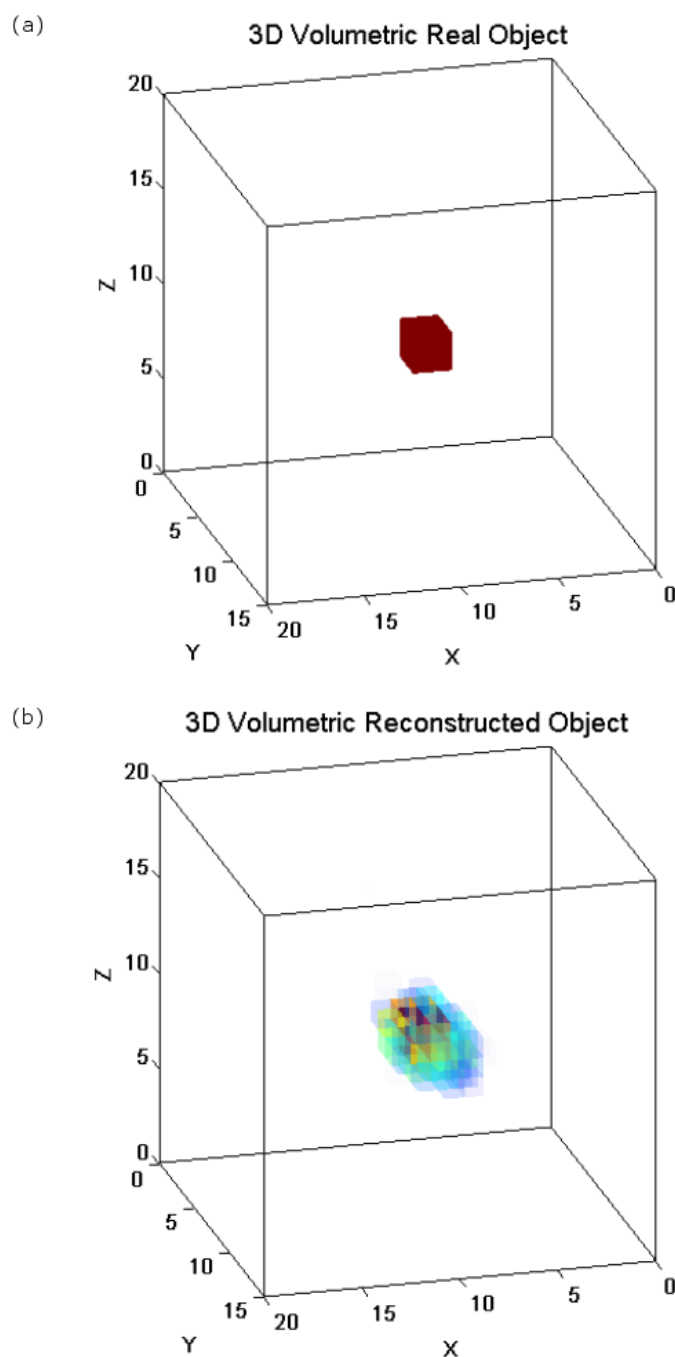


**Figure 4.1:** Simulation of 3D reconstruction of a square object at the depth of 2 mm. (a) 3D volumetric image of the real object in XYZ view. (b) 3D volumetric image of the reconstructed object in XYZ view.

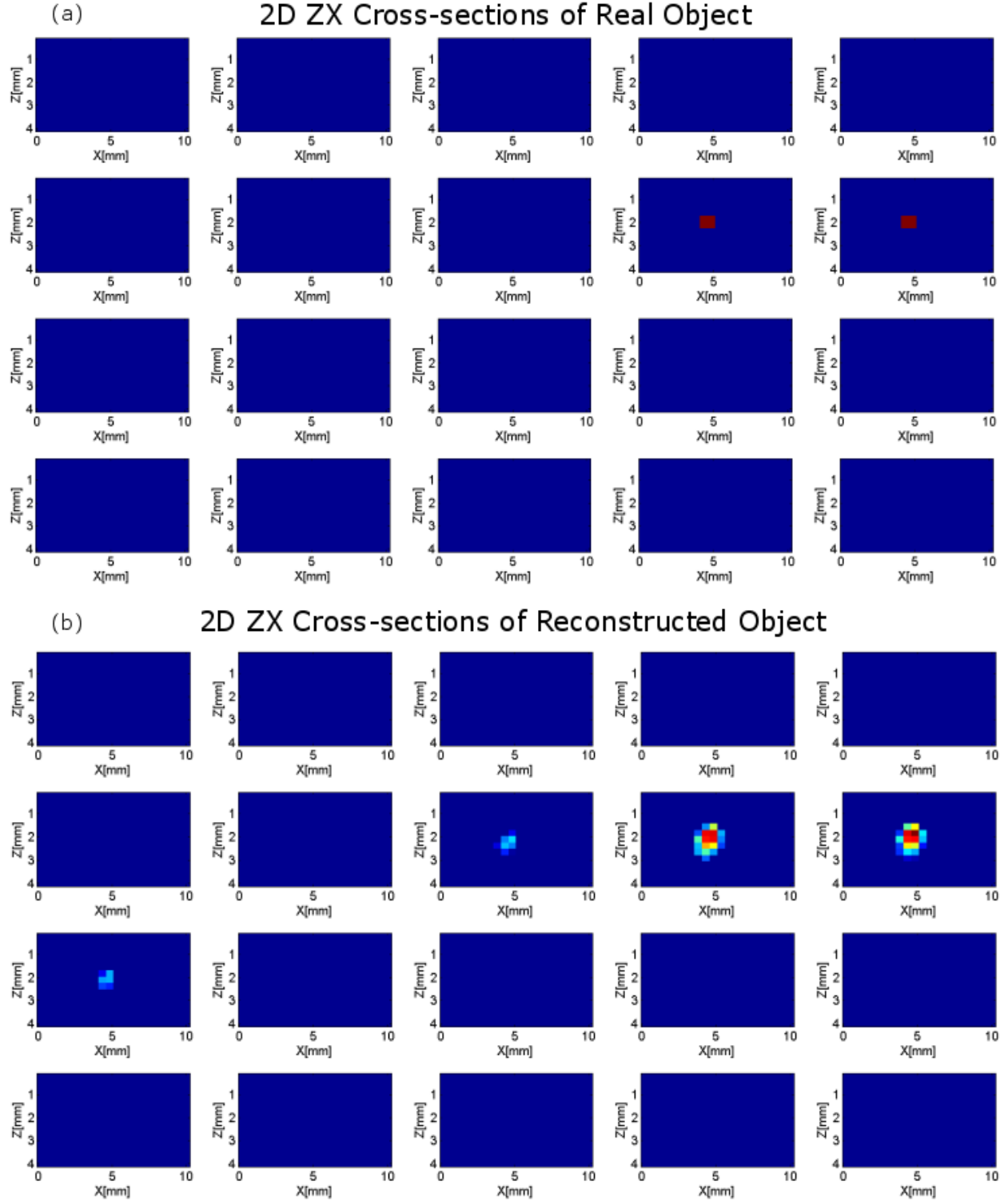


**Figure 4.2:** Simulation of 2D reconstruction of a square object at the depth of 2 mm. (a) 2D ZX cross-sections of the real object. (b) 2D ZX cross-sections of the reconstructed object.

## 4.2 Phantom Studies

Tissue-simulating optical phantoms are commonly used to mimic light distributions in living tissue to calibrate or evaluate the performance of optical instruments under experimental conditions [83][84]. We are interested in developing optical phantoms suitable for FLOT imaging applications. We used these phantoms to determine fluorescence quantum yields in the visible spectrum, with predefined optical properties at two wavelengths, 450nm and 530nm. These phantoms are made from four components: a base material and its curing agent, scattering agent, absorbing agent, and fluorophores.

Several types of phantoms such as homogenized milk, suspensions of oils/fats in an aqueous solution, or suspensions of Intralipid and India ink in agarose, were used to simulate the optical properties of biologic tissues. Using liquid phantoms has the difficulty of creating inhomogeneities or fine structures like blood vessels. Identifying a tube or container to encapsulate the fluorescence material such that the difference in refractive indices does not create reflections is another issue. To tackle these problems, we decided to use silicone-based microfluidic phantoms, which are robust, cost effective, easy to transport and use, and have a long shelf life. Another main advantage is their flexibility in design, so that we do not need to use an extra structure like a tube or container, instead we can make the channel structures inside the phantoms to inject the fluorescence solutions.

The phantoms were fabricated by using pure polydimethylsiloxane (PDMS) and its associated curing agent (Sylgard 184 silicone elastomer kit, Ellsworth Adhesives, Germantown, WI), at room temperature. To introduce scattering and absorption, titanium dioxide ( $TiO_2$ , Sigma Aldrich, St. Louis, MO) and India ink (Chartpak Inc., Leeds, MA) were chosen respectively. The method of preparation of the samples is described in the next section. The absorption and scattering properties of the created phantom is a primary design factor. Inverse Adding-Doubling (IAD) method was used to find the scattering and absorption of a thin slab of the material using total reflection and total transmission measurements

reference. This method is described in more details in section 4.2.2.

### 4.2.1 Design and Fabrication method of tissue phantoms

Our phantom is developed by mixing the correct portions of the base material, scattering and absorbing media, so that the resulting suspension has the optical properties close to the simulated tissue. According to [85], typical optical properties of gray matter are around  $\mu_a = 1mm^{-1}$ ,  $\mu_s = 30mm^{-1}$  and  $g = 0.9$ , for 450nm wavelength. Our chosen scattering medium,  $TiO_2$ , and the absorption agent, India Ink, have been employed in other phantom investigations, but have not been completely characterized in PDMS base phantom at 450nm. However, referring to the available literatures [83][86] for other wavelengths, and the fact that tissue absorption and scattering is higher for shorter wavelengths, we can start with an initial weight and change it if needed after measuring the real optical properties.

The first step in PDMS molding is mold design. Such molds come in a variety of shapes and sizes. The molds we used had rectangular channels with different widths and heights. The surface conditioning of the mold is an important factor in preventing PDMS from sticking (Figure 4.2(a)). Different ratios of the PDMS base versus the curing agent help to produce different hardnesses. We used the traditional 10:1 ratio which results in a solid yet flexible structure. We combined 12 grams of PDMS and 1.2 grams of the provided curing agent to make a 13.2 grams phantom. Scattering is achieved by adding  $TiO_2$  powder to the mixture.  $TiO_2$  is a highly effective scatterer due to its high index of refraction while has negligible absorption. Absorber is added in the form of India ink.

The whole procedure [83][87] of fabricating the phantoms is shown in Figures 4.3 and 4.4. To begin, 1.2g curing agent is poured in a plastic beaker.  $TiO_2$  is measured by weight (24.8mg) and added to the curing agent (Figure 4.3(b)). This is manually mixed for about 10 minutes. The solution should be stirred several times during this period to prevent the  $TiO_2$  from precipitating. We also used the ultrasonic bath to make sure that  $TiO_2$  is completely mixed with the curing agent. During this period, the bulk PDMS (12g) and India ink (10mg)

is combined (Figure 4.3(c)). In the next step we mixed these two solutions again for about 10 minutes manually and then pour it into the mold (Figure 4.3(d)). For removing any entrapped bubbles, we place the mixture with a cover on top into a vacuum chamber for at least 30 minutes (Figure 4.3(e)). After degassing, the molds were set onto a level surface in the 80 degree Celsius heated chamber (oven) for at least 3-4hrs and then we let them rest for about 24hrs (Figure 4.3(f)). Then the sample could be removed from the molds and cut out.

After demolding and cutting the phantom (Figure 4.4(g)), the next step is to pin the holes for the inputs/outputs of the channels using a microscope and special drillers with desired tip size. We chose 0.5 mm and 0.75 mm pin size (Figure 4.4(h)). The same procedure was done to make a base using the same materials and ratio for covering the channels. This way, we made a uniform phantom without using a piece of glass on top of the channels, which causes the reflection problem. These two pieces can be bonded together using the oxygen plasma surface activation (Figure 4.4(i)). PDMS is hydrophobic, with a low energy and non-reactive surface. Therefore, it is difficult to bond it with other surfaces. By exposing PDMS layers to oxygen plasma, its surface becomes hydrophilic and more reactive. This results in each sheet to be stacked on another easily without the use of any intermediary contact gels or air gaps [83]. Contact should be made quickly after plasma exposure since the PDMS surface undergoes reconstitution to its hydrophobic and non-reactive state within hours. The final rectangular-shaped phantoms are shown in Figure 4.4(j).

The thickness of each phantom can be measured directly by calipers or more precisely under the microscope. Taking measurements at multiple locations of each sheet can give a gross estimation of possible thickness variation (figure 4.4(k)). In our lab, we also have access to an OCT (Optical Coherence Tomography) scanner. With this technology, we were able to determine the exact phantom thickness. For fluorescent imaging we can inject different concentrations of FAD into the channels using a syringe pump (Genie Plus, Kent Scientific Corporation, Torrington, CT) (Figure 4.4(l)).

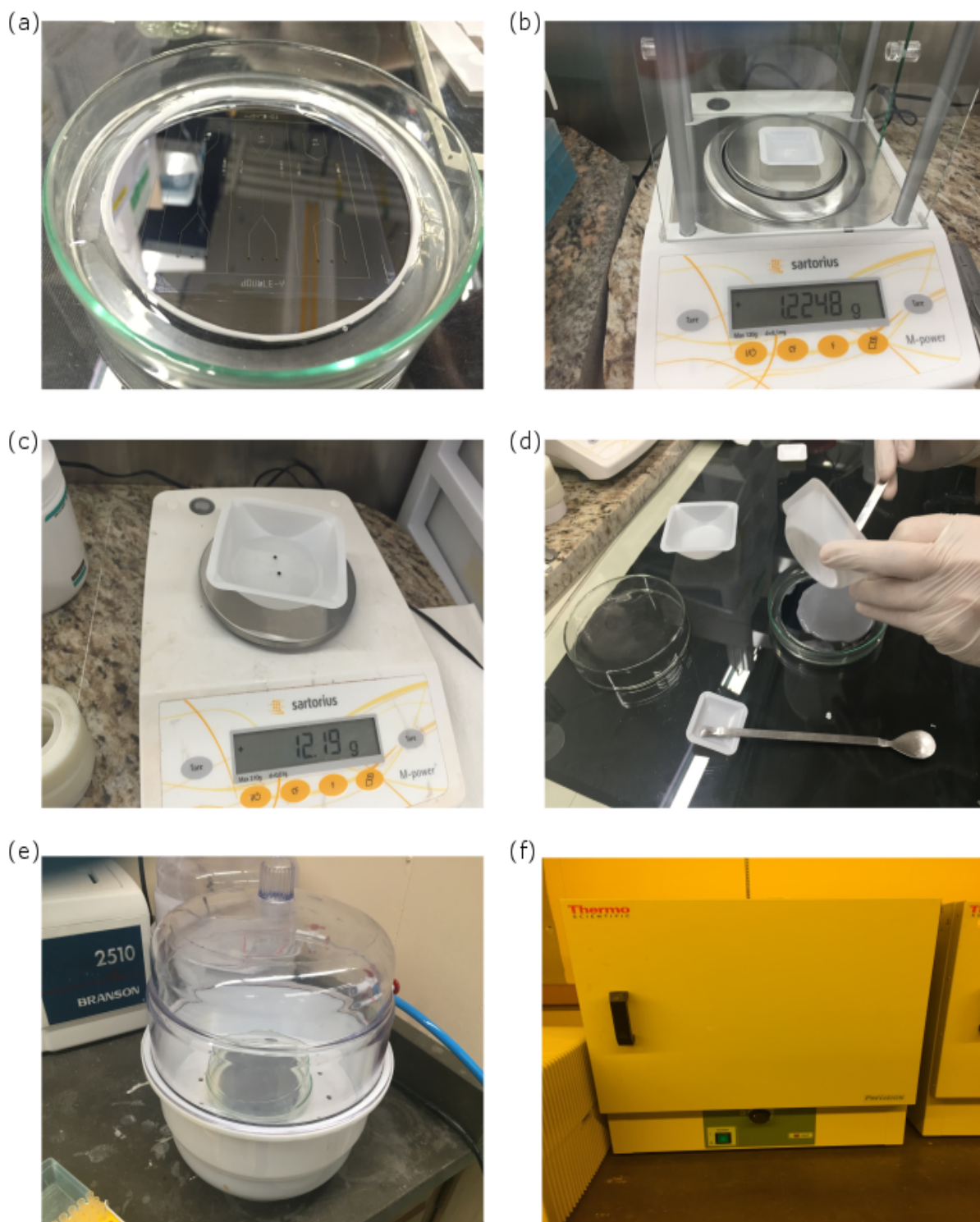


**Figure 4.3:** Phantom fabrication process 1. (a) Plain mold, (b) weighing curing agent and  $TiO_2$ , (c) weighing PDMS base and India ink, (d) pouring the mixture into the mold, (e) vacuum degassing, (f) oven baking.



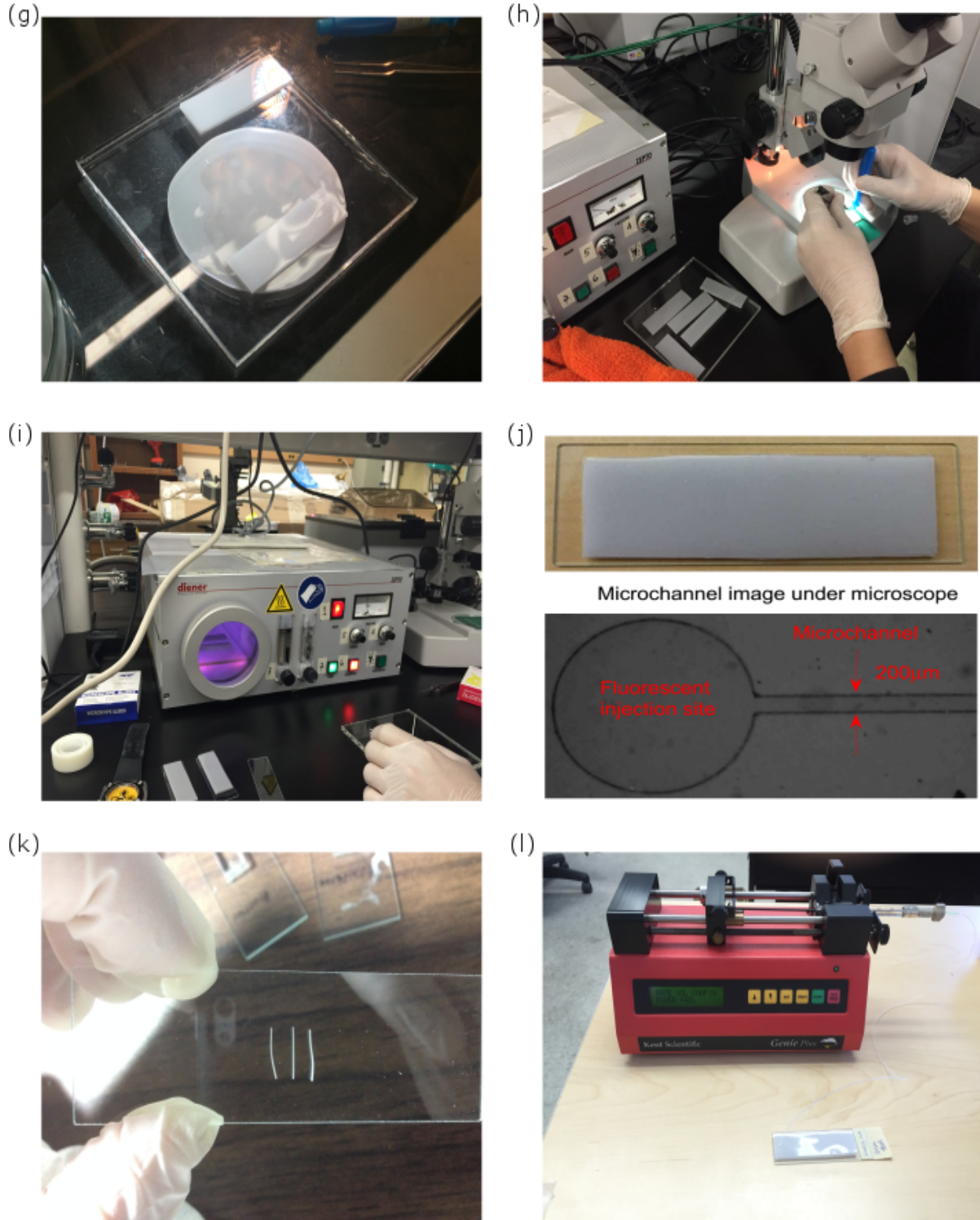


**Figure 4.4:** Phantom fabrication process 2. (g) Demolding and cutting the phantom, (h) pinning the input/output holes, (i) oxygen plasma surface activation, (j) final phantom and its image under microscope, (k) thickness measurements, (l) FAD injection using syringe pump.

## 4.2.2 Measuring the Optical Properties of Phantoms

A method is needed to determine the optical properties of phantoms (absorption and scattering coefficients and the anisotropy factor). These parameters were calculated based on the Inverse Adding-Doubling (IAD) method, by measuring the diffuse reflectance and transmittance using two integrating spheres optical setup [88]. The schematic and a picture of the optical setup is shown in Figure 4.5. This includes two integrating spheres (one two-port, 6-in. CVI Melles Griot BPS integrating sphere with 1.5-in. sample port diameter, and one four-port, 6-in. Spectrafect Integrating Sphere, with 1-in. sample port diameter, Newport Corporation, Irvine, CA), a collimated laser beam (450nm single mode pigtailed laser diode, Thorlabs Inc., Newton, NJ), a photodetector (PDA36A, Si switchable gain detector, Thorlabs Inc., Newton, NJ) mounted on the top sphere, and a second photodetector (APD110A2/M, avalanche photodetector, Thorlabs Inc., Newton, NJ) installed on the bottom sphere.

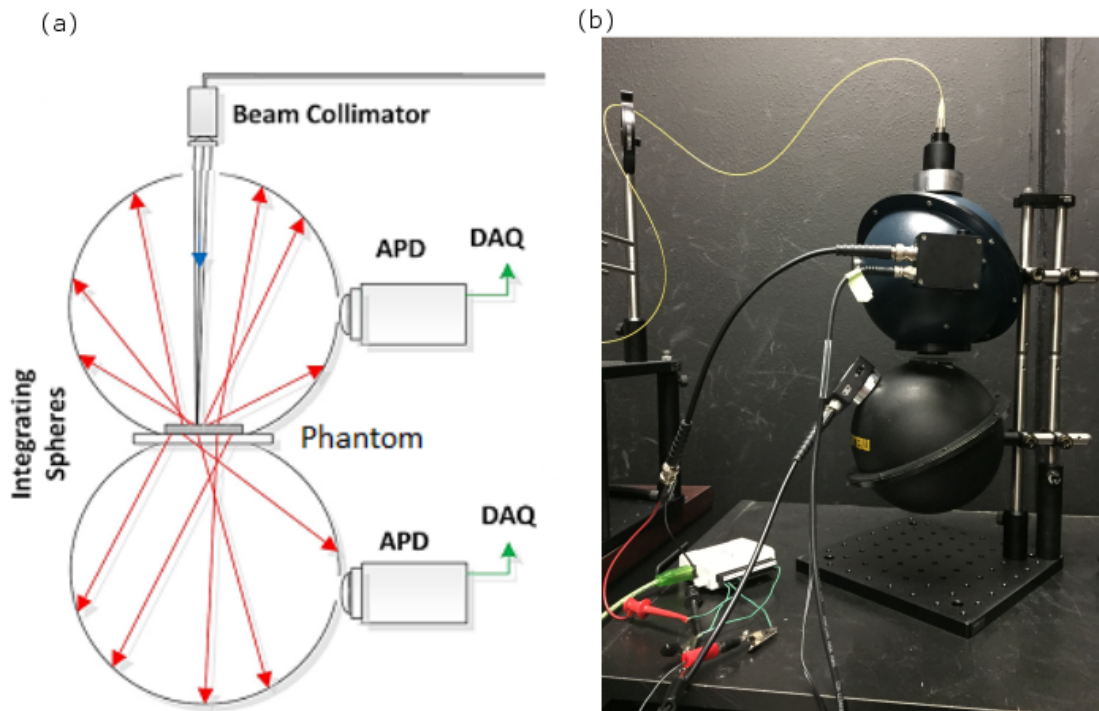


**Figure 4.5:** Double Integrating Sphere setup used to measure the diffuse reflected and transmitted light. (a) Schematic (taken and modified from [88]), (b) experimental setup.

After preparing the PDMS sample, it was placed between two integrating spheres. Using a laser source, we launched 450nm beam to the entrance port of the top integrating sphere which passes through to the bottom sphere. About  $90^\circ$  from the entrance ports, photodetectors are mounted on the detector ports. Different measurements are needed with samples as total reflector and total absorber to calibrate the system and measure the diffuse reflectance and diffuse transmittance. The diffuse reflected light intensity,  $R(r_s^{direct}, r_s)$ , was measured using the photodetector mounted on the top sphere, and diffuse transmitted light intensity,  $T(t_s^{direct}, r_s)$ , was measured by the second photodetector installed on the bottom sphere at the presence of the sample. The total reflectance,  $R(r_{std}, r_{std})$ , is measured with a total reflector from top detector, where  $r_{std}$  is the wall reflectance coefficient of the integrating sphere. Calibration parameters were also measured which include the  $R(0, 0)$  at the presence of a total absorber,  $T(0, 0)$  and  $T_{dark}$  where spheres are close to each other without anything in between, with the laser source be on and off respectively [88].

Once the dataset was prepared, these measurements were fed to the IAD code to extract the optical properties of the sample. This method is an iterative algorithm which starts with some random values assigned to the optical properties, and then, in each iteration, the algorithm solves the radiative transport equation to calculate the transmission and reflection of the sample and compares these results with the experimental data. The iterations continue until the calculated values of the reflection and transmission match the measured ones and the error is minimized. Some experimental results are shown below. The phantom we used is made of PDMS, TiO<sub>2</sub>, and India ink with the amount detailed in section 4.2.1.

#### **Dataset (measurements):**

Diffuse reflected light intensity  $R(r_s^{direct}, r_s)$ , with sample, top photodetector = 0.6832

Diffuse transmitted light intensity  $T(t_s^{direct}, r_s)$ , with sample, bottom photodetector = 1.4853

Total reflectance  $R(r_{std}, r_{std})$ , with a total reflector, top photodetector = 2.9120

Calibration parameter  $R(0, 0)$ , with a total absorber, top photodetector = 0.0735

Calibration parameter  $T(0, 0)$ , no sample, laser on, bottom photodetector = 1.5914

Calibration parameter  $T_{dark}$ , no sample, laser off, bottom photodetector = 1.3944

**Calculated optical properties:**

Absorption coefficient:  $\mu_a = 0.1552mm^{-1}$

Reduces scattering coefficient:  $\mu'_s = 0.9938mm^{-1}$

### 4.2.3 Measuring the Phantom Thickness

In order to confirm the reconstruction results with real channel depth, we tried two different methods. First, using a microscope and a thin cut of the top layer of the sample, second, by scanning the sample with an OCT system [71]. An example of the results for a sample with channel size of  $100 \times 500\mu m$  at the depth of 0.8mm, is shown in Figure 4.6. In general, scanning the sample with the OCT is more reliable and precise. With the microscope, we can only have a rough estimation of the depth as we are not able to cut through all parts of the sample to take the measurements. In contrast, with the OCT, we are able to scan any desired part of the sample with no limitation. In addition, the OCT can provide complimentary data regarding the channel width and height.

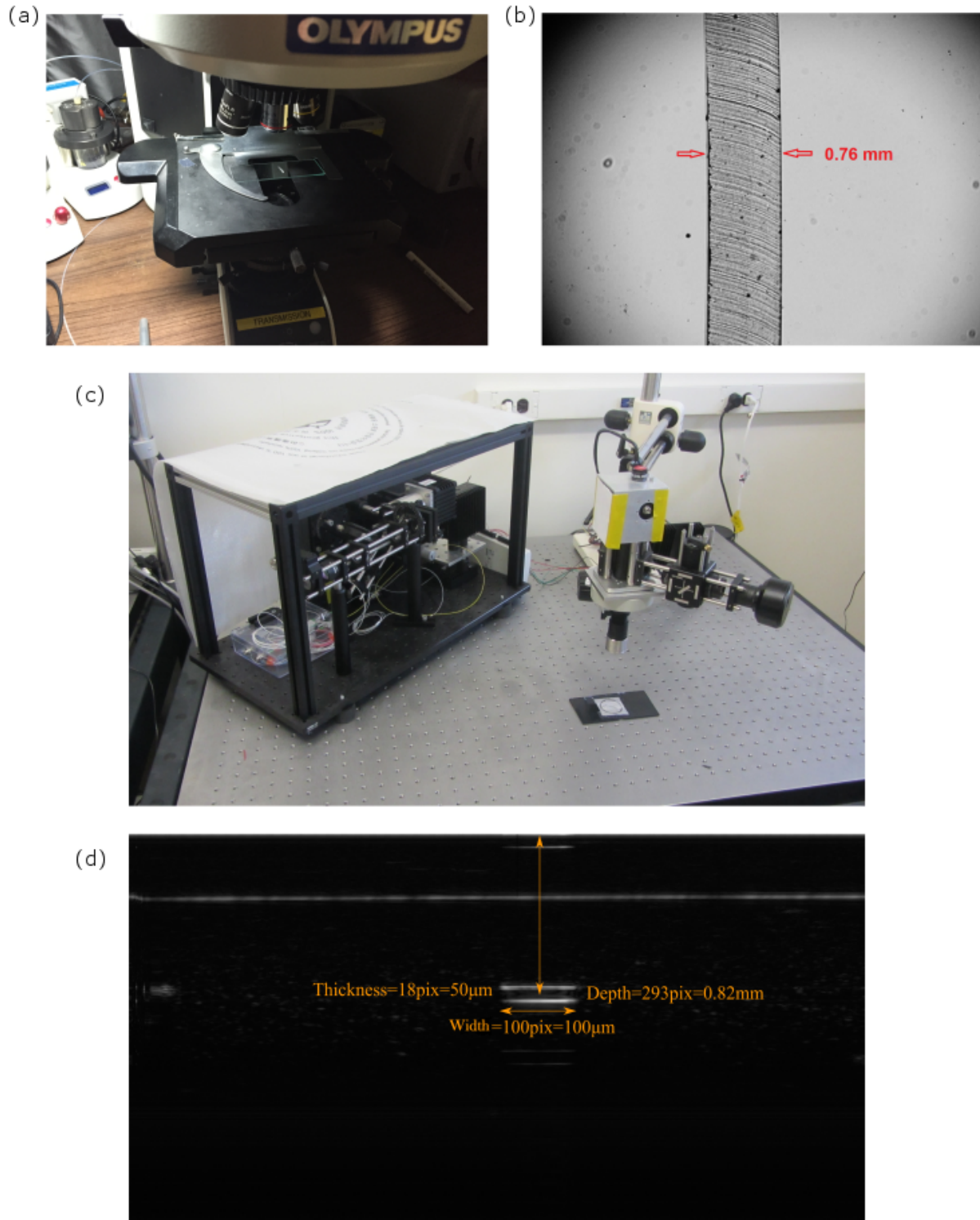


**Figure 4.6:** Measuring the depth of a phantom with the channel size of  $100 \times 50 \mu m$ . (a) and (b) Measuring the depth under the microscope, (c) and (d) measuring the depth using the OCT.



#### 4.2.4 Phantom Experimental Results

A picture of the setup used for scanning the phantom is shown in Figure 4.7. The position of the incident light can be specified by the user with the convention that illumination line is along the Y axis. Therefore, illumination direction lying in XZ plane and the acquired measurements are series of YX images. The results of the Monte Carlo simulations easily exceeded the capacity of our computer; therefore, we reduced the grid size to  $3 \times 3 \times 3mm^3$  ( $60 \times 60 \times 60$  voxels with the voxel size of  $50\mu m$ ) for all the tests we conducted in this project. The reconstruction typically needed 3000 SART iterations to obtain a reasonable result.

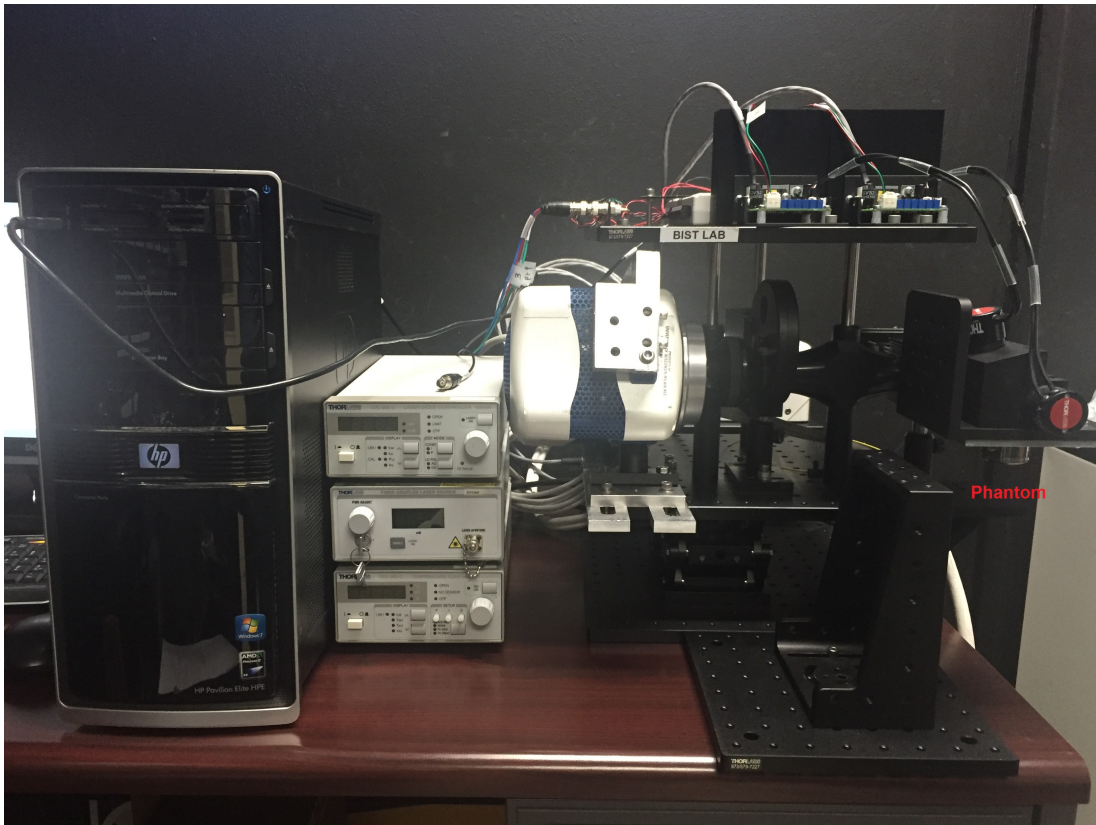


**Figure 4.7:** Optical setup for scanning phantoms.

Figures 4.8, 4.9 and 4.10 show some experimental results for three samples with a rectangular channel at depths of 0.82mm, 1.18mm and 1.64mm, respectively. Obviously, as we move further in depth, the raw data and reconstructions get noisier.

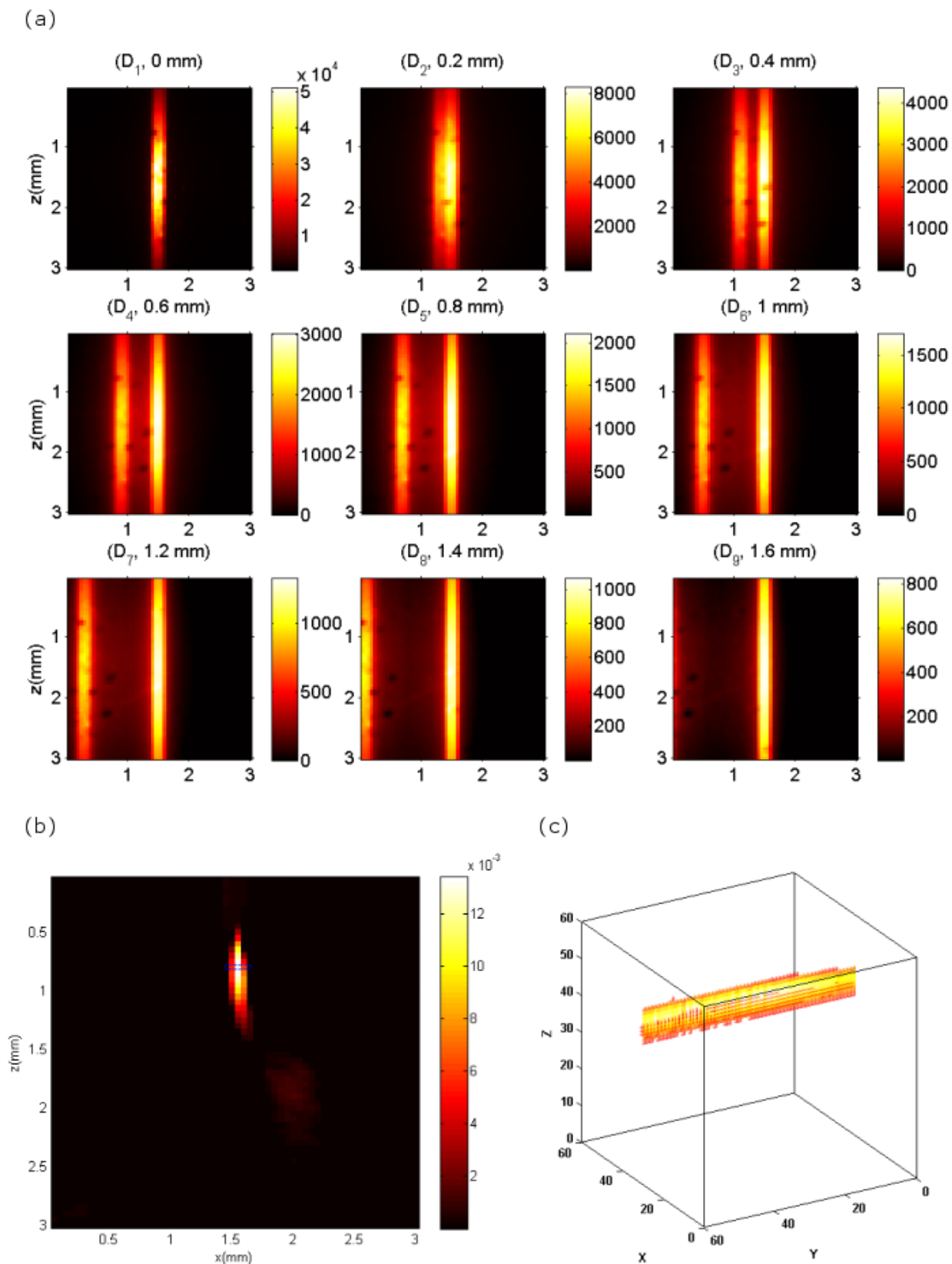


**Figure 4.8:** A phantom with a rectangular channel ( $200 \times 25$  microns) embedded at the depth of 0.82mm. Images were reconstructed by SART algorithm after 1600 iterations, (a) raw data (color bar shows the fluorescence intensity), (b) 2D  $\times$  cross-section of reconstructed channel (cross-section no. 30), (c) 3D volumetric of reconstructed channel, XYZ view.

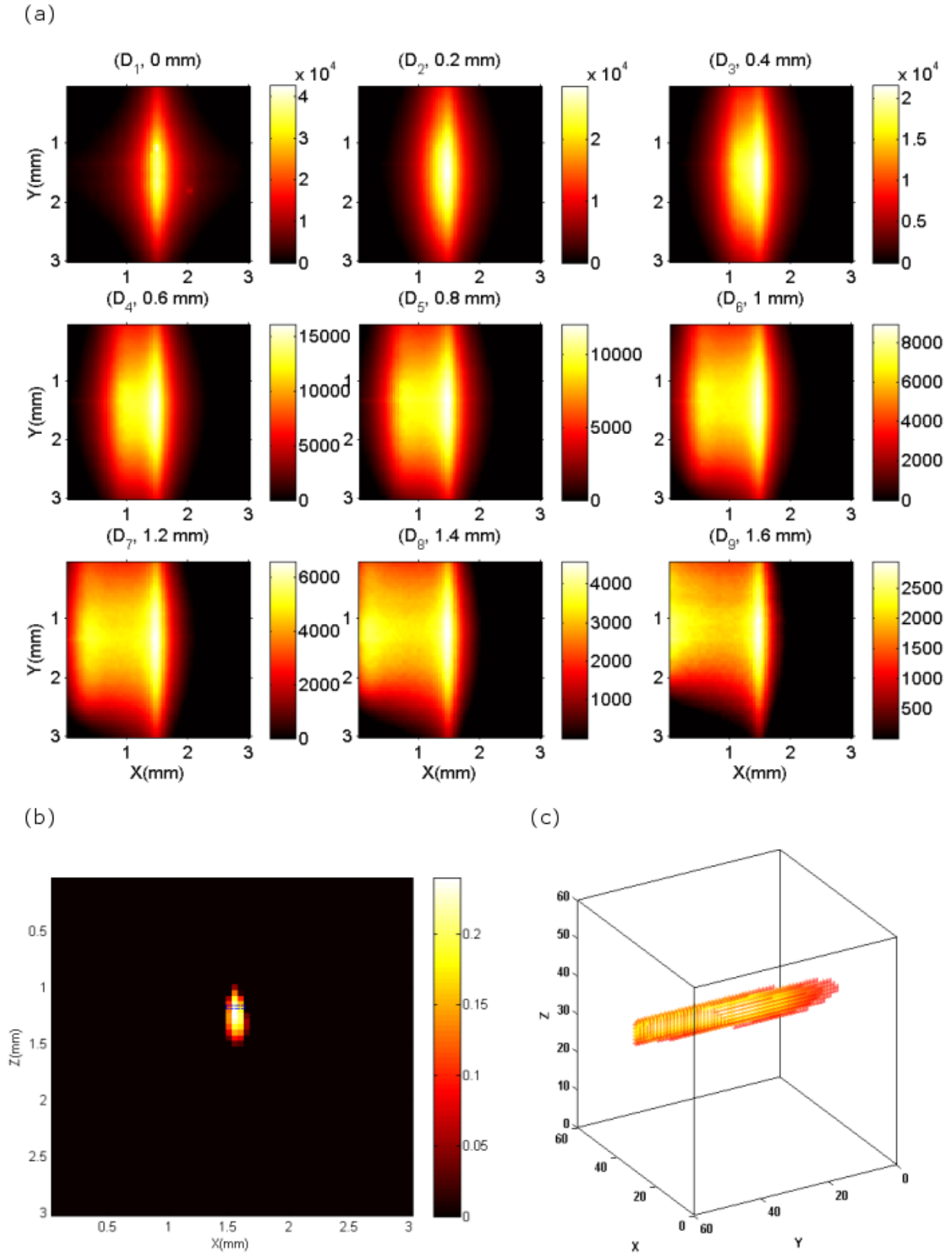


**Figure 4.9:** A phantom with a rectangular channel ( $150 \times 25$  microns) embedded at the depth of 1.18mm. Images were reconstructed by SART algorithm after 4000 iterations, (a) raw data (color bar shows the fluorescence intensity), (b) 2D  $XZ$  cross-section of reconstructed channel (cross-section no. 30), (c) 3D volumetric of reconstructed channel, XYZ view.



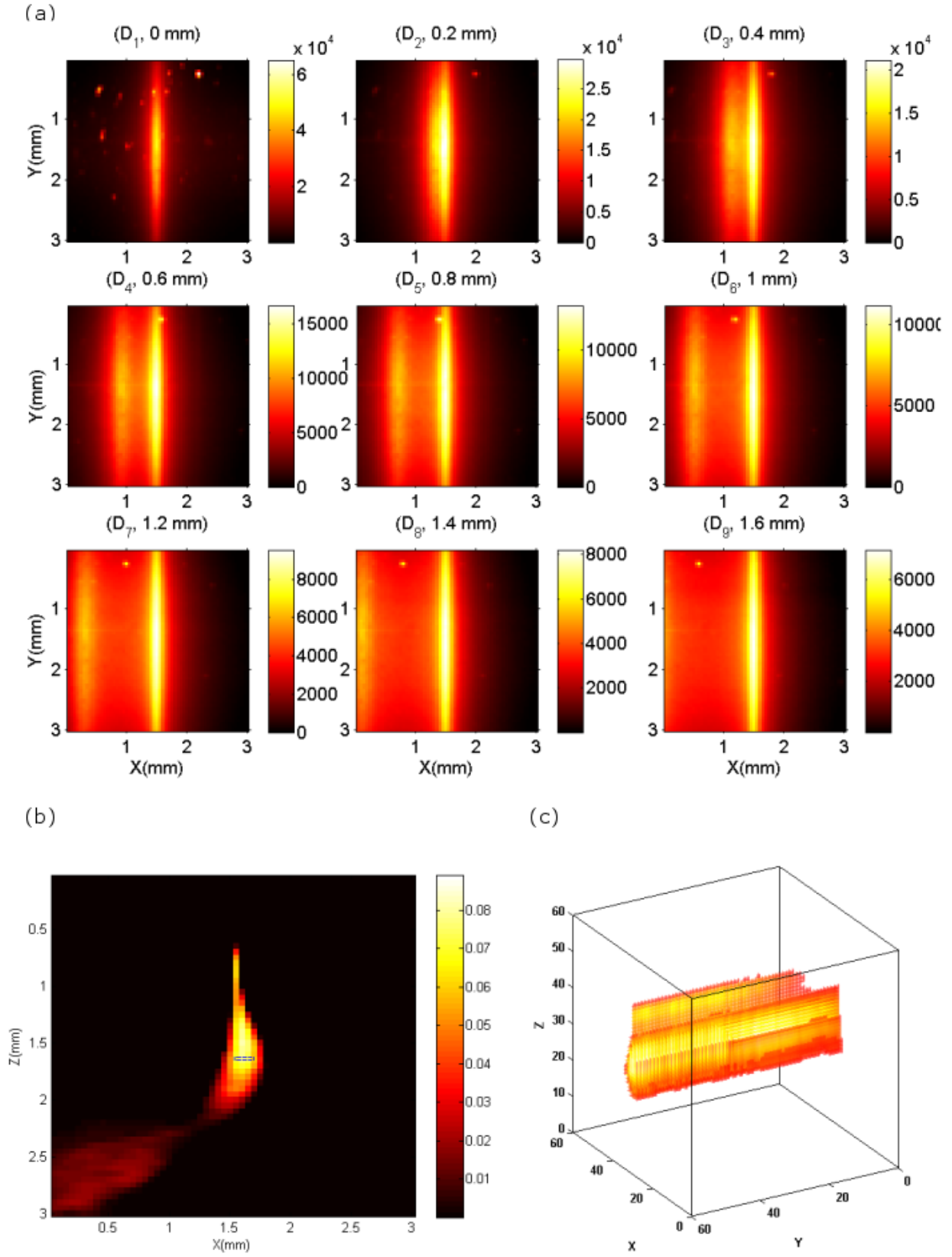


**Figure 4.10:** A phantom with a rectangular channel ( $150 \times 25$  microns) embedded at the depth of 1.18mm. Images were reconstructed by SART algorithm after 2000 iterations, (a) raw data (color bar shows the fluorescence intensity), (b) 2D  $Z$ - $X$  cross-section of reconstructed channel (cross-section no. 30), (c) 3D volumetric of reconstructed channel, XYZ view.

As mentioned before, to confirm the real depth with our reconstruction results, we scanned our phantoms with an OCT system. Our results illustrate a good match between these two techniques.

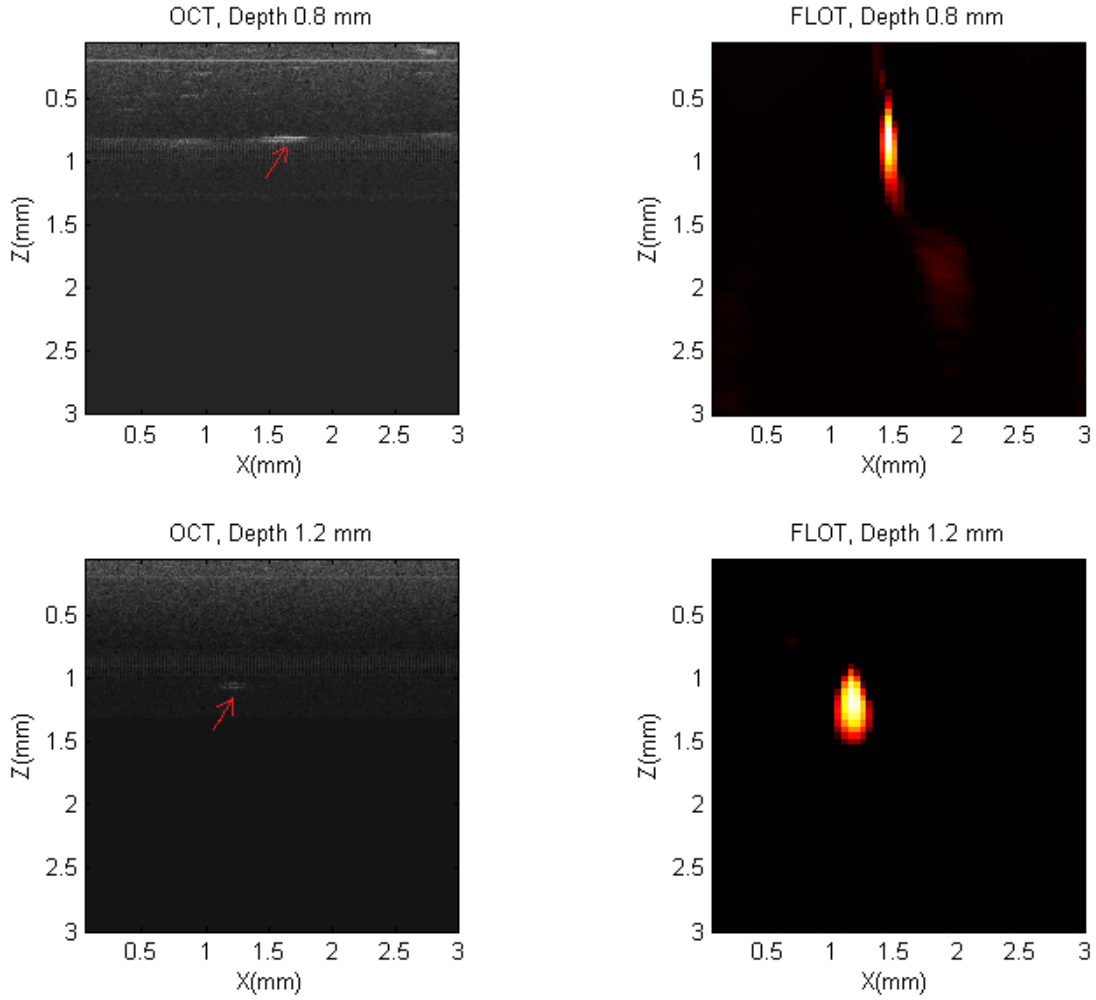


**Figure 4.11:** A comparison between the results of the OCT and FLOT in finding the depth of channels.

### 4.3 In-vivo Studies

In addition to computer simulations and phantom experiments, in-vivo experiments were also performed on rat brains, to test our device and the developed reconstruction methods under realistic experimental condition. The geometry of source-detectors, and all of the con-

ventions were the same as the ones used for the phantom studies. Monte Carlo simulation were adapted similar to the phantom experiments; nevertheless, we used the optical properties of the gray matter,  $\mu_a = 1\text{mm}^{-1}$ ,  $\mu_s = 30\text{mm}^{-1}$ , according to [85] and [90]. The FLOT system next to a surgery station for an animal experiment is displayed in Figure 4.12. The FLOT scanner head is positioned on the experiment table, right above the animal.

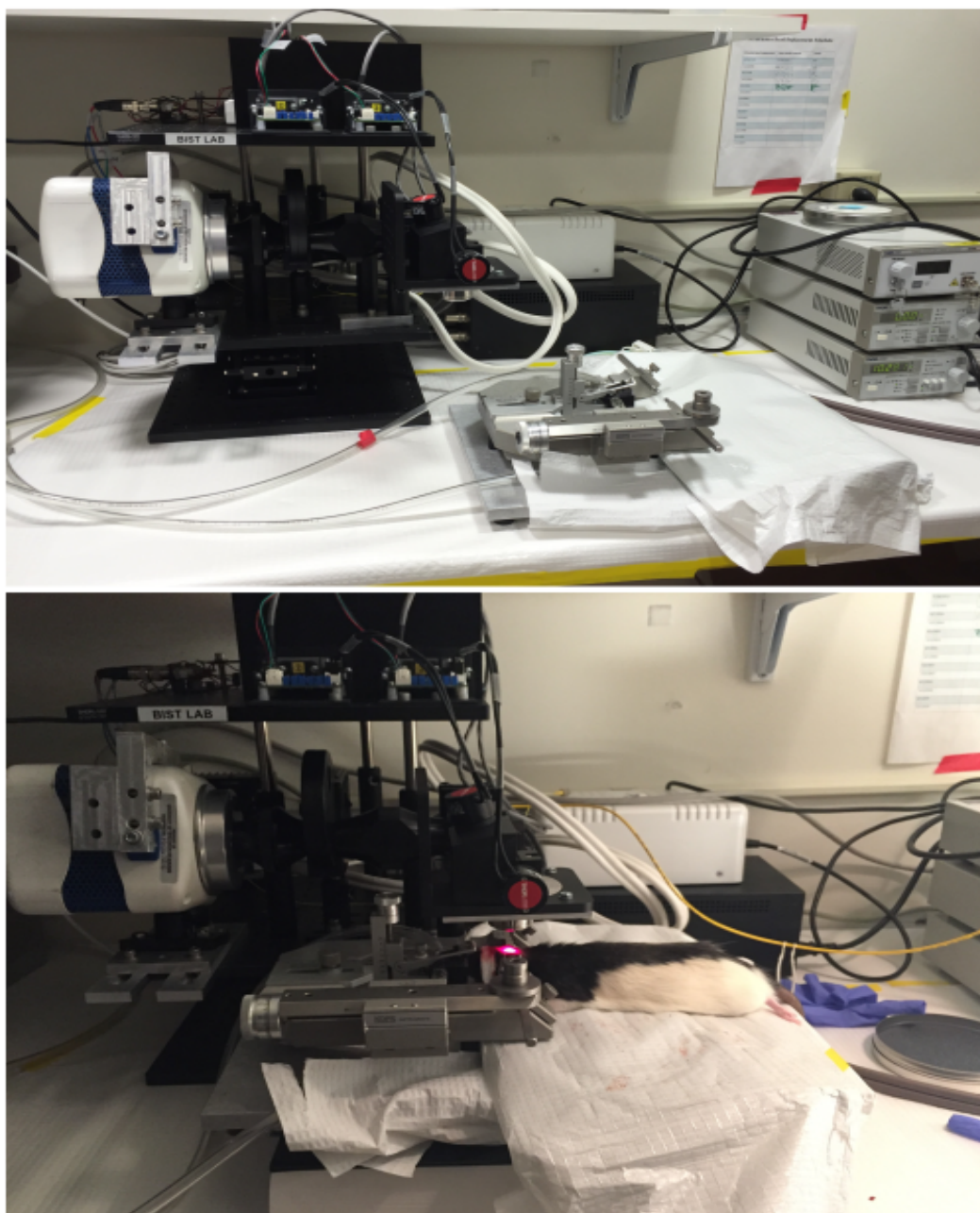


**Figure 4.12:** Experimental setup in surgery room for in vivo scanning of rat brain.

### 4.3.1 Animal Preparation

All procedures were carried out in a facility accredited by the Association for Assessment and Accreditation and Laboratory Animal Care and approved by the University of Wisconsin-Milwaukee Institutional Animal Care and Use Committee (IACUC) and conducted within the ethical guidelines of the National Institutes of Health (NIH).

**Subjects:** We used 12 naïve male Long-Evans rats (300-400g; Harlan, WI) housed individually in shoebox cages with free access to food and water in a room maintained on a 14:10 light/dark cycle. All experiments took place during the light portion of the cycle. Spring-Fill Crinkle Cut Kraft (Quality Packaging, WI) paper bedding was provided as environmental enrichment.

**Surgical procedures/Virus injection:** Animals were anesthetized with isoflurane in 100% oxygen (induction occurred with 4% isoflurane and maintained with 2%). Rats were mounted in a stereotaxic apparatus (Kopf Instruments). Purified AAV9-CAG-GFP was infused into the primary somatosensory cortex (forelimb) (A/P -1.0mm, M/L + 3.8 mm) and the primary visual cortex (A/P -5.3mm, M/L -3.8mm). The depth of injection was systematically varied to include 0.8mm, 1.0mm, 1.5mm, and 2.0mm. The injection volume was also systematically varied to include 0.2 $\mu$ l, 0.5 $\mu$ l, and 0.75 $\mu$ l. The virus was infused using a 10 $\mu$ l syringe with a 34-gauge needle mounted to a stereotaxic automated injector at a rate of 0.05 $\mu$ l/min. The injector was left in place for 10 minutes, following the injection, to allow diffusion of the virus away from the injector. One to four weeks later, animals are ready to perform the experiments.

**Tissue Extraction/Sectioning:** Immediately following the completion of experiments, animals were deeply anesthetized with isoflurane, transcardially perfused with 0.2MPBS followed by 10% buffered formalin. Brains were removed and post-fixed in 10% formalin for 24-hours before being transferred to 30% sucrose/PB. The brains were then frozen, sectioned into coronal slices of 200 $\mu$ m thickness, then mounted on glass slides, and coverslipped

with UltraCruz mounting medium (Santa Cruz, CA) containing  $1.5\mu\text{g/ml}$  DAPI (for nuclear counter staining).

Figure 4.13 shows an example of the injection sites with identical volumes and depths, and a rat's skull before drilling the holes for the injections.

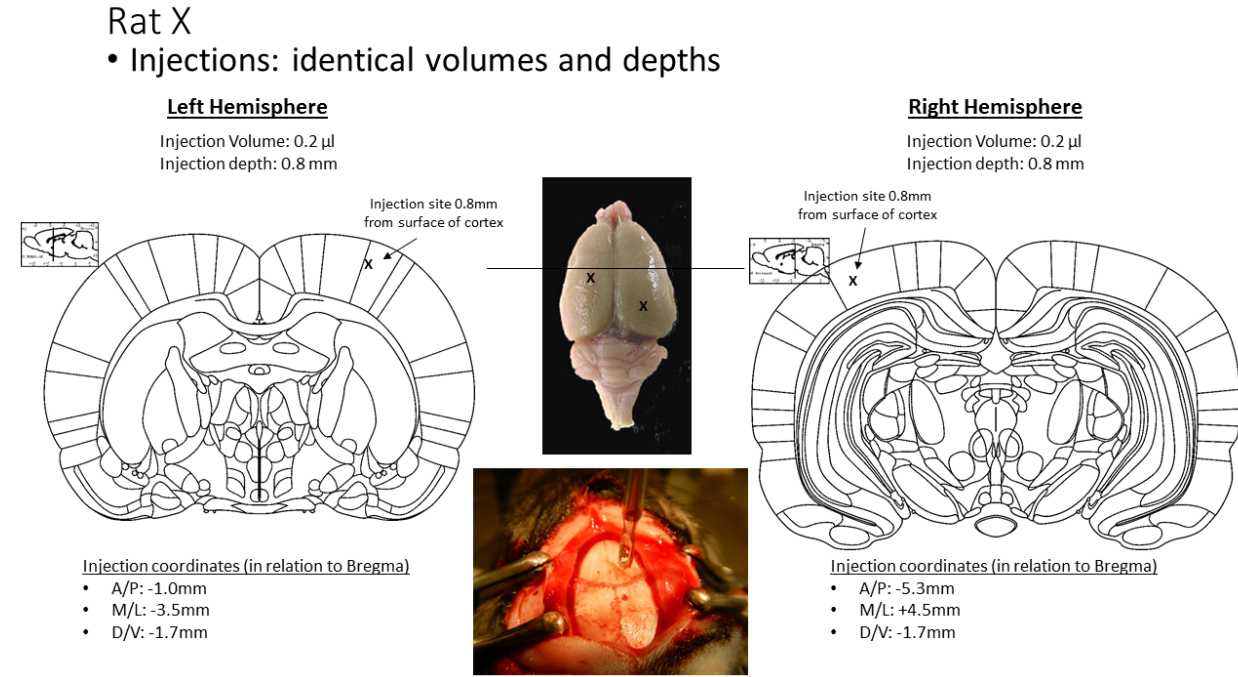


**Figure 4.13:** Injection sites and rat's skull before the injection.

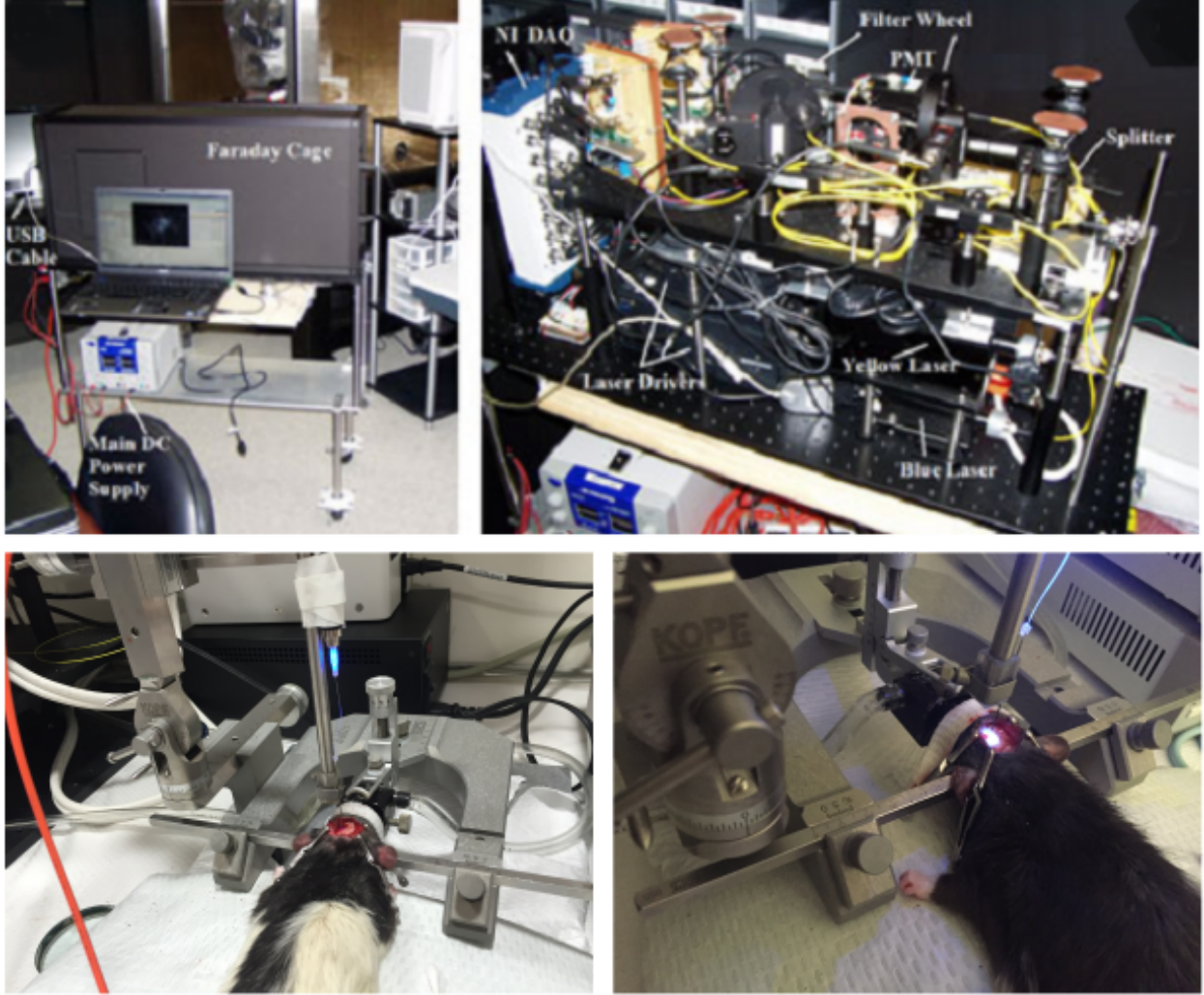
### 4.3.2 In-vivo Experimental Results

Similar to the phantom studies, to confirm our results, we tried two methods. First, we used our fiber-optic-based probe system [89] for the precise delivery of excitation light pulses and detection of fluorescence signals, all done in-vivo. Next, we used a confocal microscope to image the fluorescence distribution in brain slices tissue after sacrificing the animal.

The probe system [89] is shown in Figure 4.14. The system works by inserting a thin optical fiber into the brain of the animal to deliver light pulses to the region of interest and recording the intensity of the corresponding emission signals. The excitation light and the associated emission signals are frequency modulated by chirp pulses, which is a sinusoidal

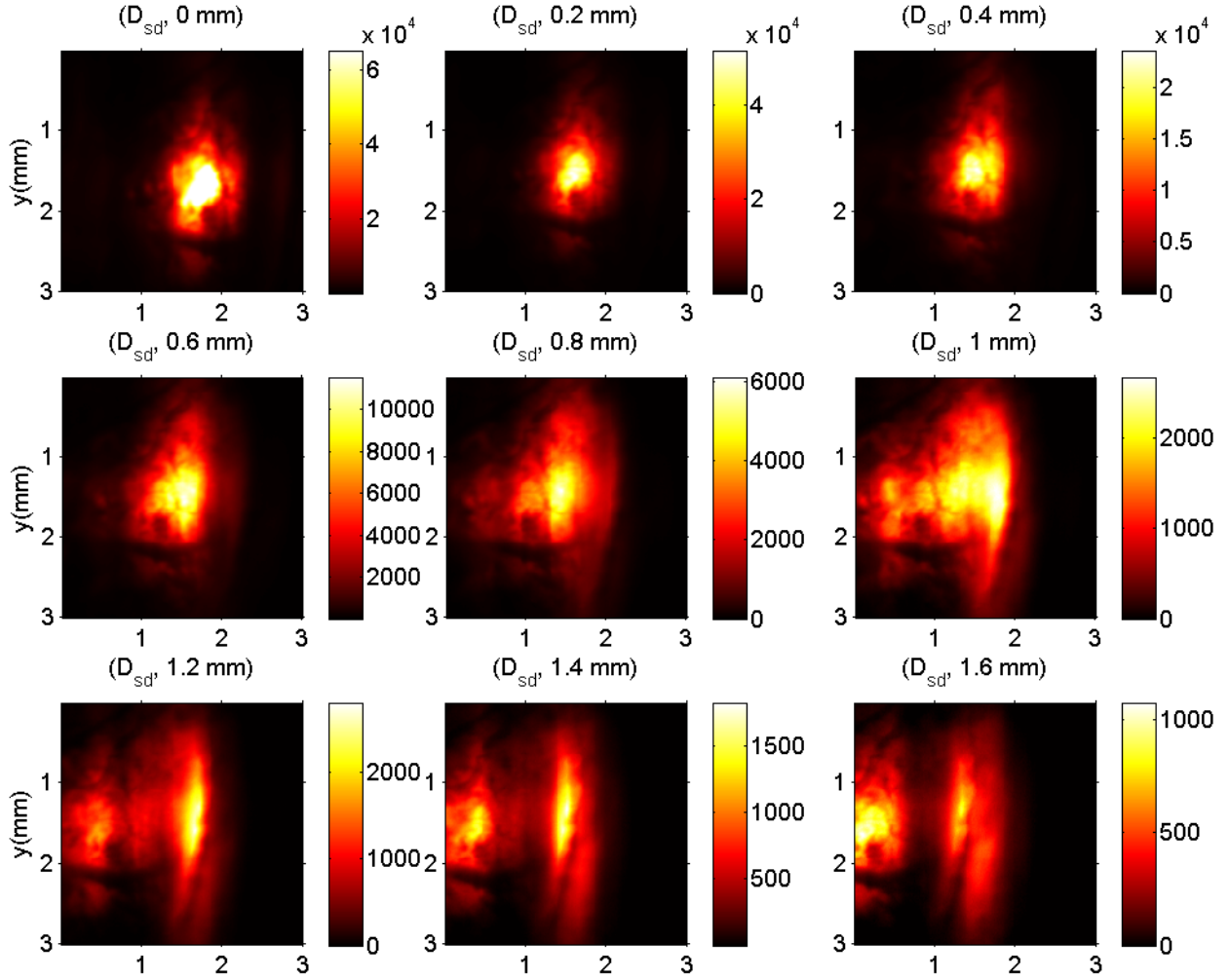


function with constant amplitude, but linearly swept frequency. This way, the system provides a mechanism to read fluorescence signals at the tip of the fiber with the optimized signal to noise ratio (SNR).



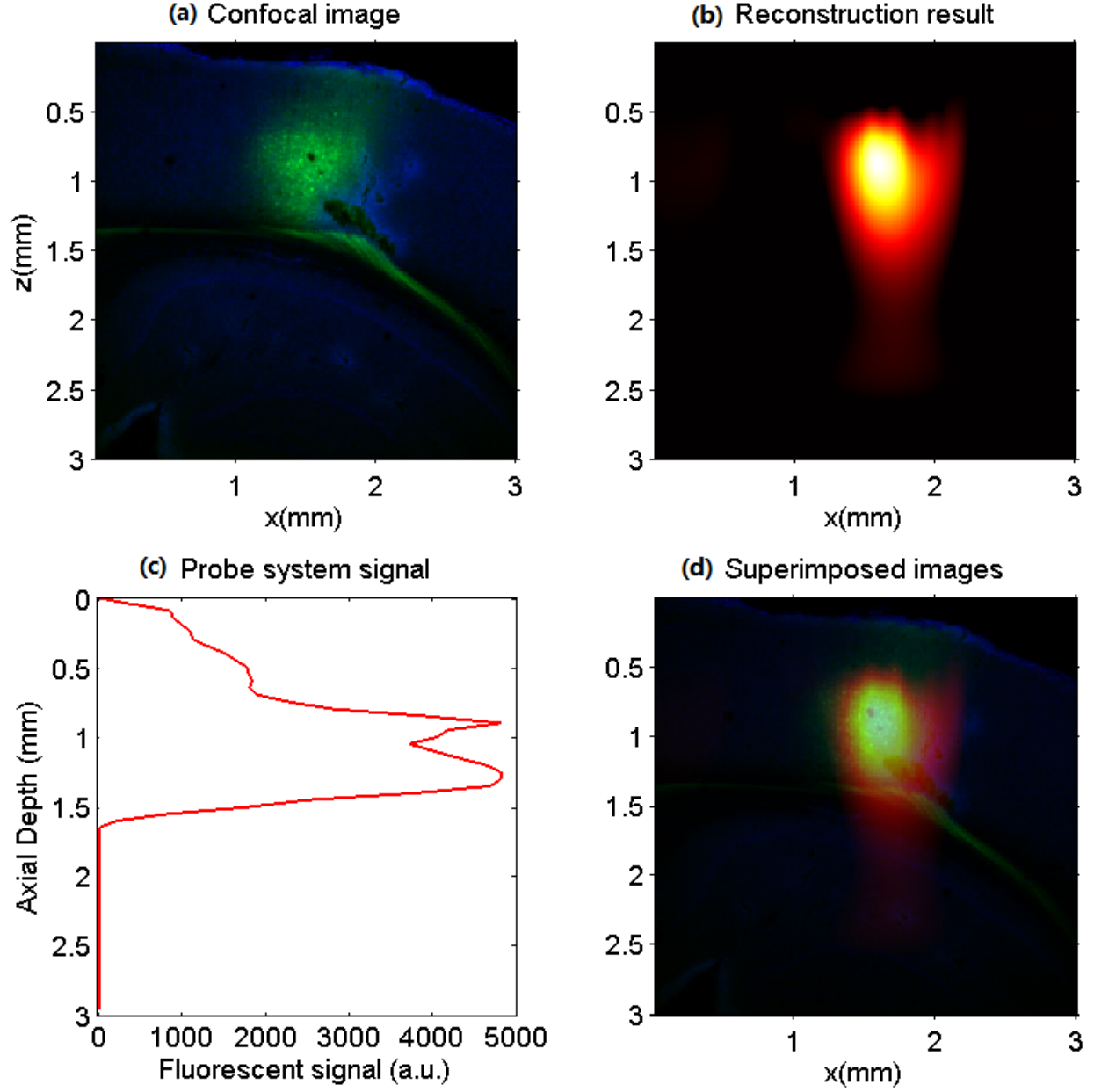
**Figure 4.14:** Single-fiber probe system [89]. A rat before and during the experiments with the probe system.

Figure 4.15 shows the experimental raw data collected from the right hemisphere of a rat brain which received injection at the depth of 0.8mm. Again, the raw data can be examined by eye to infer information about the shape and depth of structures within the tissue and therefore can give us a great deal of information regarding the distribution of fluorescence within the tissue.



**Figure 4.15:** Experimental raw data of a rat brain which was injected with GFP in right hemisphere, at the depth of 0.8mm (color bar shows the fluorescence intensity).

Figures 4.16 and 4.17 display some experimental results collected from the brain of the same rat who has received injections at depths of 0.8mm and injection volumes of  $0.2\mu\text{l}$ , in both right and left hemispheres. Figures show the superimposed images of reconstruction results and the fluorescence image of a slice close to the site of the experiment. The probe system signal is also shown as a curve displaying the fluorescence intensity as a function of the penetration depth. As it can be seen, there is a good match between the FLOT result and what we get from the confocal microscopy and the single-fiber probe system.



**Figure 4.16:** Experimental data of an in-vivo scan of a rat brain with the injection depth of 0.8mm and injection volume of  $0.2\mu l$  in the right hemisphere, (a) a confocal microscopy image of a slice close to the site of experiment, (b) FLOT reconstruction result, (c) probe system's curve showing the fluorescence intensity as a function of the penetration depth, (d) superimposed image of the reconstruction result and the confocal microscopy image.



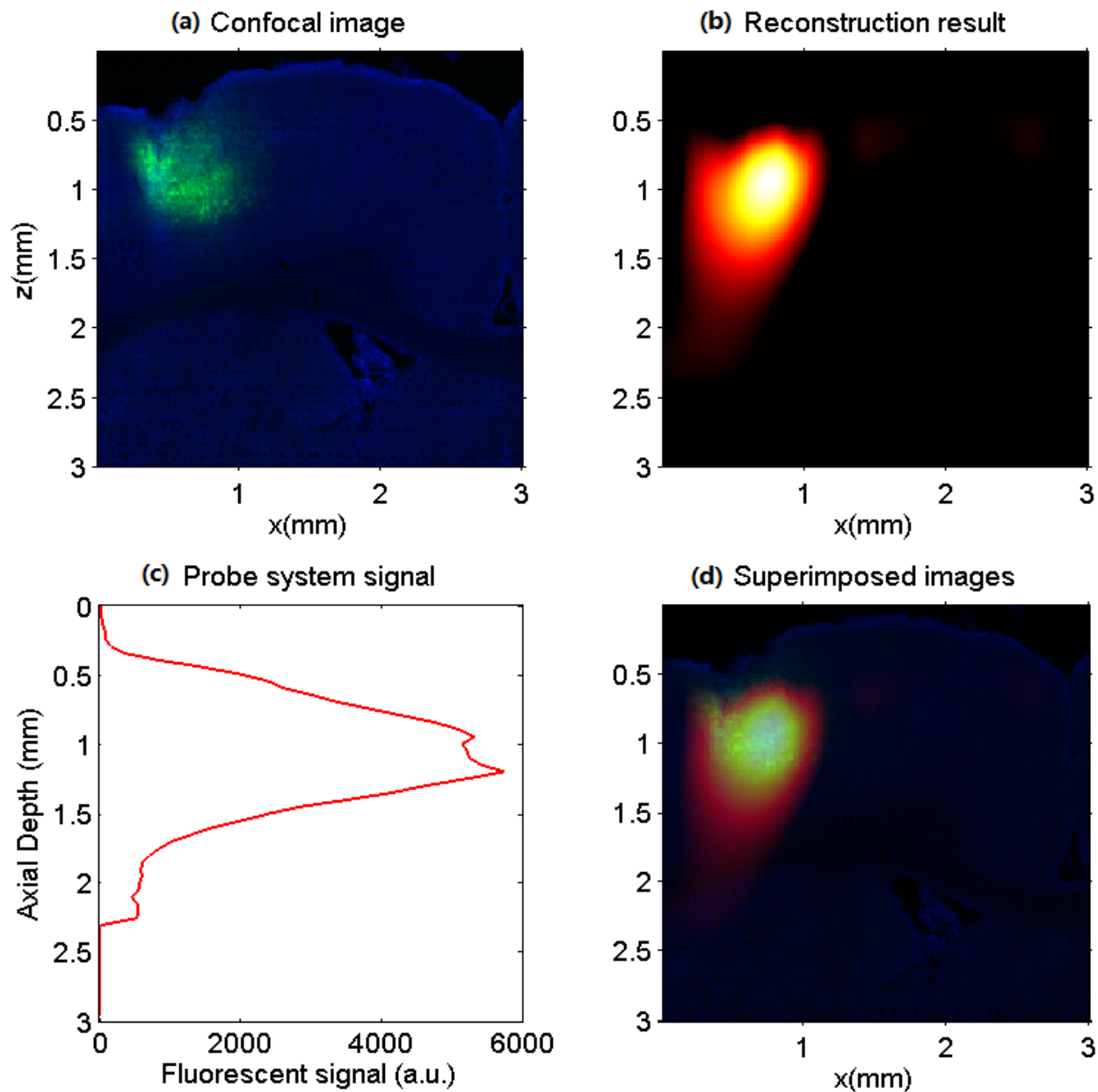


**Figure 4.17:** Experimental data of an in-vivo scan of a rat brain with the injection depth of 0.8mm and injection volume of  $0.2\mu l$  in the left hemisphere, (a) a confocal microscopy image of a slice close to the site of experiment, (b) FLOT reconstruction result, (c) probe system's curve showing the fluorescence intensity as a function of the penetration depth, (d) superimposed image of the reconstruction result and the confocal microscopy image.

FLOT is also able to confirm if the gene expression is not successful for any reason. Figure 4.18 shows a case that we did not get any fluorescence data scanning with the FLOT system. The probe system curve and confocal microscopy image of the rat brain also confirm

that the gene delivery or expression was not successful.

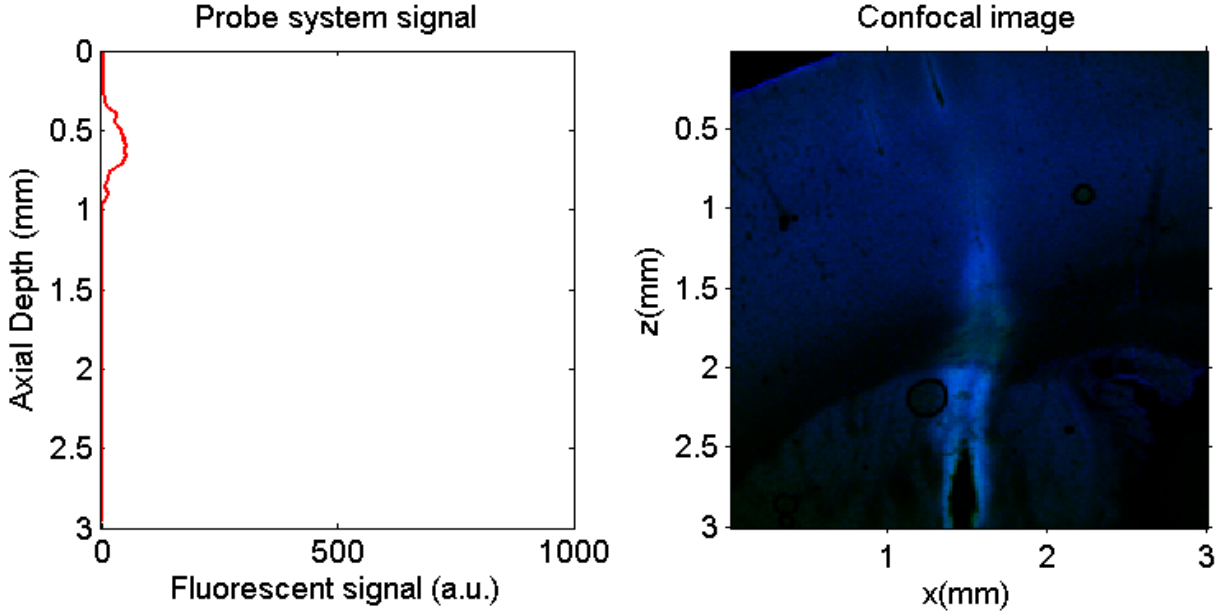


**Figure 4.18:** Experimental data of an in-vivo scan of a rat brain for which the gene expression was not successful, (a) the probe system signal, (b) confocal image of the corresponding brain slice.

## 4.4 Summary

In this chapter, the performance of the developed fluorescent laminar optical tomography (FLOT) system was discussed through three test models, and the reconstruction results were presented. One of the challenges in fluorescent tomography, is finding the accurate depth of the fluorescent object. In phantom experiments, the actual depth of the micro-channel buried inside a highly scattering medium was determined using a SD-OCT system and the reconstruction results using the FLOT system were in a good match with the OCT measurements. The in-vivo animal experiments were also conducted on rat's thinned-skull. Two different mechanisms were employed to compare the FLOT results with the actual expression of GFP. First one was by using a single optical fiber probe system [89] to define the axial distribution of the GFP. Then, the animal was sacrificed and the brain tissue was extracted, sliced and imaged by a confocal fluorescence microscope. Live animal experi-

ments also showed promising results in using the FLOT system for noninvasive imaging of fluorescent proteins and the system is particularly useful for optogenetic applications.

---

## Chapter 5

### Conclusion and Future Directions

Fluorescence imaging is a powerful tool for non-invasively investigating biomedical systems. The tomography technique presented here, the Fluorescence Laminar Optical Tomography (FLOT), enables us to derive quantitative information clarifying the fluorescence distribution in three-dimensional structures, with applications in different biomedical research areas. In particular, FLOT targets the reconstruction of fluorescence distributions in the rat brain for optogenetic applications. The method is non-invasive, fast, sensitive, and relatively in-expensive; allowing for reasonable throughput to indirectly study neural activities by confirming the success of gene delivery or protein expression, in-vivo.

The development of FLOT scanner is a step towards filling the gap between microscopic and macroscopic techniques, offering larger penetration depth than microscopic techniques and higher resolution than macroscopic techniques. The forward model of the image reconstruction algorithm is based on Monte Carlo simulation for light propagation in inhomogeneous tissue and the inverse problem is solved using an iterative reconstruction method. The geometry of the sources and detectors were defined for the banana-shaped sensitivity curves, to efficiently scan the tissue at desired depths. The setup was tested in three test models: computer simulations, silicon-based microchannel phantoms, and in-vivo imaging of rat brains. Experiments showed a good match between the actual and reconstructed fluorophore distributions in all three models.

For future work, the main improvement in the technique can be achieved by developing a better forward model and image reconstruction schemes. It is possible to reduce the computational time by using more refined inversion strategies. The quality of reconstructed images can also be improved by incorporating prior information, which can be obtained by

considering the physics and the physiology of the problem. Such information potentially helps to reduce the effect of the ill-posedness by using the measurements obtained in a more effective way, and therefore improving the accuracy of the model.

Limitations associated with the operation in the visible spectrum, particularly the wavelength below 500nm, such as the limited depth of penetration of blue light (450nm), or the autofluorescence caused by the excitation wavelength, can be strongly improved by using red/near-infrared shifted fluorescence proteins, such as tdTomato and mCherry, instead of GFP. However, it is worth mentioning that based on the application and specifications of the experimental setup, some critical factors such as brightness or photostability needs to be considered before choosing any specific fluorescent protein. For instance, GFP has a higher brightness factor compared to mCherry, which was one of the reasons we chose GFP for our experiments.

A potential application of our system is on-line 3D monitoring of neural activity during optogenetic/electrode-based stimulation. Fluorescent proteins are used to study the dynamic changes within the cells, e.g., ion concentration via calcium imaging. Nevertheless, such fluorescent indicators usually have fast kinetics; therefore, recording the fluorescence emission of these molecules requires a tomography system that offers a fast scanning and recording mechanism. If the image acquisition time is short enough, compared to the physiological fluctuations, image time series can be obtained to draw a clear picture of the dynamics under test and the underlying cellular activity. We believe with some modifications in our system, we will be able to fulfill the speed requirements and our system can be used for this new application.

---

## BIBLIOGRAPHY

- [1] Elizabeth M. C. Hillman, “Optical brain imaging in vivo: techniques and applications from animal to man,” *Journal of Biomedical Optics* 12(5), 051402, 2007.
- [2] Elizabeth M. C Hillman, Anna Devor, Andrew K. Dunn, David A. Boas, “Laminar optical tomography: high-resolution 3D functional imaging of superficial tissues,” *SPIE*, Vol. 6143, 2006.
- [3] Elizabeth M. C. Hillman, Cyrus B. Amoozegar, Tracy Wang, Addason F. H. McCaslin, Matthew B. Bouchard, James Mansfield, and Richard M. Levenson, “In vivo optical imaging and dynamic contrast methods for biomedical research,” *Philosophical transactions. Series A Math Phys Eng Sci.*, 4620-4643, 2011.
- [4] Youngwoon Choi, Changhyeong Yoon, Moonseok Kim, Wonjun Choi, and Wonshik Choi, “Optical imaging with the use of a scattering lens,” *IEEE Journal of Selected Topics in Quantum Electronics*, Vol. 20, NO. 2, 2014.
- [5] Rajadhyaksha, M., Anderson, R. R. and Webb, R. H., “Video-rate confocal scanning laser microscope for imaging human tissues in vivo,” *Applied Optics*, Vol. 38, Issue 10, pp. 2105-2115, 1999.
- [6] Denk, W., Strickler, J. H. and Webb, W. W., “Two-photon laser scanning fluorescence microscopy,” *Science*, Vol. 248 No. 4951 pp. 73-76, 1990.
- [7] Elizabeth M. C. Hillman, David A. Boas, Anders M. Dale, and Andrew K. Dunn, “Laminar optical tomography: demonstration of millimeter-scale depth-resolved imaging in turbid media,” *Optics Letters*, Vol. 29, No. 14, 2004.

- [8] Baohong Yuan, Sean A. Burgess, Amir Iranmahboob, Matthew B. Bouchard, Nicole Lehrer, Clmence Bordier, and Elizabeth M. C. Hillman, "A system for high-resolution depth-resolved optical imaging of fluorescence and absorption contrast," *Review of Scientific Instruments*, 80(4):043706, 2009.
- [9] Ramin Pashaie, Polina Anikeeva, Jin Hyung Lee, Rohit Prakash, Ofer Yizhar, Matthias Prigge, Divya Chander, Thomas J. Richner, and Justin Williams, "Optogenetic brain interfaces," *IEEE Reviews in Biomedical Engineering*, Vol. 7, 2014.
- [10] "Medical image processing market - global industry analysis, size, share, growth, trends and forecast, 2014-2020," Online Available at: <http://www.transparencymarketresearch.com/medical-image-processing.html>, Accessed September 2015.
- [11] Andrew Webb, "Introduction to biomedical imaging," *Wiley-IEEE Press*, 2003.
- [12] "Medical imaging modalities," Online Available at: <http://www.medicalimaging.org/about-mita/medical-imaging-primer>, Accessed September 2015.
- [13] "Medical imaging," Online Available at: <http://www.cocir.org/?id=171>, Accessed September 2015.
- [14] "General nuclear medicine," Online Available at: <http://www.radiologyinfo.org/en/info.cfm?pg=gennuclear>, Accessed September 2015.
- [15] National Institute of Biomedical Imaging and Bioengineering, "Optical imaging," Online Available at: <http://www.nibib.nih.gov/science-education/science-topics/optical-imaging>, Accessed September 2015.
- [16] Tarik F. Massoud and Sanjiv S. Gambhir, "Molecular imaging in living subjects: seeing

- fundamental biological processes in a new light,” *Genes and Development*, 17:545580, 2003.
- [17] Ronan M. Valentine, Sally H. Ibbotson, Kenny Wood, C. Tom A. Brown and Harry Moseley, “Modellingfluorescence in clinical photodynamic Therapy,” *Photochemical and Photobiological Sciences*, 12(1):203-13, 2013.
- [18] Valery Tuchin, “Tissue optics: light scattering methods and instruments for medical diagnosis,” *SPIE Press Monograph*, 2007.
- [19] Steven L Jacques, “Optical properties of biological tissues: a review,” *Physics in Medicine and Biology*, R37R61, 2013.
- [20] Wikipedia, Online Available at: <https://www.wikipedia.org>, Accessed October 2015.
- [21] Lihong V. Wang, Hsin-i W, “Biomedical optics,” *Wiley-Interscience*, 2007.
- [22] Christiana Honsberg and Stuart Bowden, A collection of resources for the photovoltaic educator, Online Available at: <http://www.pveducation.org>, Accessed October 2015.
- [23] Alan D. McNaught, Andrew Wilkinson, “Compendium of chemical terminology: IUPAC recommendations, *Blackwell Science*, 2nd ed. (the ”Gold Book”), 1997.
- [24] Lucian Fodor, Monica Elman, Yehuda Ullmann, “Aesthetic applications of intense pulsed light,” *Springer-Verlag London*, 2011.
- [25] Sean A. Burgess, “Development and applications of laminar optical tomography for in vivo imaging,” *Doctor of Philosophy Thesis, Columbia University*, 2011.
- [26] Brian Herman, Joseph R. Lakowicz, Douglas B. Murphy, Thomas J. Fellers and Michael W. Davidson, “Fluorescence excitation and emission fundamentals,” Online Available at: <http://www.olympusconfocal.com/theory/fluoroexciteemit.html>, Accessed September 2015.



- [27] Reyhaneh Sepehr, “Optical studies of oxidative stress in lung tissue: rodent models,” *Doctor of Philosophy Thesis, University of Wisconsin Milwaukee*, 2014.
- [28] Christoph Bocklin, “Modeling light propagation in tissue,” *Doctor of Philosophy Thesis, ETH Zurich University*, 2014.
- [29] Marcelo Soto Thompson, “Photodynamic therapy utilizing interstitial light delivery combined with spectroscopic methods,” *Doctor of Philosophy Thesis, Lund Institute of Technology*, 2004.
- [30] S. A. Prahl, S. L. Jacques, Monte Carlo simulations, Online Available at: <http://omlc.org/software/mc/>, Accessed October 2015.
- [31] Robert Splinter, Brett A. Hooper, “An Introduction to biomedical optics,” *CRC Press*, 2006.
- [32] S. A. Prahl, M. Keijzer, S. L. Jacques, A. J. Welch, “A Monte Carlo model of light propagation in tissue,” *SPIE Institute Series*, Vol. IS 5, 1989.
- [33] Caigang Zhu and Quan Liu, “Review of Monte Carlo modeling of light transport in tissues,” *Journal of Biomedical Optics*, 18(5), 050902, 2013.
- [34] Yu Chen, Shuai Yuan, Jeremiah Wierwille, Renee Naphas, Qian Li, Tiffany R. Blackwell, Paul T. Winnard, Jr., Venu Raman and Kristine Glunde, “Integrated optical coherence tomography (OCT) and fluorescence laminar optical tomography (FLOT),” *IEEE Journal of Selected Topics in Quantum Electronics*, Vol. 16, No. 4, 2010.
- [35] Elizabeth M. C. Hillman and Sean A. Burgess, “Sub-millimeter resolution 3D optical imaging of living tissue using laminar optical tomography,” *Laser Photon Rev.*, 1; 3(1-2): 159179, 2009.
- [36] Yu Chen, Chia-Pin Liang, Yang Liu, Andrew H. Fischer, Anil V. Parwani and Liron

- Pantanowitz “Review of advanced imaging techniques,” *Journal of Pathology Informatics*, 3:22, 2012.
- [37] A. F. Gmitro and D. Aziz, “Confocal microscopy through a fiber-optic imaging bundle,” *Optic Letters*, Vol. 18, pp. 565567, 1993.
- [38] T. D. Wang, M. J. Mandella, C. H. Contag, and G. S. Kino, “Dual-axis confocal microscope for high-resolution in vivo imaging,” *Optic Letters*, Vol. 28, pp. 414416, 2003.
- [39] W. Denk, J. H. Strickler, and W. W. Webb, “Two-photon laser scanning fluorescence microscopy,” *Science*, Vol. 248, pp. 7376, 1990.
- [40] M. T. Myaing, D. J. MacDonald, and X. Li, “Fiber-optic scanning twophoton fluorescence endoscope,” *Optic Letters*, V. 31, pp. 10761078, 2006.
- [41] D. Huang, E. A. Swanson, C. P. Lin, JS. Schuman, W. G. Stinson, W. Chang, M. R. Hee, T. Flotte, K. Gregory, C. A. Puliafito, and G. H. Fujimoto “Optical coherence tomography,” *Science*, Vol. 254, No. 5035, pp. 1178-1181, 1991.
- [42] J. G. Fujimoto, “Optical coherence tomography for ultrahigh resolution in vivo imaging,” *Nature Biotechnology*, Vol. 21, No. 11, 2003.
- [43] Seth Thomas Frye, “Monitoring Changes in hemodynamics following optogenetic stimulation,” *Master of Science Thesis, University of Wisconsin Milwaukee*, 2014.
- [44] Alana Mauluidy Soehartono, “Angiography and monitoring of hemodynamic signals in the brain via optical coherence tomography,” *Master of Science Thesis, University of Wisconsin Milwaukee*, 2013.
- [45] Huabei Jiang, “Diffuse optical tomography: principles and applications,” *CRC Press*, 2010.
- [46] Atam P. Dhawan, H. K. Huang, and Dae-Shik Kim, “Principles and advanced methods in medical imaging and image analysis,” *World Scientific Publishing Co.*, 2008.

- [47] BD Biosciences, Online Available at: <http://www.bdbiosciences.com>, Accessed April 2016.
- [48] Mikhail Y. Berezin and Samuel Achilefu, "Fluorescence lifetime measurements and biological imaging," *Chemical Reviews*, 110 (5), pp. 2641-2684, 2010.
- [49] Luker GD, Luker KE. "Optical imaging: current applications and future directions," *Journal of Nuclear Medicine*, 49:14, 2008.
- [50] Vasilis Ntziachristos, "Fluorescence Molecular Imaging," *Annual Review of Biomedical Engineering*, 8:1-33, 2006.
- [51] Marta Fernandez-Surez and Alice Y. Ting, "Fluorescent probes for super-resolution imaging in living cells," *Nature Reviews, Molecular Cell Biology*, Vol. 9, 929-94, 2008.
- [52] Elizabeth M.C. Hillman, Anna Devor, Matthew B. Bouchard, Andrew K. Dunn, G.W. Krauss, Jesse Skoch, Brian J. Bacsikai, Anders M. Dale, and David A. Boas, "Depth-resolved optical imaging and microscopy of vascular compartment dynamics during somatosensory stimulation," *NeuroImage*, Vol. 35, 891-904, 2007.
- [53] Sean A. Burgess, Matthew B. Bouchard, Baohong Yuan, and Elizabeth M. C. Hillman, "Simultaneous multiwavelength laminar optical tomography," *Optic Letters*, Vol. 33, No. 22, 2008.
- [54] Shuai Yuan, Qian Li, James Jiang, Alex Cable, and Yu Chen, "Three-dimensional coregistered optical coherence tomography and line-scanning fluorescence laminar optical tomography," *Optics Letters*, Vol. 34, No. 11, 2009.
- [55] Sean A. Burgess, Dsire Ratner, Brenda R. Chen, and Elizabeth M. C. Hillman, "Fiber-optic and articulating arm implementations of laminar optical tomography for clinical applications," *Biomedical Optics Express*, Vol. 1, No. 3, 2010.

- [56] Timothy J. Muldoon, Sean A. Burgess, Brenda R. Chen, Dsire Ratner, and Elizabeth M. C. Hillman, “Analysis of skin lesions using laminar optical tomography,” *Biomedical Optics Express*, Vol. 3, No. 7, 2012.
- [57] Smith MH, Denninghoff KR, Lompado A, Hillman LW, “Effect of multiple light paths on retinal vessel oximetry,” *Applied Optics*, 39(7):1183-1193, 2000.
- [58] Feixiao Long, Mehmet S. Ozturk, Xavier Intes, and Shiva Kotha, “Dental imaging using laminar optical tomography and micro CT,” *SPIE*, Vol. 8937, 2014.
- [59] Feng Zhang, Alexander M. Aravanis, Antoine Adamantidis, Luis de Lecea and Karl Deisseroth, “Circuit-breakers: optical technologies for probing neural signals and systems,” *Nature Reviews*, Vol. 8, 2007.
- [60] Karl Deisseroth, “Optogenetics,” *Nature Methods*, Vol. 8, 2629, 2011.
- [61] Karl Deisseroth, “Controlling the brain with light,” *Scientific American*, 2010.
- [62] Ofer Yizhar, Lief E. Fenno, Thomas J. Davidson, Murtaza Mogri, and Karl Deisseroth, “Optogenetics in neural systems,” *Neuron Primer*, Vol. 71, Issue 1, p934, 2011.
- [63] Viviana Gradinaru, Kimberly R. Thompson, Feng Zhang, Murtaza Mogri, Kenneth Kay, M. Bret Schneider, and Karl Deisseroth, “Targeting and readout strategies for fast optical neural control in vitro and in vivo,” *The Journal of Neuroscience*, 27(52): 14231-14238, 2007.
- [64] Thomas Knpfel, Michael Z. Lin, Anselm Levskaya, Lin Tian, John Y. Lin, and Edward S. Boyden, “Toward the second generation of optogenetic tools,” *The Journal of Neuroscience*, 30(45): 14998-15004, 2010.
- [65] James Butler, “Optogenetics: shining a light on the brain,” *Bioscience Horizons*, pp. 1-8, 2012.

- [66] James Butler, “Diffuse optics for tissue monitoring and tomography,” *Reports on Progress in Physics*, 73(7):076701, 2010.
- [67] Collimating emission-port adapter XT2, Evolve 512 EMCCD Camera, Online Available at: <http://www.photometrics.com/>, Accessed November 2015.
- [68] Thorlabs, “Collimator, Cylindrical Lens, Acromatic Lens, GVS212 - 2D Large Beam Diameter Galvo System,” Online Available at: <https://www.thorlabs.com>, Accessed November 2015.
- [69] National Institute of Biomedical Imaging and Bioengineering, “NI USB-6212,” Online Available at: <http://sine.ni.com/nips/cds/view/p/lang/en/nid/207096>, Accessed November 2015.
- [70] Zhenwen Xue, Jie Tian, Dong Han, and Xibo Ma, “A novel method for eliminating autofluorescence of small animals in fluorescence molecular imaging,” *SPIE, Medical Imaging 2011: Biomedical Applications in Molecular, Structural, and Functional Imaging*, 79651D, 2011.
- [71] Farid Atry and Ramin Pashaie, “Analysis of intermediary scan-lens and tube-lens mechanisms for optical coherence tomography,” *Applied Optics*, Vol. 55, No. 4, 2016.
- [72] David A. Boas, Constantinos Pitris, and Nimmi Ramanujam, “Handbook of biomedical optics,” *CRC Press*, 2011.
- [73] A. P. Gibson, J. C. Hebden, and S. R. Arridge, “Recent advances in diffuse optical imaging,” *Physics in Medicine and Biology*, 50, R1R43, 2005.
- [74] Gene H. Golub and Charles F. Van Loan, “Matrix computations,” *The Johns Hopkins University Press*, 2nd edition, 1989.
- [75] Daniela Calvetti and Lothar Reichel, “Tikhonov regularization of large linear problems,” *BIT Numerical Mathematics*, Vol. 43, Issue 2, pp 263-283, 2003.

- [76] R. Gordon, “A tutorial on ART (algebraic reconstruction techniques),” *IEEE Press*, Vol. 21, Issue 3, 1974.
- [77] C. Kakand and M. Slaney, “Principles of Computerized Tomographic Imaging,” *SIAM*, 1988.
- [78] A. H. Andersen and A. C. Kak, “Simultaneous algebraic reconstruction technique (SART): a superior implementation of the art algorithm,” *Ultrason Imaging*, 6(1):81-94, 1984.
- [79] Jixing Yao, Fenghua Tian, Yothin Rakvongthai, Soontorn Orintara, and Hanli Liu, “Quantification and normalization of noise variance with sparsity regularization to enhance diffuse optical tomography,” *Biomedical Optics Express*, Vol. 6, No. 8, 2015.
- [80] P. C. Hansen and M. Saxild-Hansen, “AIR Tools A MATLAB Package of Algebraic Iterative Reconstruction Techniques,” *Journal of Computational and Applied Mathematics*, Vol. 236, No. 8, 2012.
- [81] Richard J. Gaudette, Dana H. Brooks, Charles A. DiMarzio, Misha E. Kilmer, Eric L. Miller, Thomas Gaudette, and David A. Boas, “A comparison study of linear reconstruction techniques for diffuse optical tomographic imaging of absorption coefficient,” *Physics in medicine and biology*, Vol. 45, No. 4, 2000.
- [82] Murat Guven, Birsan Yazici, and Vasilis Ntziachristos, “Fluorescence optical tomography with a priori information,” *Proceedings of SPIE*, 2007.
- [83] Rolf B. Saager, Clement Kondru, Kendrew Au, Kelly Sry, Frederick Ayers, and Anthony J. Durkin, “Multilayer silicone phantoms for the evaluation of quantitative optical techniques in skin imaging,” *Proceedings of SPIE*, Vol. 7567, 2010.
- [84] Theodore Moffitt, Yin-Chu Chen, and Scott A. Prahl, “Preparation and characterization of polyurethane optical phantoms,” *Journal of Biomedical Optics*, 11(4):041103, 2006.

- [85] Yuming Liu, Steven L. Jacques, Mehdi Azimipour, Jeremy D. Rogers, Ramin Pashaie, and Kevin W. Eliceiri, “OptogenSIM: a 3D Monte Carlo simulation platform for light delivery design in optogenetics,” *Biomedical Optics Express*, Vol. 6, No. 12, 2015.
- [86] Ashwin B. Parthasarathy, W. James Tom, Ashwini Gopal, Xiaojing Zhang, and Andrew K. Dunn, “Robust flow measurement with multi-exposure speckle imaging,” *Optical Society of America*, Vol. 16, No. 3, 2008.
- [87] Center of Micronanotechnology CMI, “General Overview of Polydimethylsiloxane (PDMS) micro-molding,” Online Available at: <https://cmi.epfl.ch/packaging/PDMS.html>, Accessed January 2016.
- [88] Mehdi Azimipour, Ryan Baumgartner, Yuming Liu, Steven L. Jacques, Kevin Eliceiri, and Ramin Pashaie, “Extraction of optical properties and prediction of light distribution in rat brain tissue,” *Journal of Biomedical Optics*, Vol. 19, No. 7, 2014.
- [89] Ramin Pashaie and Ryan Falk, “Single optical fiber probe for fluorescence detection and optogenetic stimulation,” *IEEE Transactions on Biomedical Engineering*, Vol. 60, No. 2, 2013.
- [90] Mehdi Azimipour, Farid Atry, and Ramin Pashaie, “Effect of blood vessels on light distribution in optogenetic stimulation of cortex,” *Optic Letter*, Vol. 40, No. 10, 2173-2176, 2015.